

Winter 2016

Improving nano-drug delivery by using near-real time sensing and feedback

Pratik Adhikari

Follow this and additional works at: <https://digitalcommons.latech.edu/dissertations>

 Part of the [Biomedical Engineering and Bioengineering Commons](#)

**IMPROVING NANO-DRUG DELIVERY BY USING NEAR-REAL
TIME SENSING AND FEEDBACK**

by

Pratik Adhikari, B.S.

A Dissertation Presented in Partial Fulfillment
of the Requirements of the Degree
Doctor of Philosophy

COLLEGE OF ENGINEERING AND SCIENCE
LOUISIANA TECH UNIVERSITY

March 2016

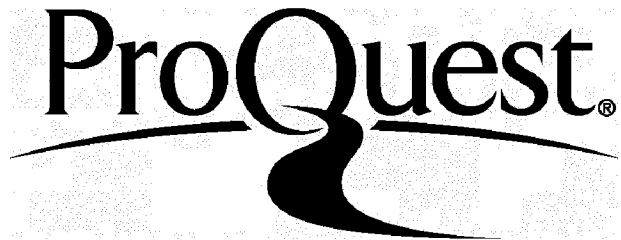
ProQuest Number: 10301321

All rights reserved

INFORMATION TO ALL USERS

The quality of this reproduction is dependent upon the quality of the copy submitted.

In the unlikely event that the author did not send a complete manuscript and there are missing pages, these will be noted. Also, if material had to be removed, a note will indicate the deletion.



ProQuest 10301321

Published by ProQuest LLC(2017). Copyright of the Dissertation is held by the Author.

All rights reserved.

This work is protected against unauthorized copying under Title 17, United States Code.
Microform Edition © ProQuest LLC.

ProQuest LLC
789 East Eisenhower Parkway
P.O. Box 1346
Ann Arbor, MI 48106-1346

LOUISIANA TECH UNIVERSITY

THE GRADUATE SCHOOL

08/14/2015

Date

We hereby recommend that the dissertation prepared under our supervision
by Pratik Adhikari, B.S.

entitled "IMPROVING NANO-DRUG DELIVERY BY USING NEAR-REAL TIME
SENSING AND FEEDBACK"

be accepted in partial fulfillment of the requirements for the Degree of
Doctor of Philosophy

D. Patrick O'Neil
Supervisor of Dissertation Research
Steven Jones
Head of Department
Biomedical Engineering
Department

Recommendation concurred in:

S. Zivanovic
Steven Jones
Mary Ann
Pat A. Owen

Advisory Committee

Approved: [Signature]
Director of Graduate Studies

Approved: Sheryl S. Shalman
Dean of the Graduate School

Misham Hegab / SD
Dean of the College

ABSTRACT

Personalized medicine, seen as the solution to address the variability among the individuals, is the movement which proposes customization of medical procedures based on the need of the patient during the stages of prevention, diagnosis, treatment, and follow up. As the technology in medicine expands and newer methods of diagnosis and treatment are introduced in the clinic, real time data from the procedures is critical to assess the performance at point of care. Real time feedback, through collection of data at point of care would help make informed clinical decisions, potentially improving the efficacy of the treatment. In this dissertation, the development of instrumentation and data analysis protocols for rapid feedback during clinical application of antimalarial quinine, antifungal amphotericin b, and gold nanoparticles are discussed.

Nanoparticles have emerged as powerful treatment modality in many biomedical sensing and therapeutic applications. The application of intravenously delivered near-infrared absorbing gold nanoparticles for photothermal ablation of solid tumors has been previously reported. A lot of research has been devoted to the development and characterization of gold nanoparticles for clinical applications, and with multiple clinical trials underway, ongoing pre-clinical research continues towards better understanding the *in vivo* interactions of these particles. The current need for a set of best practices in nanomedicine to increase the *in vivo* treatment efficacy was the rationale for this investigation.

In an effort to enable informed decisions at point-of-care applications, within a relevant time frame, instrumentation for real-time plasma concentration (multi-wavelength photoplethysmography) and protocols for rapid elemental analysis (energy dispersive X-Ray fluorescence) of tumor tissue samples have been developed in a murine model. This dissertation describes the implementation and characterization of the novel pulse photometer in terms of its sensing application, and outlines the development of a protocol for quantifying the concentration of gold in excised tumors in a clinically relevant time frame (< 24 hours) using energy dispersive X-ray fluorescence protocol developed for this specific purpose. In this dissertation, we evaluate the relationship between circulation pharmacokinetics and tumor accumulation using gold nanorods which passively accumulated in a murine subcutaneous colon cancer model. The plasma concentration of the near-infrared absorbing nanoparticles was monitored in real-time using a novel pulse photometer. The data collected was used to build a bio distribution curve and to calculate circulation half-life as well as the area under the curve (AUC) using an exponential decay model.

New research efforts are described, which focus on adjuvant therapies that are employed to modify circulation parameters, including the AUC, of nanorods and gold nanoshells. Based on the premise that nanoparticles are primarily removed from the blood by the reticuloendothelial system (RES), this dissertation also demonstrates the effects of RES blockade to prolong the circulation of gold nanoparticles tested on a murine model via intravenous administration of λ -carrageenan at a concentration of 50 mg/kg. Transient RES blockade techniques have the potential to enhance the circulation time of agents that are cleared by the RES. Preliminary studies demonstrated a greater

than 300% increase in average AUC using a reticuloendothelial blockade agent against the control groups.


Further expansion of the application of the novel pulse photometer was achieved by modification of the device for *in vivo* sensing of other clinically applicable molecular drugs such as quinine and amphotericin b. This dissertation reports the development of a non-invasive optical system capable of reporting the *in vivo* vascular concentration of these molecular drugs in near real time.

APPROVAL FOR SCHOLARLY DISSEMINATION

The author grants to the Prescott Memorial Library of Louisiana Tech University the right to reproduce, by appropriate methods, upon request, any or all portions of this Dissertation. It is understood that "proper request" consists of the agreement, on the part of the requesting party, that said reproduction is for his personal use and that subsequent reproduction will not occur without written approval of the author of this Dissertation. Further, any portions of the Dissertation used in books, papers, and other works must be appropriately referenced to this Dissertation.

Finally, the author of this Dissertation reserves the right to publish freely, in the literature, at any time, any or all portions of this Dissertation.

Author



Date 01-27-16

DEDICATION

This dissertation is dedicated to my family and friends for their help and support throughout my college life at Louisiana Tech University. I am deeply indebted to my father, Chiranjibi Adhikari, and my mother, Deepa Adhikari, for all the sacrifices they made, and being a source of constant inspiration and a constant reminder of my goals during all the time I spent away from home. I dedicate my work to my little sister, Prapti Adhikari, who always saw the positive in things, Anita Poudel, for the emotional support when the going got tough. I thank all of my dearest friends who weren't just spectators at the sidelines, but coaches to me in their own little ways. I couldn't have done this without all of you.

TABLE OF CONTENTS

ABSTRACT	iii
DEDICATION	vii
LIST OF TABLES	xiii
LIST OF FIGURES	xiv
ACKNOWLEDGEMENTS	xvii
CHAPTER 1 INTRODUCTION	1
1.1 Photoplethysmography and Monitoring of Nanoparticles and Other Drugs.....	1
1.2 Photoplethysmography, Beer-Lambert's Law and Optical Density.....	2
1.3 Application of Nanoparticles in Development for Cancer Therapies.....	5
1.4 EPR Effect and Passive Targeting.....	9
1.5 AuroShell® Gold Nanoparticles.....	10
1.6 Research Need and Presented Research.....	11
CHAPTER 2 LITERATURE REVIEW	18
2.1 Gold Nanoparticles.....	18
2.2 Clearance of Gold Nanoshells and Nanorods.....	19
2.3 Pulse Photometer.....	20
2.4 Pharmacokinetics.....	24
2.4.1 One Compartment Model.....	24
2.4.2 Population Pharmacokinetics.....	26
2.5 Elemental Analysis.....	26

CHAPTER 3 CALIBRATION AND DETERMINATION OF OPERATIONAL RANGE OF THE PULSE PHOTOMETER	29
3.1 Upper Dynamic Range Experiments	30
3.2 Materials and Methods.....	31
3.2.1 Animal Experiments	31
3.2.2 Temperature Control.....	31
3.2.3 Dosage.....	31
3.2.4 Anesthesia.....	31
3.2.5 Injection	31
3.2.6 Example Calculation.....	32
3.2.7 Discussion.....	33
3.3 Lower Limit of Detection	34
CHAPTER 4 DEVELOPMENT OF AN ENERGY DISPERSIVE X-RAY FLUORESCENCE (EDXRF) TECHNIQUE FOR ELEMENTAL ANALYSIS OF GOLD NANORODS	36
4.1 Introduction and Specifications	36
4.2 Materials and Methods.....	37
4.2.1 Animal Experiments	37
4.2.2 Temperature Control.....	37
4.2.3 Dose Groups.....	37
4.2.4 Anesthesia.....	37
4.2.5 Injection	38
4.2.6 End of Experiment and Organ Collection.....	38
4.2.7 EDXRF Sample Preparation.....	38
4.2.8 Data Analysis	39
4.3 Results.....	40

4.4 Discussion.....	41
4.5 Review of Specifications	43
CHAPTER 5 USE OF REAL-TIME PHARMACOKINETICS TO PREDICT TUMOR UPTAKE OF GOLD NANORODS	44
5.1 Introduction and Specifications	44
5.2 Materials and Methods.....	47
5.2.1 Experimental Design.....	47
5.2.1.1 Temperature control.....	47
5.2.1.2 Anesthesia and injection	48
5.2.1.3 Pulse Photometer data collection	48
5.2.1.4 End of experiment.....	49
5.2.1.5 Data analysis	49
5.2.1.6 EDXRF tumor sample preparation	50
5.2.1.7 EDXRF tumor sample analysis.....	50
5.3 Results.....	51
5.4 Discussion and Review of Specifications	55
CHAPTER 6 RETICULOENDOTHELIAL SYSTEM BLOCKADE OF GOLD NANORODS IN A MURINE MODEL.....	60
6.1 Introduction.....	60
6.2 Materials and Methods.....	61
6.2.1 Overview.....	61
6.2.1.1 Temperature control.....	63
6.2.1.2 Anesthesia and injection	64
6.2.1.3 Pulse photometer data collection	64
6.2.1.4 Data analysis	64
6.3 Results.....	65

6.4 Discussion	67
6.5 Review of Specifications	68
CHAPTER 7 USE OF PULSE PHOTOMETER FOR <i>IN VIVO</i> DETECTION OF QUININE	69
7.1 Introduction and Specifications	69
7.2 Materials and Methods.....	71
7.2.1 Instrumentation	71
7.2.2 Algorithm.....	72
7.2.3 Animal Experiments	73
7.3 Results.....	75
7.4 Discussion.....	78
CHAPTER 8 USE OF PULSE PHOTOMETER FOR <i>IN VIVO</i> DETECTION OF AMPHOTERICIN B.....	79
8.1 Introduction and Specifications	79
8.2 Materials and Methods.....	82
8.2.1 Instrumentation	82
8.2.2 Algorithm.....	83
8.2.3 Animal Experiments	84
8.2.4 Blood Analysis.....	85
8.3 Results.....	86
8.4 Discussion.....	87
8.5 Conclusion	88
CHAPTER 9 CONCLUSIONS AND FUTURE WORK	89
APPENDIX A MOUSE BLOOD DRAW PROTOCOL	92
A.1 Theory	93
A.1.1 Finding the Extinction Coefficients for Nanorods	93

A.1.2 Blood Draws and Measurements	94
A.2 Adjustments	95
A.3 Calibration Curve/Typical Results.....	96
APPENDIX B ESTIMATION OF THE LIMITS OF DETECTION OF A LED DETECTOR COMBINATION	97
APPENDIX C AVERTIN ANESTHESIA (2,2,2-TRIBROMOETHANOL)	100
C.1 Contraindication	101
C.2 Materials.....	101
C.3 Avertin Stock Solution.....	101
C.4 Avertin Working Solution.....	102
C.5 Animal Injection.....	102
APPENDIX D INSTITUTIONAL ANIMAL CARE AND USE COMMITTEE APPROVAL LETTERS.....	103
APPENDIX E INDIVIDUAL BIOAVAILABILITY CURVES OF MICE USED IN CHAPTER 7.....	106
APPENDIX F SAMPLE BIOAVAILABILITY CURVE OF MOUSE USED IN CHAPTER 8.....	109
APPENDIX G DESCRIPTION OF THE LOESS SMOOTHING FUNCTION	111
BIBLIOGRAPHY	113

LIST OF TABLES

Table 1-1: List of design specifications and rationale outlined in Section 1.5	11
Table 4-1: Summary of Chapter 4 specifications.....	43
Table 5-1: Half lives for all mice in study (n = 17). Dose group A (9 μ L/gm, n = 8) and dose group B (4.5 μ L/gm, n = 9) with averages and standard deviations	53
Table 5-2: Population pharmacokinetic parameter estimates from the final 2-compartment model	54
Table 5-3: P-values for comparison of pharmacokinetic and accumulation parameters between dose groups A and B.....	56
Table 5-4: Review of specifications.....	60
Table 6-1: Review of specifications.....	69

LIST OF FIGURES

Figure 1-1: A conceptual schematic of the sources of absorption of light as measured by the pulse photometer.	3
Figure 2-1: A schematic of the circuitry and software interface of the pulse photometer. Channels 1, 3 and 5 carry the information for the three wavelengths, and channel 7 is not used; “sub” is the background subtraction channel. “LPF” represents low pass filters with a cutoff of 29Hz.....	22
Figure 2-2: Schematic demonstrating one compartment model.	25
Figure 3-1: The bioavailability curve of a naive BALB/c mouse (first injection at around 18 mins, and an injection every five minutes. The graphed data represents the data with artifacts removed (using MATLAB code). The average of upper limit of detection of the device was found to be 7.94 optical density (n=3).	32
Figure 4-1: A raw spectrum of a sample from the calibration set (PPM value = 21.73). Vertical lines from left to right: Zn K_{α}^1 line (8.631 Kev), Zn K_{β}^1 line (9.572 Kev), Au L_{α}^1 line (9.711 Kev), Au L_{β}^1 line (11.439 Kev), Br K_{α}^1 line (11.907 Kev). These lines contribute to counts at each given energy.....	39
Figure 4-2: EDXRF Calibration. This graph demonstrates the raw calibration points (\square), used calibration curve (dashed line), and individual tumors (\circ).	41
Figure 5-1: The graph of the peak intensity vs. concentration of gold in tissue for a sample of the Calibration data (Δ) from Figure 4-1, Experimental group A (x, n = 8), and Experimental Group B (o, n = 9). The linear correlation (dashed line) ($y = 0.07126x + 0.09984$, $R^2 = 0.93$) and 95% prediction interval (solid lines).....	52
Figure 5-2: An example bio distribution curve built from the data taken by the pulse photometer.	55
Figure 6-1: The effect of λ -carrageenan on circulation half-life of nanorods. The half-life for the first injection (without the λ -carrageenan injection) was 58.10 mins. The half-life for the second injection immediately following a λ -carrageenan injection was 110.55 mins.....	66

Figure 6-2: The circulation half-life of nanorods after a λ -carrageenan injection. It was observed that the peak concentration of the nanorods was not affected after the injection of λ -carrageenan, while the clearance slowed down and, thus circulation half-life went up..... 67

Figure 6-3: The elongation of circulation time of nanorods after the introduction of λ -carrageenan into the circulation..... 68

Figure 7-1: The pulsatile part of the photoplethysmogram signal (a) before injection (b) during and after injection. The ratiometric measurements of the three channels (with $V_{p-p} > 5\text{mV}$) were collected and used to calculate the *in vivo* concentration of quinine. 76

Figure 7-2: The real-time *in vivo* concentration of quinine in blood. The graph is divided into three parts: (1) Background data from pre-injection phase (2) The rising concentration during the injection (3) The decay phase after the end of the injection..... 77

Figure 7-3: The comparison between the results of blood analysis (UV/Vis) and the PPG readings of intravenously injected quinine. The graph represent the PPG readings that were taken at different time points after the injection, plotted against the UV/Vis analysis of the blood draws at the same time points (n = 3 mice, 8-9 points from each mouse). Linear fit resulted in a straight line with the equation: $y = 1.032x - .1604$ 78

Figure 8-1: Bioavailability curve of Abelcet® *in vivo* as measured by the PPG ($R^2 = 0.95$) and the blood draws by UV/Vis analysis ($R^2 = 0.93$). The values were then fitted to a single decay exponential model to obtain half-lives. (UV/Vis = 355 min, PPG = 398 min.) 87

Figure 8-2: The comparison between the results of blood analysis (UV/Vis) and the PPG readings for intravenously injected Abelcet®. The graph represent the PPG readings that were taken at different time points after the injection, plotted against the UV/Vis analysis of the blood draws at the same time points (n = 3 mice, 7-8 points from each mouse). Linear fit resulted in a straight line with the equation: $y = 0.85x + 0.41$ 88

Figure A-1: Extinction spectra of blood prior to (raw blood) and post (all other spectra) injection. Note how the extinction at 760 nm increases greatly in comparison to 940 nm and then begins to return to a spectrum more like that for raw blood. 96

Figure A-2: Calibration curve comparing the calculated nanoshell concentration in samples containing blood and nanoshells to samples containing only known concentrations of nanoshells. The equation of the linear fit is $y = 0.6671x + 5E+08$ 97

Figure E-1: Bioavailability curve of quinine *in vivo* as measured by the PPG ($R^2 = 0.989$) and the blood draws by UV/Vis analysis ($R^2 = 0.943$). The values were then fitted to a single decay exponential model to obtain half-lives in Mouse 1 108

Figure E-2: Bioavailability curve of quinine *in vivo* as measured by the PPG ($R^2 = 0.985$) and the blood draws by UV/Vis analysis ($R^2 = 0.971$). The values were then fitted to a single decay exponential model to obtain half-lives in Mouse 2 108

Figure E-3: Bioavailability curve of quinine *in vivo* as measured by the PPG ($R^2 = 0.987$) and the blood draws by UV/Vis analysis ($R^2 = 0.954$). The values were then fitted to a single decay exponential model to obtain half-lives in Mouse 3 109

Figure F-1: Bioavailability curve of quinine *in vivo* as measured by the PPG ($R^2 = 0.952$) and the blood draws by UV/Vis analysis ($R^2 = 0.931$). The values were then fitted to a single decay exponential model to obtain half-lives in Mouse 1. 111

ACKNOWLEDGMENTS

I would like to thank my committee: Dr. Patrick O'Neal, Dr. Katie Evans, Dr. Leon Iasemidis, Dr. Sandra Zivanovic, and Dr. Steve A. Jones. All the members of my committee were always helpful, not only with their time in the dissertation proposal and defense process, but also in experimental advice throughout my graduate career. I found that I communicated with each member of my committee regularly (compared to some of my peers, which is rare), which was extremely helpful for me throughout my time in the graduate program at Louisiana Tech. I would also like to thank the members of the Nano Cancer Therapy and Sensing Group Lab over the last six years for their help and input and discussion in the lab meetings for experimental design and data analysis.

In addition to the help of my committee, I would like to thank Dr. Sven Eklund for his help in the development of a new rapid elemental analysis protocol used for some of the experiments included in this body of work, and Dr. James Spaulding for his help with the IACUC committee and his advice with the animal work.

The collaborative efforts of Nanospectra Bioscience, Inc. made my graduate work possible. The help from the team (including Dr. Jon Schwartz, Dr. Glenn Goodrich, and Kelly Gill-Sharp) in experimental design, troubleshooting, training, and general advice was invaluable.

CHAPTER 1

INTRODUCTION

1.1 Photoplethysmography and Monitoring of Nanoparticles and Other Drugs

The medical advances in recent decades can be described in terms of the development of personalized or individualized diagnostic and therapeutic techniques which address “the great variability among individuals” [1]. This recent drive towards personalized medicine, suggests the need for near-real time clinical evaluation of the progression and efficacy of therapies. The progression of medicine, especially the clinical processes that involve drug delivery, has evolved to a point where quantitative assessment of various factors is considered critical to the outcome of the therapy. Since each individual reacts differently to a particular drug, and there is significant patient-to-patient variability, even within a small group of patients, real time monitoring of and verification of pharmacological variables such as dose, circulation, and clearance, is necessary. This type of monitoring is particularly important in the case of drugs which carry harmful side effects in case of overdosing.

In an effort to verify the dose, and investigate the real time *in vivo* circulation of optically resonant gold nanorods, a non-invasive optical device was developed [2], [3]. The device, referred to as a pulse photometer, uses the technique of multi-wavelength

photoplethysmography, which is the basis of instrumentation in pulse photometry, and pulse dye densitometry.

Using the pulse photometer, we were able report the circulation of gold nanorods and oximetry for six hours post-injection in mice with no anesthesia. The initial rationale for developing this type of instrument relates to the need for increased quality and reproducibility of nanoparticle-based therapies. The driving rationale was that the important step towards the clinical utility of these nanoparticles is to verify that the nanoparticles have been delivered to the blood at the expected dose and have an adequate circulation time so that they have the opportunity to accumulate at the target sites. This data could also lend credibility to other metrics showing the nanoparticles had been manufactured according to specifications.

1.2 Photoplethysmography, Beer-Lambert's Law and Optical Density

The plethysmogram is a physiological signal that arises from the small change of volume in tissue due to a pulsatile phenomenon. This signal can be measured using light by measuring small changes in its reflection or transmission. Measuring this signal using the technique of detecting light is called photoplethysmography (PPG) and this technique has been utilized in many medical applications and this technique has been developed over the past few decades [4].

Since the optical properties of the pulsatile tissue are determined by looking at the individual components of the signal, PPG can be used to gain spectral information about the pulsatile constituents of the tissue. A mass of tissue perfused with blood will contain

optically extinguishing components that are relatively constant in volume (such as muscle, bone, and venous blood), and pulsing arterial blood.

When we examine the small changes in the attenuation of light interacting with the tissue, the contribution of only arterial blood is isolated from the other components by isolating the pulsatile part of the signal as shown in Figure 1-1.

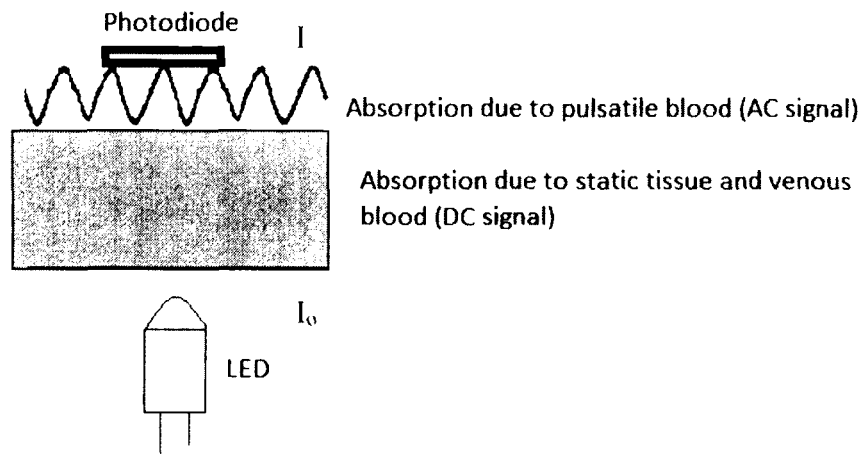


Figure 1-1: A conceptual schematic of the sources of absorption of light as measured by the pulse photometer.

It is for this reason that PPG is applicable to the analysis of the optically extinguishing properties of arterial blood. A graphical illustration of the transmission mode measurement of this pulsatile nature of tissue can be seen in Figure 1-1. In the preceding figure, if we consider I_0 to be the intensity of light of a single wavelength entering the tissue, and I be the intensity of light that reaches the detector, then the absorption of light (A) caused by the tissue is defined as:

$$A = -\ln\left(\frac{I}{I_0}\right). \quad \text{Eq. 1-1}$$

Beer-Lambert's Law states that the intensity of light decreases exponentially as a function of depth and photon attenuation by the material. Therefore, the absorbance of

photons in an absorptive medium for a particular wavelength is defined as the absorbance (equivalent to absorption defined above), which is:

$$A = \epsilon \cdot c \cdot d, \quad \text{Eq. 1-2}$$

where ϵ = molar extinction coefficient of the material for that wavelength.

c = concentration of the absorptive material.

d = thickness of the sample (path length).

In this case, we ignore specular reflection and combine absorption and scattering into one term, the equation can be rearranged in terms of the total extinction, which is represented by the quantity A . Since it is a ratio of intensities, the measured value extinction for a specific wavelength is unitless. This value is also known as the optical density of the sample. In conventional spectroscopy, because of the size of the cuvettes (sample holders) used, the value is typically defined as optical density/cm or optical density/mm.

The PPG quantifies the concentration using the Beer-Lambert Law and the principles of pulse oximetry theory, focusing on the absorption due to the pulsating medium measured in a vascularized mass of tissue. The particular descriptions of the theory behind the operation of the device is further explained in Section 2.2. This was implemented to find the concentration of gold nanoshells *in vivo* in murine models across the therapeutically relevant concentration range [2]. The device uses off-the-shelf optoelectronic components in conjunction with a LabVIEW virtual instrument (VI) with an algorithm based on Beer-Lambert's Law in a multi-spectral method designed to elucidate the concentration (in optical density) of oxy- and deoxy-hemoglobin and the nanoparticles simultaneously in the blood. This device was reported to measure the

optical density of particles that are absorbent between 600 – 940 nm, longer than the major absorptive bands of hemoglobin [3].

Expanding on the current application of the pulse photometer, the prototype was modified to monitor the *in vivo* circulation of other clinically relevant molecular drugs in real time. It was decided to examine quinine and amphotericin b, focusing on the current clinical needs related to maintaining the dose within the therapeutic window and concerns of potential toxicity [5] and the widespread application of these drugs. The rationale was to improve treatment reproducibility as we precisely control and verify the delivered dose. In addition, we also aimed to quantify the clearance properties of the drug in real-time allowing for better control of the dose within the therapeutic window. This report presents the feasibility test of the system to quantify the concentration of quinine, delivered intravenously at a therapeutically relevant dose.

1.3 Application of Nanoparticles in Development for Cancer Therapies

Empirical evidence has shown that cancer manifests itself as solid tumors about 85% of the time, and therefore, solid tumors are an area of interest for a lot of research [6]. The successful outcome of tumor treatments often depends on physicians' experience and available techniques because of lack of quantifiable metrics in the diagnostic and treatment phase [7], [8]. Although survival rates have improved over the past few decades, with a one-year's survival rate going from 69.9% in 1975 to 81.8% in 2008, and a 10 year survival rate going from 41.9% in 1975 to 60.6% in 1999, much of cancer therapy relies on qualitative assessment of progression of treatment parameters [9], [10], [11]. During the treatment, if surgical removal is not feasible for tumors that lie near

sensitive tissues, such as head, neck, and brain, or those that have metastasized, the treatment is continued with radiation or chemotherapy [12]. Chemotherapy usually involves intravenous injection of a therapeutic drug (which is generally toxic) and relies on the high metabolic activity of tumors to absorb the chemotherapeutic agent quickly [13]. In recent years, research has been done towards the efficacy of less systemically toxic chemotherapy drugs, and Herceptin was found to exhibit very little toxicity in human trials [14]. However, the uptake and retention of traditional chemotherapeutic small/macro-molecules can be hindered by several physiological factors in the tumors [15], which in turn might lead to side effects.

The high influence of local physiological factors on drug uptake caused the scientific community to study the anatomical and physiological characteristics of tumors in recent decades [16], [17], [18]. However, these characteristics vary with tumor size, type, and location [19], [20], and identifying usable metrics that help in specific drug or nanoparticle design have been difficult to achieve. Although many empirical studies have pointed to different factors that influence uptake in some tumors [21], these studies do not necessarily apply to other particles or conditions.

Custom designed nanoparticles have recently emerged as a powerful tool in many biomedical applications [22, 23]. In particular, several classes of nanoparticles have been employed as cancer therapy agents [24]. These particles can have architectures of varying complexity, achieved by various chemical techniques usually performed in specific sequences to add complexity and functionality, depending on their specific applications, some of which are described further.

One class of nanomaterials used for drug delivery are hydrogels, which are networks of cross-linked polymer chains that are hydrophilic and are commonly used as tissue scaffolds. Several studies have been conducted using cross-linkers that will degrade under specific conditions (such as change in pH, or temperature), usually to release an encapsulated drug. Tauro *et al.* have demonstrated potential use of poly (ethylene glycol) diacrylate (PEGDA) hydrogels to deliver chemotherapeutic agents to highly specific sites, and for use in treatment of glioblastoma [25].

Polymeric nanoparticles are developed and are similar in nature to the hydrogel nanoparticles in the manner of drug release. The polymeric nanoparticles are being made from polymers which erode under certain conditions to release an encapsulated drug and then disappear. Poly (ϵ -caprolactone), poly (lactic acid), poly (glycolic acid) and their copolymers are a few examples of the polymers under investigation for use in cancer therapy. The use of polymeric nanoparticles could help in the location specific delivery of chemotherapeutic agents, decreasing systemic toxicity, and improving patient outcomes [26].

Liposomes consist of a lipid bilayer and are usually spherical, creating a hollow core used for the encapsulation of drugs. This method is advantageous because it takes advantage of the ability of liposomes to preferentially accumulate in tumors due to the Enhanced Permeability and Retention (EPR) effect. This preferential accumulation in tumors allows for the control of the dosage of the encapsulated chemotherapeutic agent, enabling it to be given in lower doses, and be less systemically toxic while retaining the desired concentration and effect in the target tumor. Liposomes also allow for the control of characteristics such as bioavailability, size, drug release rate, and dosing schedule,

which gives them a lot of flexibility in their application. In 1990, The United States Food and Drug Administration (USFDA) first approved this type of therapeutic agent as DOXIL (liposomal doxorubicin) [27]. Some of the nanomaterials currently found in the market for cancer therapies are nanocarrier-based drugs. A few examples are Zevalin, Bexxar, Myocet, Zinostatin, Stimalmer, Oncaspar, Ontak, and Abraxane, which are drug carriers that include protein conjugates, immunoconjugates, and liposomes [28].

Additional types of metal nanomaterials, such as Auroshells (gold nanoshells) and Combidex (iron oxide nanoparticles), are currently undergoing clinical trials for cancer therapy [29]. Gold nanoparticles have unique optical properties that allow for non-invasive, real-time monitoring of nanoparticle concentration in the blood [30], [2], [3].

Metrology and imaging technologies that are capable of quantitatively characterizing the properties of the nanoparticles have enabled the development of the first round of nanomedical technologies at an experimental or prototype level. However, the key characteristics that make a type of nanoparticle treatment successful are yet to be recognized. Most of the current research in nanoparticle based therapy is focused on various applications of the nanoparticles for very specific purposes. Most of the *in vivo* characteristics are interactions of different kinds of particles have yet to be studied.

Although many nanoparticles are increasingly being manufactured for various purposes, with variations in size, shape, surface charge, surface coatings, ligands, depending upon the application, the physiological conditions that affect the accumulation and ultimately efficacy of the therapeutic agents are rarely investigated.

Whatever type of nanoparticle is chosen, the efficacy of the treatment is determined by the ability to exploit the natural differences between cancerous and healthy

tissue for the selective delivery to tumor cells in order to reduce damage to healthy cells. Most solid tumors are characterized by an abnormal vasculature and the lack of functioning lymphatic vessels [16]. Studies have demonstrated that the vasculature of some tumors is quantifiably different from normal tissue in terms of permeability, size, the lack of a complete basement membrane, and abnormally large inter-endothelial junctions [6], [16], and these differences are commonly exploited for passive delivery of therapeutic agents via the enhanced permeability and retention effect (EPR). Thus, a careful study of all these factors is important in order to take better advantage of those properties resulting in an increased delivery while minimizing the effect of those that would make the delivery less effective.

1.4 EPR Effect and Passive Targeting

The EPR effect is a commonly found defect in the vessel walls of the tumors. It is caused by the high metabolic and growth rate of the tumor tissue compared to the healthy tissue. The high demands of nutrients in the tumor leads to rapid expansion of vasculature along the tumor, which is aided by the secretion of various growth factors, which is largely unregulated by the body. This lack of regulation leads to poorly formed vessels and defective basement architecture allowing larger particles and molecules to escape the vasculature in these areas. This also caused the lymphatic drainage in areas around the tumor area to be sub-optimal. These larger particles are not able to escape the well-formed (healthy or non-tumorous) vasculature [31]. Passive tumor targeting is a technique to target tumors with therapeutic agents with the aid of the EPR effect. This effect, in combination with the poor lymphatic drainage, creates an environment where specifically sized particles can preferentially accumulate, compared to normal tissue.

Different modeling efforts in the past have suggested that the pore size is more important than the particle size for effective extravasation [32]. Reports have suggested that pore size can be effectively modified by several methods including hyperthermia [32], [33].

1.5 AuroShell® Gold Nanoparticles

AuroShell® Particles are spherical particles with a dielectric core with a thin gold shell. The ratio of core to coating gives the nanoshell's tunable optical properties [34]. These particles (diameter of approximately 155 nm) and nanorods (14 x 45 nm) have demonstrated utility in cancer therapies through the use of the tunable optical properties. The therapy involves the intravenous injection of gold nanoparticles and passive accumulation in tumor tissue. Once accumulation is complete, the particles are exposed to a specific wavelength of light (by fiber optic), which excites and heats the nanoparticles, killing the tumor. This photothermal ablation of the tumor has two major advantages: killing the tumor along vascular lines (cutting the tumor off from its source of nutrients) and preferentially killing the tumor to minimize damage to healthy tissues surrounding the tumor. Once the tumor dies, the cells are disposed of by the immune system [34]–[36]. These plasmon resonant gold nanoparticles are used in tumor treatment and as contrast agents and have specific optical properties in the near infrared spectrum making them ideal for modern cancer therapy and optical imaging [37]. In the treatment of tumors, it is essential that nanoparticles be designed that will effectively deliver treatment, whether it is a drug or the nanoparticle itself, to the tumor preferentially to avoid collateral damage to normal tissue. So, the first step towards ensuring the preferential accumulation of these nanoparticles is to make sure that the nanoparticles have a long enough circulation time so that they can be accumulated at the target sites.

1.6 Research Need and Presented Research

The research plan was proposed with the previously described clinical need and concerns, which gave rise to certain specifications to the instrumentation to be implemented, which are summarized in Table 1-1.

Table 1-1. List of design specifications and rationale outlined in Section 1.5.

Objective	Clinical need	Design Specification
Model to relate pharmacokinetics with treatment variability	Address the patient-to-patient variability (in terms of dosage, bioavailability, and uptake) in therapeutic nanoparticles.	Develop a population model for gold nanoparticles to establish a relationship between dose, bioavailability and accumulation in the tumor.
	<u>Elemental Analysis</u> Develop a method to rapidly quantify the accumulation of gold nanoparticle in the tumor.	Develop a protocol for elemental analysis of gold in tumor tissue using EDXRF (Energy Dispersive X-Ray Fluorescence), sensitive in the 0-50 ppm range, rapid enough to inform a clinical decision (24-48 hours).
Reproducibility of treatment	<u>Dose verification</u> Provide real-time assessment of the delivery of dose in gold nanoparticle therapy.	Use of novel multi-wavelength photoplethysmograph for direct dose verification and real-time <i>in vivo</i> sensing of circulating nanoparticles.
	<u>RES modulation</u> Provide a means to modulate the AUC and clearance to increase exposure time of nanoparticles.	Develop a safe protocol for temporary RES blockade, for the modulation of AUC and, eventually to increase treatment efficacy.
Expansion of application	Expand the application of the current prototype into real-time detection of other clinically relevant molecular drugs.	Modify the current prototype to detect real-time <i>in vivo</i> detection of anti-malarial quinine and anti-fungal amphotericin b, within the limits of their clinical doses.

One important issue to address in nanoparticle therapy is the immune response of the body after the *in vivo* application. Unmodified nanoparticles, when introduced to the body intravenously, will elicit an immune response resulting in rapid removal. Depending on the size and composition of the nanoparticles, this can be either via renal excretion if the particles are small enough, or cell mediated by the reticulo-endothelial system (RES). Primarily, the nanoparticles are removed from the vasculature by tissue macrophages in the liver and spleen called Kupffer cells. These cells can quickly identify and eliminate nanoparticles via phagocytosis [38]. The rapid removal of nanoparticles from the bloodstream limits their potential application in control target delivery [39]. Although the attachment of PEG has been shown to increase the circulation time of several types of nanoparticles dramatically [40], which is usually reported as the circulation half-life of the particle assuming an exponential decay in concentration over time, a detailed model-based study over the dynamics of circulation of these particles in the body has not been conducted yet. A detailed study that investigates the effect of various hemodynamic variables on the final accumulation of the tumor has not been performed.

In addition to several clinical factors that affect tumor uptake, researchers need to know the bioavailability and bio distribution of the nanoparticles in order to ensure that they reach the target site, for which the real time monitoring of the nanoparticles *in vivo* is required. A potential way to enhance the outcome during therapy is to increase feedback through additional clinical signs during the accumulation and treatment phases. Nanoparticle systems can be coupled with individualized pharmacokinetics and elemental analysis of *ex vivo* tissue to confirm uptake and retention into the tumor. Concurrently, innovative medical devices are being developed to provide near-instantaneous

pharmacokinetic feedback [35], suggesting the need for an elemental analysis technique that provides similarly rapid quantitative feedback of biodistribution. These analyses could assess when, and to what degree, the particles were accumulating in the tumor, or if they were being eliminated by the reticuloendothelial system (RES). The use of rapid elemental analysis coupled with real-time pharmacokinetic measurements could help predict the most appropriate time for animal or human ablation (e.g. photothermal) of the tumor. For animal studies, a faster technique can have a major impact for companies involved in nanomaterial quality control and product development.

Over the years, different *ex vivo* techniques have been implemented to monitor the nanoparticle accumulation and distribution in the body. The standard accepted method of determining gold concentration is considered to be Instrumental Neutron Activation Analysis (INAA), which has been shown to be effective in determining the bio distribution of gold nanoshells [41]. However, this technique is not useful for a clinical setting because of the time delay (up to two weeks) in the processing and analysis of the samples, whereas during patient care and treatments, almost instantaneous quantitative values are needed to make a decision on treatment. We posit that the Energy Dispersive X-Ray Fluorescence (EDXRF), with a suitable sample preparation and handling protocol, will be a suitable method for *ex vivo* analysis of gold nanoparticles in biopsy samples in a clinically relevant time frame.

Since the particles are optically active, their optical absorbance and scattering properties can be exploited to monitor them [42]. This method applies Dynamic Light Scattering (DLS) to correlate the ration of the scattering of the signal from a sample to a known concentration of nanoparticles. Similar technique can be applied using a UV/ Vis

spectrometer by correlating the absorbance with the concentration. Recently, a novel device that uses multi-wavelength pulse plethysmograph, based on Beer-Lambert's Law of highly scattering medium, was designed to determine the optical density of a pulsating medium was successfully implemented to find the concentration of gold nanoshells *in vivo* in murine models [43]. This device uses off-the-shelf optoelectronic components in conjunction with a tailor-made LABVIEW VI with an algorithm based on Beer-Lambert's Law and pulse oximetry theory to calculate real time optical density of nanoparticles in the blood. Currently, this device is able to measure the optical density of particles that are absorbent at the near infra-red band of the spectrum [44]. This prototype is able to work with various therapeutic particles to track the concentration of *in vivo* gold nanoparticles in real time.

This research plan utilizes gold nanoshells as currently used in clinical investigations in the United States (Investigational Device Exemption 070090) and spectrally similar gold nanorods, and other optically active therapeutic agents. The objective of this work will be the application of pulse plethysmographic system for a broad-based pre-clinical and clinical use toward the control of intravenous drugs into the target sites. In the context of nanoparticles, the relationships between the variations in therapeutic dose and treatment efficacy have not been firmly established in the literature. This project will also help develop a pharmacokinetic population model which could be used to predict accumulation for selected doses and injection patterns based on a larger data set [45]. Working with the assumption that increased circulation and AUC are major contributing factors that influence tumor uptake, this project will investigate the effect of compounds that suppress RES function when used in conjunction with nanoparticle

injections. Working towards improvement of clinical impact of nanoparticle therapy, this project will develop a method of rapid analysis of tumor particles to assess accumulation within a clinically relevant time frame. In addition, this research aims to expand the application of the photo plethysmograph into real-time sensing of circulation of other optically active molecular drugs.

In addition to assessing the effect of AUC on tumor uptake, this research will aim to increase the efficacy of nanoparticle based therapy by increasing the *in vivo* circulation half-life, thus providing a longer exposure time of the therapeutic nanoparticles. Since the Kupffer cells of the liver provide a major removal route of nanoparticles by the RES, an effective RES blocking agent should enable longer circulation of the nanoparticles *in vivo*. This research aims to demonstrate the use of λ -Carrageenan (linear sulphated polysaccharide) to suppress the actions of the RES, and allow for longer circulation of gold nanoparticles temporarily.

As the research strives towards the determination of the best clinical and physiological parameters for optimum dose delivery, the experiments are designed to approach the problem from different areas. This project was started with two major aims that would demonstrate the potential benefits of integrating the pulse photometer with an established nanoparticle-based cancer therapy. The aim is to improve treatment reproducibility as we precisely control and verify the delivered dose. This objective was expanded to encompass other clinically relevant drugs like quinine and amphotericin b, by making modifications to the prototype. The results of each unique experiment were used to construct a standard one compartment pharmacokinetic model. The employment of near real-time pharmacokinetics was done to investigate the physical response to

nanoparticles and other intravenously injected particles, giving us the ability to make rapid recommendations on treatments. In accordance with the purpose of clinically relevant feedback, an EDXRF elemental analysis protocol was developed to quantify the accumulation of therapeutic gold nanoparticles in target tissue in a clinically relevant time frame.

The body of research presented in this dissertation is the product of iterative and improvements to develop protocols rapidly for use in translational pre-clinical trials using gold nanorods. The work started with the purpose of the implementation of the novel pulse photometer in a clinical setting in order to help health care providers make informed decisions based on rapid feedback on nanoparticle treatment. In order to achieve that goal, proper calibration with existing standards and establishing the working range of the pulse photometer was required (as described in Chapter 3: Calibration and Determination of Operational Range of the Pulse Photometer).

After implementation of the pulse photometer, the focus of the research was to assess the efficacy of the treatment in terms of some quantifiable metric, which in this case was the final accumulation of the gold nanoparticles in the tumor. Based on the premise that real time knowledge of bioavailability of the nanoparticles during the injection phase should inform the outcome (i.e. final accumulation in the tumor), experiments were conducted to investigate the predictability of the final accumulation based on the bioavailability of the nanorods, as described in Chapter 4: Use of Real-Time Pharmacokinetics to Predict Tumor Uptake of Gold Nanorods. The initial experiments of 0: Use of Real-Time Pharmacokinetics to Predict Tumor Uptake of Gold Nanorods revealed a need to develop a rapid elemental analysis system to be able to observe a full

set of data on one animal prior to the beginning of an experiment on another animal (and for future clinical work). This need for a rapid elemental analysis system leads to the work in Chapter 4: Development of an Energy Dispersive X-Ray Fluorescence (EDXRF) Technique for Elemental Analysis of Gold Nanorods, and this novel rapid elemental analysis technique was used in the revised experiments of the Chapter 5: Use of Real-Time Pharmacokinetics to Predict Tumor Uptake of Gold Nanorods. The data from these experiments was used to investigate the effect of adjuvant therapies in the circulation of nanorods during the accumulation phase. Exploring this possibility led to application of reticuloendothelial system (RES) blocking agent to achieve longer circulation times, which is described in Chapter 6: Reticuloendothelial System Blockade and Redosing of Gold Nanorods in a Murine Model. In addition, the possibility of expanding the application of the novel pulse photometer in *in vivo* sensing of other clinically relevant molecular drugs (quinine and amphotericin b) was explored, the details of which are described in Chapter 7 and Chapter 8, respectively.

The objective of this research is to facilitate improvement in clinical outcomes with the use of real time data to inform point of care decisions. The rationale of these studies was to demonstrate that dose verification, population pharmacokinetic modeling, and protocol modifications will be instrumental in informing clinical decisions, which then will improve efficacy of any treatment. Using tools such as pulse plethysmography instrumentation for dose verification and drug sensing, and EDXRF for rapid quantification for population modeling, efforts can be made to address variability among individuals, and increase reproducibility in treatment outcomes.

CHAPTER 2

LITERATURE REVIEW

As the nanoparticles were ready for therapeutic use in the clinic, the need for their real time monitoring was realized. The need for instrumentation for the real time sensing and the development of the pulse photometer, which was useful in determining the real time bioavailability of the nanoparticles. In addition, a pharmacokinetic model was needed to establish a relationship between different pharmacokinetic variables and final accumulation in the target organs (tumor). The data required to establish such a model needed a method of elemental analysis of gold in the tumors, which was achieved by developing a new EDXRF protocol for analysis of gold in the tissue. This chapter provides some background on the current state and the research needed on the therapeutic nanoparticles, their clearance from the body, and the development of pulse photometer for real time monitoring of nanoparticles in the body, and the development of a new EDXRF protocol for analysis of gold in the tissue for use in development of a population pharmacokinetic model.

2.1 Gold Nanoparticles

The gold nanoparticles (nanoshells and nanorods) discussed in this dissertation were provided by Nanospectra Biosciences, Inc. (NBI). Their nanoshells are currently in pre-clinical and clinical trials under an investigational device exemption (IDE). These

nanoparticles do not chemically interact with the body and are therefore classified as devices instead of drugs. The nanoshells are approximately 150 nm in diameter with a mPEG coating, stored in an iso-osmotic solution of 10% trehalose, and produced in the manner described by Oldenberg *et al.* [46], [47]. Biodistribution of these gold nanoshells has been previously conducted where James *et al.* demonstrated that at 24 hours, the gold was primarily accumulated in the organs of the RES [47].

The gold nanorods provided by NBI are approximately 15 x 45 nm, PEGylated, and suspended in an iso-osmotic solution of 10% trehalose. The nanorods are synthesized using a modified version of the method developed by Jana *et al.* [48]. Biodistribution of these gold nanorods has been conducted. Goodrich *et al.* demonstrated the primary accumulation of gold after 24 hours was in the organs of the RES (liver approximately 77% of injected dose and spleen approximately 6% of injected dose) [36]. Optical coherence tomography was used to monitor the accumulation and dissipation in mammary tumors PEGylated gold nanorods of similar size, the maximum accumulation was found to be at 16 hours [49].

2.2 Clearance of Gold Nanoshells and Nanorods

Nanoparticles, when circulating *in vivo*, are subject to rapid opsonization. The Kupffer cells (tissue macrophages of the liver) are unable to detect foreign bodies in the blood directly, so this process requires the opsonization of the nanoparticles while they are circulating. This opsonization is followed by removal from the blood by macrophages of the reticuloendothelial system (RES) within seconds of injection. This rapid clearance causes very short half-lives, which is incompatible with passive targeting [50], [51]. This problem is avoided by coating the nanoparticles with chemicals such as poly ethylene

glycol (PEG) to “stealth” them from the immune system effectively until they have reached their target.

Charged and metal particles are more rapidly and efficiently cleared by the RES compared to electrically neutral particles. This fast clearance created a need to make the particles electrically neutral or hide the particles by adding a surface coating [31]. Masking nanoparticles from the RES is necessary to increase the circulation time to a period long enough for passive accumulation, which led to the application of nanoparticle coatings to mask the nanoparticles from the immune system. The most common surface coating for stealth nanoparticles is polyethylene glycol (PEG). PEG uses steric hindrance to prevent the adsorption of opsonins and delaying the uptake by phagocytic cells. PEGylation of nanoparticles is a common method of evasion of the immune system and used in liposomes, polymeric nanoparticles, and gold nanoparticles. A form of PEG (DSPE-PEG) has been used to suppress opsonizing proteins, and chol-PEG or PE-PEG has shown a concentration dependent ability to inhibit binding of nanoparticles with immunoglobulins, and almost eliminate the binding at large concentrations [51].

2.3 Pulse Photometer

Optical methods have recently been explored as a method for monitoring the *in vivo* activities of gold nanoparticles [52-54]. This is made possible because the energy most attenuated by these nanoparticles resides in the region of wavelengths (700-1100 nm) known as the tissue optical window. It is in this band that hemoglobin, a primary absorber in vascular tissue, along with melanin and water, demonstrate extinction minima and thus *in vivo* penetration depth is maximal. The spectral analysis of arterial blood has been employed in applications like photoacoustic tomography [55] oximetry [56],

glucosimetry [57], and pulse dye densitometry [58-61]. These methods isolate the time-varying attenuation of light resulting from the arterial pulsation of each heartbeat.

A photodetector circuit is used to detect the amount of transmitted light at selected wavelengths by converting it to a time varying electrical signal. This signal is a waveform referred to as a photoplethysmogram (PPG) which consists of a time varying portion (AC) and baseline (DC). The magnitude of the AC signal is the envelope of the PPG and the magnitude of the DC portion is the average value of the PPG.

This allows for an analysis of the isolated optical properties of arterial blood, which change, often drastically, with the addition of optically attenuating agents. Pulse dye densitometry exploits the same phenomena to measure the concentration of a dye injected into the vasculature suggesting that similar techniques could be applied to the monitoring of optically extinguishing nanoparticles. The measurement of optically attenuating species in the blood can be done by employing the Beer-Lambert Law at several wavelengths.

By examining the ratio of the changes in attenuation of light at these wavelengths, the calculations become path-length independent. This suggests, in theory, that the measurements are also independent of anatomical probing location as long as a suitable pulsatile signal is obtained. In pulse oximetry, for example, the ratio of pulsatile changes at a red (λ_1) and infrared wavelength (λ_2) is used to determine the percent oxygen saturation (SpO_2) in arterial blood. These measurements can be made on several anatomical locations including the fingers, toes, earlobes, and noses with little difference in the measured oxygen saturation.

The ratio of these pulsatile changes can be determined using the DC and AC portions of the PPG, which can be equated to small changes in attenuation of light referred to as R [62]. The setup of the instrumentation, the individual channels and the main parts of the experimental setup is shown in schematic form in Figure 2-1.

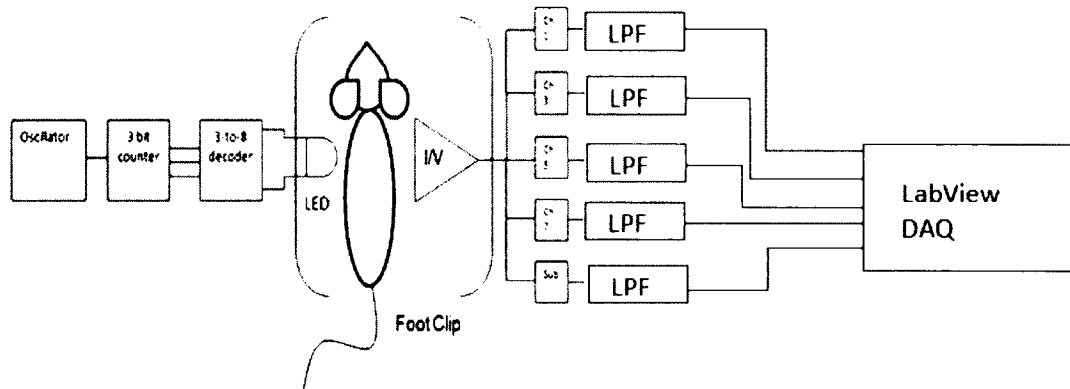


Figure 2-1: A schematic of the circuitry and software interface of the pulse photometer. Channels 1, 3 and 5 carry the information for the three wavelengths, and channel 7 is not used; “sub” is the background subtraction channel. “LPF” represents low pass filters with a cutoff of 29 Hz.

These wavelengths are selected to correspond to the extinction properties of gold nanoshells. The device (shown in Figure 2-1) consists of a probe compatible with mouse anatomy, analog circuitry, a data acquisition card, and LabVIEW software [43].

The probe includes an LED that emits at four unique wavelengths (660, 735, 805, and 940). This LED is purchased through Marubeni out of Santa Clara, California. Only the 805 and 940 nm wavelengths are used in the probe. A photodiode (Hamamatsu Hamamatsu City, Japan) is used on the other side of the subject to record the changes in emitted light through the subject. The additional analog circuitry consists of filtering and timing systems and LED drivers.

The addition of multiple wavelengths to analyze several ratios can be used to determine the concentrations of several optically attenuating species in the arterial blood [64], [65]. This multi-wavelength technique has recently been employed in the improvement of the pulse oximeter to account for the contribution of pulsatile tissue, venous blood, dyshemoglobins, and total hemoglobin concentration [65, 66].

The multispectral pulse photometer is commonly used for mice under light anesthesia or no anesthesia to detect the intravascular concentration of nanorods. The pulse photometer helps by providing the levels of the nanoshells or nanorods in the vasculature displayed as optical density. The pulse photometer does this by observing pulsatile changes in optical extinction between 805 and 940 nm, and calculating a ratio between the wavelengths known as R shown in Eq. 2-1, where V_{AC} is the alternating current voltage, V_{DC} is the direct current voltage, λ_1 is wavelength 1, and λ_2 is wavelength 2:

$$R = \frac{\log\left(\frac{V_{DC}}{V_{DC}-V_{AC}}\right)_{\lambda_1}}{\log\left(\frac{V_{DC}}{V_{DC}-V_{AC}}\right)_{\lambda_2}} \sim \frac{\left(\frac{V_{AC}}{V_{DC}}\right)_{\lambda_1}}{\left(\frac{V_{AC}}{V_{DC}}\right)_{\lambda_2}}. \quad \text{Eq. 2-1}$$

The pulse photometer then simultaneously solves Eq. 2-2 and Eq. 2-3 to solve for the optical density of the nanorods (OD_{NR}), which corresponds to the absorption caused by the nanorods in solution and is concentration dependent, and oxygen saturation (S) both in real time using LabVIEW, using the R (which is the ratiometric value representing the ratio of the absorptions at the wavelengths used, which, in the example demonstrated are 805 nm and 940 nm) values, effective attenuation coefficients of oxygenated whole blood ($\mu_{HbO_2}^\lambda$) at the wavelength of interrogation (λ), and effective

attenuation coefficients of deoxygenated whole blood ($\mu_{\text{Hbr}}^{\lambda}$) at wavelength of interrogation (λ) which can be shown as

$$R_{805/940} = \frac{S(\mu_{\text{HbO}_2}^{805}) + (1-S)(\mu_{\text{Hbr}}^{805}) + \mu_{\text{NR } 805}}{S(\mu_{\text{HbO}_2}^{940}) + (1-S)(\mu_{\text{Hbr}}^{940}) + \mu_{\text{NR } 940}}, \quad \text{Eq. 2-2}$$

and

$$R_{660/940} = \frac{S(\mu_{\text{HbO}_2}^{660}) + (1-S)(\mu_{\text{Hbr}}^{660}) + \mu_{\text{NR } 660}}{S(\mu_{\text{HbO}_2}^{940}) + (1-S)(\mu_{\text{Hbr}}^{940}) + \mu_{\text{NR } 940}}. \quad \text{Eq. 2-3}$$

The use of the pulse photometer allows us to obtain as many data points on the blood plasma concentration curve as needed, thus eliminating the need of blood draws for those estimations. This ability to obtain as many data points as desired is advantageous so we build a more reliable blood plasma concentration curve. Another main advantage of the pulse photometer is the potential for use in near real-time applications of pharmacokinetic models and feedback controls during nanoparticle infusion.

2.4 Pharmacokinetics

Pharmacokinetics is the quantitative study of a drug or a therapeutic particle after it has been introduced into the body until its complete elimination [67]. The pharmacokinetics of the nanoparticles is important because the knowledge about their biodistribution of nanorods informs the outcome of the nanoparticle therapy. Starting with the most basic of pharmacokinetic models, this section discusses two basic models, the one compartment and population pharmacokinetic models.

Physiologically based pharmacokinetic models typically include significantly more compartments to account for more biological systems. De Jong *et al.* conducted biodistribution studies, and demonstrated a presence of gold nanoparticles (of multiple

sizes) in the blood, liver, spleen, lung, brain, heart, and kidney at 24 hours [68]. The pharmacokinetic systems are divided into different compartments for simplicity of modeling, which is typically later verified empirically by animal experimentation. The simple compartmental models we use in this study is one compartmental model, which is described as follows.

2.4.1 One Compartment Model

A one compartment non-physiological based model, is currently being used due to the availability of data. The one compartment model for the experimental data would represent the blood volume of the mouse. Concentration of nanoparticles in the blood volume of the mouse is available in the form of experimental data.

The model uses Eq. 2-4 to give a concentration as a function of time, which can be used to describe several clinical variables related to the injection. A conceptual schematic of the one compartmental model can be seen in Figure 2-2.

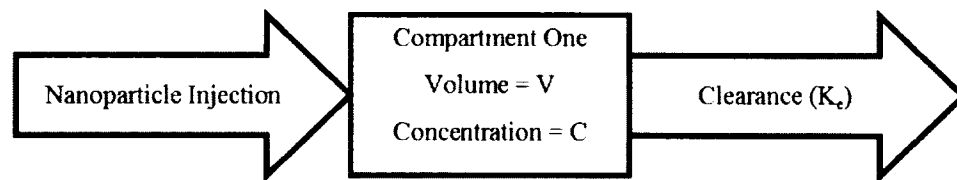


Figure 2-2: Schematic demonstrating one compartment model.

$$C=C_0e^{-k_e t}, \quad \text{Eq. 2-4}$$

where C is the concentration, C_0 is the initial concentration, k_e is the elimination rate constant, and t is time.

The initial concentration is calculated using Eq. 2-5:

$$C_0 = \frac{D}{VOD}, \quad \text{Eq. 2-5}$$

where D is the initial dose and VOD the volume of distribution. Using this basic model, the half-life ($t_{\frac{1}{2}}$) is calculated using Eq. 2-6:

$$t_{\frac{1}{2}} = \frac{\ln(2)}{k_e} = \frac{0.693}{k_e}. \quad \text{Eq. 2-6}$$

This model demonstrates the removal of the nanoparticles from the blood as a function of time, which is defined as a single exponential decay model. This model does not account for differences in the accumulation or release of nanoparticles from tissues, but only the removal of the nanoparticles from the blood. Other models, such as the two compartment physiological models, would provide a better model of the movement of nanoparticles. These models would depend on the availability of real-time data reflecting accumulation in target tissues.

2.4.2 Population Pharmacokinetics

Population pharmacokinetics investigates the variability between patients (or subjects) given the same treatment, also referred to as inter-patient (or subject) variability. The objective of population pharmacokinetics is to account for the inter-subject variability in terms of subject specific variables such as age, sex, or weight. The developed population pharmacokinetics analysis techniques are very valuable in analysis of studies with scarce data. The availability of sparse data in pharmacokinetics led to the development of several analysis techniques such as nonlinear mixed effects modeling, non-parametric maximum likelihood, and Bayesian modeling. These techniques are useful where traditional methods of analyses, which require large data sets, are not.

Nonlinear mixed effects modeling is the most popular method, due in part to the software package NONMEM [69]. Models generated through population pharmacokinetics to have the ability to reveal sub-group specific effects, and covariate effects that can help the clinicians make decisions about the treatment process.

2.5 Elemental Analysis

The application of elemental analysis in nanomedicine stems from the need for feedback to judge the efficacy of the treatment. Different types of metal nanoparticles are employed in nanomedicine for various applications. For example, gold nanoparticles are being used in animal and human trials for assessing the feasibility of photothermal ablation of inoperable solid tumors [28], [30]. A potential way to enhance efficacy in such cancer therapies is to increase feedback through additional clinical signs during the accumulation and treatment phases. Concurrently, innovative medical devices are being developed to provide near-instantaneous pharmacokinetic feedback, [35], [36] suggesting the need for an elemental analysis technique that provides similarly rapid quantitative feedback of biodistribution. These analyses could assess when, and to what degree, the particles were accumulating in the tumor, or if they were being eliminated by the RES. The use of rapid elemental analysis coupled with real-time pharmacokinetic measurements could help predict the most appropriate time for animal or human ablation (e.g. photothermal) of the tumor. For animal studies, a faster technique can have a major impact for companies involved in nanomaterial quality control and product development. For human trials, the ability to measure, or predict, the accumulation of the nanoparticles in the target tissues could improve treatment outcomes for some of the approximately 52,000 anticipated deaths due to cancers targeted by this therapy each year in the United

States [9]. Biodistribution of gold nanorods is normally analyzed through inductively coupled plasma mass spectrometry (ICP-MS) or instrumental neutron activation analysis (INAA) [47]. ICP-MS requires elaborate and time-consuming sample preparation (up to 104 hours) [70]. INAA does not require a long sample digestion and preparation, but requires longer analysis [47]. Although both of these techniques are accurate, they take from days to weeks to get results, longer than a clinical treatment time of one day. If the data were available within the clinical treatment time, we hypothesize that some accuracy could be sacrificed compared to these standard methods.

Energy Dispersive X-Ray Fluorescence (EDXRF) is a technique used for bulk and ppm elemental analysis that is rapid, robust and requires little sample preparation time [71]. EDXRF has been previously used for quantitative *in vivo* and *ex vivo* analysis of gold in tissues like kidney and liver [72], [73]. Previous work with biological samples demonstrates the need for thin samples, so that matrix effects can be neglected [74]. Common EDXRF protocols require a long process of drying, crushing, and pressing samples into pellets [74], [75]. Based on guidance from the literature towards optimizing a rapid sample preparation, the key aspects of this protocol include: sample thickness, geometry, and homogeneity [74].

Chapter 4 outlines the procedure developed for a benchtop EDXRF elemental gold analysis of gold nanorods ($\approx 15 \times 45$ nm), an optically absorptive cylindrical nano-object used in nanomedicine. The protocol presented includes tissue digestion/homogenization in potassium hydroxide followed by desiccation in the sample cup before EDXRF analysis. Using subcutaneous mouse tumors, the elemental analysis was completed in less than 12 hours from the time of tissue collection.

CHAPTER 3

CALIBRATION AND DETERMINATION OF OPERATIONAL RANGE OF THE PULSE PHOTOMETER

This section discusses the experiments dealing with establishing the operating dynamic range of an optoelectronic device designed to measure the concentration of optically resonant nanoparticles *in vivo*. Gold nanoparticles (nanorods and nanoshells) are a class of optically resonant nanoparticles that are used for photo-thermal ablation (PTA) of tumors. PTA is a cancer treatment modality using preferential heating of tumor tissue to the point of irreversible cell damage by illumination with a light source. NIR extinguishing gold nanoparticles can be used in PTA to enhance absorption and localized heating in tissues where they collect. In the treatment of tumors, nanoparticles can be injected in the vasculature and extravagate at the tumor site. Once optimal nanoparticles collection is achieved, a laser emitting a wavelength corresponding to its resonant wavelength is used to irradiate the tumor. The absorption of this energy causes a localized significant increase in temperature, causing damage to the cells in the tumor but leaving tissues not containing NS unaffected. The development of a novel optoelectronic instrumentation was guided by the need to monitor the *in vivo* circulation of these nanoparticles.

The optoelectronic instrumentation is based on the pulse oximetry theory, which itself was based on pulse plethysmography. Pulse plethysmography is an optical technique that observes the changes in pulsatile tissue to measure the oxygen saturation level (sPO₂). Aoyagi discovered that if the signal from pulsating arterial blood was analyzed, the attenuating factors could be subtracted [63]. Since the pulse oximeter uses changes in the attenuation coefficient of blood to calculate the concentration of oxygen in pulsatile blood, the same principle was applied to calculate the concentration of optically resonant gold nanoparticles in the blood, since they too, change the attenuation of visible light in blood.

Once the instrumentation was complete and the experiments were performed using the pulse photometer, the data obtained from it was in terms of optical density, which is the measure of the attenuation of light in the medium. The readings were verified by conducting blood draws with each data point. The blood samples were analyzed using UV/Vis spectrometry, which revealed a linear correlation between the readings of the device and UV/Vis spectrometer. ($R^2 = 0.9839$, $p\text{-value} = 2.2 \times 10^{-16}$) [43]

However, the question of limits of operation of the pulse photometer still remained. Therefore, the following experiments were designed to determine the upper and lower dynamic of the pulse photometer.

3.1 Upper Dynamic Range Experiments

The experiment to determine the upper detectable limit of optical density values by the pulse photometer was performed. The experiment was set up in such a way that a naïve balb/C mouse was injected in three minute successions of a 20 μ L volumes, and a continuous pulse photometer reading was taken until the readings were inconsistent

(caused by the assumed saturation of the detector photodiode, where too little light is being passed through the tissue for the detector to detect).

3.2 Materials and Methods

3.2.1 Animal Experiments

All experiments were conducted using BALB/c female ($n = 3$). All animals were handled and cared for in accordance with the Louisiana Tech University and Nanospectra Biosciences, Inc. (NBI, Houston, TX) Institutional Animal Care and Use Committees.

3.2.2 Temperature Control

Prior to injection and for three and a half hours after injection the animal was kept under specific temperature control (35-39°C), to facilitate intravenous cannulation and to normalize the extravasation of the gold nanorods [33].

3.2.3 Dosage

For this experiment, the animals received 300 optical density gold nanoshells in steps of 25 μL approximately five minutes apart. Since the objective of the experiment was to establish the upper limit of detection of the pulse photometer, the total injection supplied about 100 μL of 300 OD solution of nanoshells (3-4 times the normal dose).

3.2.4 Anesthesia

Isoflurane inhalation (3% for induction and 2% for maintenance) anesthesia was used to immobilize the animal for injection and to assist with the collection of the first PPG reading. The flow rate was maintained at 1.5 L/min.

3.2.5 Injection

Nanoshell injections were administered via intravenous cannulation of the tail vein, using a 28 GA needle. The injections were given at a rate of 9-18 $\mu\text{L}/\text{minute}$ depending on dose volume and expected remaining time under anesthesia.

The data thus obtained was imported in MATLAB® and it was plotted in a weighed scale, using the 'loess' curve smoothing function (described in Appendix G).

The data before the application of the smoothing algorithm is shown in Figure 3-1.

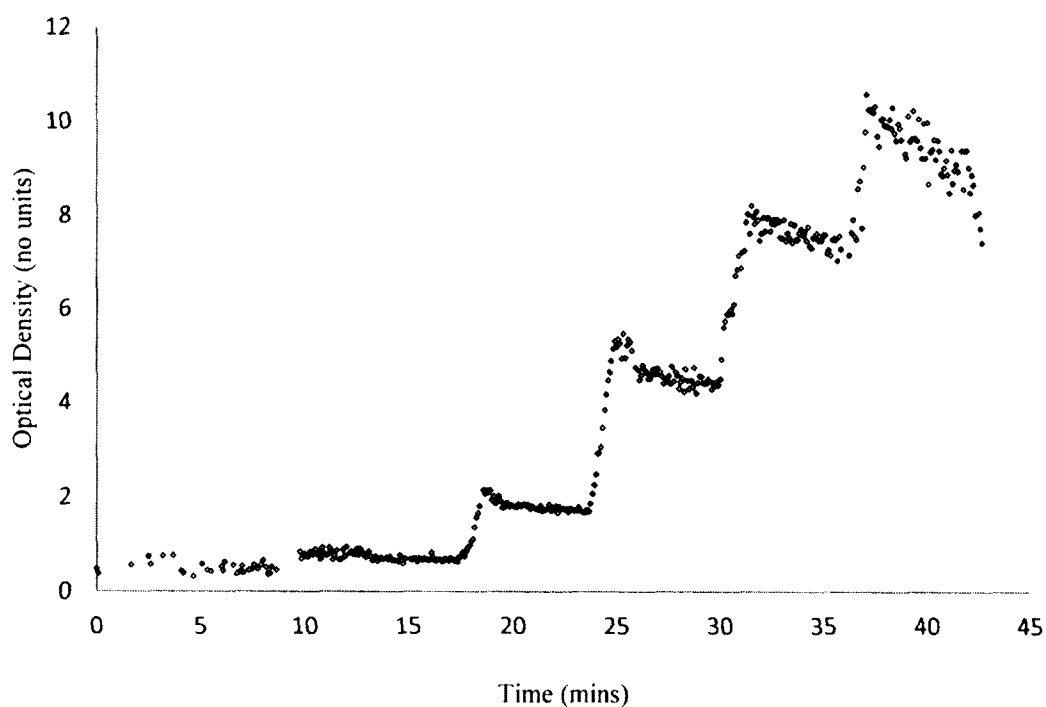


Figure 3-1: The bioavailability curve of a naive BALB/c mouse (first injection at around 18 mins, and an injection every five minutes. The graphed data represents the data with artifacts removed (using MATLAB code). The average of upper limit of detection of the device was found to be 7.94 optical density ($n = 3$).

After that the 'trapz' function in MATLAB was used to calculate the area under the curve of the original data and that was compared to the area under the curve of the smoothed data.

3.2.6 Example Calculation

The following is the theory behind the calculations that were used to compute the signal to noise ratio used in calculating the upper limit of detection. Let's assume that x is a data point from the original curve at time t and x' is the data point from the smooth curve at the same time t .

Now, normalized Area under the curve (NAUC) for original data point from the discrete data series is defined by the following equation:

$$\int_0^t x^2 dt, \quad \text{Eq. 3-1}$$

Where normalized area under the curve (NAUC) for the smooth data obtained from the smoothing function is defined by the following equation:

$$\int_0^t (x')^2 dt, \quad \text{Eq. 3-2}$$

and the difference between the two is caused by the noise in the signal.

So, the signal to noise ratio calculated from the NAUC of the noise and NAUC of the smoothed signal by using the formula:

$$\text{SNR} = 20 \log \left(\frac{A_1}{A_0} \right), \quad \text{Eq. 3-3}$$

where A_1 is the NAUC of the noise and A_0 is the NAUC of the original data.

To better analyze the appropriate limit of the pulse photometer, the whole data was divided into segments for each injection and the SNR of those groups was compared.

The highest OD levels at which the pulse photometer data maintained a SNR of 20 while fulfilling all the other requirements of good data (ie. 10 mV AC voltage peak-to-peak, the standard deviation below 0.03) is considered the upper limit of detection of pulse photometer.

3.2.7 Discussion

The upper limit of detection of the pulse photometer at 805 nm was determined to be 7.94 OD. Cope *et al.* established that an optical density of 10 translates to 8-9 cm of brain tissue [76]. Near infra-red light has been used to perform transmission mode spectrometry to monitor cerebral oxygenation of a larger volume of tissue (intact head of a cat, preterm infants) in the past [76, 77]. Although time resolved spectroscopy is required to determine the exact path length and the differential path length factor (DPF) of photons in the tissue, this ability to detect approximately eight optical density in the near infra range points to the fact that this prototype can be used for studies in larger animals. This is confirmed by the presence of pulsatile signals received by the detector through the tissue at those high concentrations.

However, it is important to note that an optical density of eight has an implicit unit of cm^{-1} associated with it. Since these experiments are performed in a mouse tail, the trans illumination distance is not the standardized 1 cm path length. Moreover, the signal analyzed by the pulse photometer only accounts for the AC portion of the signal, which is the pulsatile arterial blood (as shown in Figure 1-1). This means that the optical density of eight as read by the pulse photometer describes the absorption equivalent to 1 cm cuvette filled with the arterial blood.

In addition, the specifications of the parts used in the prototype can be a helpful guide in a rough estimation of the upper limit of detection. The noise equivalent power and the output irradiance of the LED used can be used to roughly estimate the upper limit of detection for any given detector/LED combination for a particular wavelength. This would be helpful in quick estimation of whether this prototype will be suitable for detection of other chemicals with known absorption peaks. An example calculation is shown in Appendix B.

3.3 Lower Limit of Detection

The lower detectable limit of the pulse photometer was established using a statistical technique. Baseline data was collected from 18 BALB/c mice and compiled to form a probability distribution around the baseline value.

BALB/c mice were repeatedly injected with very low dosage of gold nanoshells, and the data was compiled into an input matrix. Then, MATLAB was used to find the nearest probability distribution within the data that was outside the 95.3% confidence interval of the baseline distribution. The MATLAB algorithm was designed to maximize the Bhattacharya Distance Measure (BDM) [75], while minimizing the distance between the two means. The computation yielded a mean of 0.57 OD with a normal distribution around the mean, which was classified as the lower range of detection.

CHAPTER 4

DEVELOPMENT OF AN ENERGY DISPERSIVE X-RAY FLUORESCENCE (EDXRF) TECHNIQUE FOR ELEMENTAL ANALYSIS OF GOLD NANORODS

4.1 Introduction and Specifications

This chapter outlines the procedure developed for a benchtop EDXRF elemental gold analysis of gold nanorods ($\approx 15 \times 45$ nm), an optically absorptive cylindrical nano-object used in nanomedicine. The protocol presented in this report includes tissue digestion/homogenization in potassium hydroxide followed by desiccation in the sample cup before EDXRF analysis. Using subcutaneous mouse tumors, the elemental analysis was completed in less than 12 hours from the time of tissue collection.

This device uses x-ray excitation of a sample to characterize the elemental composition. The specifications for the development of this elemental analysis protocol are:

- Complete sample analysis 12 hours after collection.
- Minimal sample preparation.

4.2 Materials and Methods

4.2.1 Animal Experiments

All experiments were conducted using BALB/c female mice inoculated with CT26.WT tumors on the subcutaneous flank. The accumulation experiment was performed on animals with a target tumor size of greater than 5 mm in length and width. All animals were handled and cared for in accordance with the Louisiana Tech University and Nanospectra Biosciences, Inc. (NBI, Houston, TX) Institutional Animal Care and Use Committees.

4.2.2 Temperature Control

Prior to injection and for three and a half hours after injection the animal was kept under specific temperature control (35-39°C) to facilitate intravenous cannulation and to normalize the extravasation of the gold nanorods [37].

4.2.3 Dose Groups

For this experiment, two dose groups were used. Both of the groups were based on the multiples of standard dose administered by NBI. The first group received 4.5 $\mu\text{L/g}$ subject weight of 100 optical density gold nanorods (Dose group A) and the second group received 9 $\mu\text{L/g}$ of 100 optical density gold nanorods (Dose group B).

4.2.4 Anesthesia

For this experiment we used 2,2,2-Tribromoethanol (Sigma-Aldrich T48402) mixed with 2-Methyl-2-Butanol (Alfa Aesar A18304), more commonly referred to as Avertin, administered via intraperitoneal (IP) injection. The working solution of Avertin was administered at 30 μL of solution per gram body weight. Booster injections (0.5x) were delivered as necessary.

4.2.5 Injection

Nanorod injections were administered via intravenous cannulation of the tail vein, using a 28 GA needle. The injections were given at a rate of 9-18 $\mu\text{L}/\text{minute}$ depending on dose volume and expected remaining time under anesthesia.

4.2.6 End of Experiment and Organ Collection

At the end of the experiment, defined as when the blood plasma concentration of circulating nanorods reached one optical density, a 20 μL IP injection of a Ketamine/Xylazine mix was administered as heavy anesthesia. A dissection was started from the base of the abdominal cavity to sacrifice the animal by exsanguination via cardiac puncture using a 22 GA needle/syringe prefilled with 100 μL of heparin. After animal sacrifice, the following tissues were collected for further study: heart, lungs, liver, kidneys, spleen, and tumor.

4.2.7 EDXRF Sample Preparation

A wet weight of the tissue was obtained at the time of extraction. A 20% w/w KOH solution was added to the tissue based on the sample weight (3 $\mu\text{L}/\text{mg}$). The tissue and base solution were placed in a shaker or rocker until the tissue liquefied, approximately four to six hours. Aliquots of 35 μL (selected to cover our area of detection: 15 mm x 12 mm, containing approximately 0.04 g of tumor tissue) were placed in EDXRF sample cups on a Prolene® thin film support (Chemplex Industries Inc., 4 μm thick, Cat. # 3017). The tissue solution was then dried in the sample cup for two hours in a vacuum oven at 30°C under 15 in Hg vacuum to reduce the movement of the sample. The samples were analyzed in an ARL Quant'X (Thermo Scientific) EDXRF spectrometer (4-50 KV X-ray generator, Beryllium window, with 80° geometry between

x-ray tube, sample, and detector) using a thick Palladium filter (Mid-Zc range) for two minutes (50% dead time). Three replicates were prepared from most tissue samples. Each sample cup was scanned ten times which produced up to 30 spectra for each tumor. The spinner was turned on during each scan to minimize the error from the sample placement in the cup.

4.2.8 Data Analysis

Each spectrum was analyzed to compute the calibration curve shown in for a range of gold concentrations in the tissue. From the spectra, as shown in Figure 4-1, two regions of interests (ROI) were chosen. From the spectra, as shown in Figure 4-1, two regions of interests (ROI) were chosen. The ROI 1 represents the region for the $L_{\alpha 1}$ peaks for gold (9.712 KeV). However, that region lies very close to the $K_{\beta 1}$ peak for zinc (9.570 KeV) as shown in Figure 4-1.

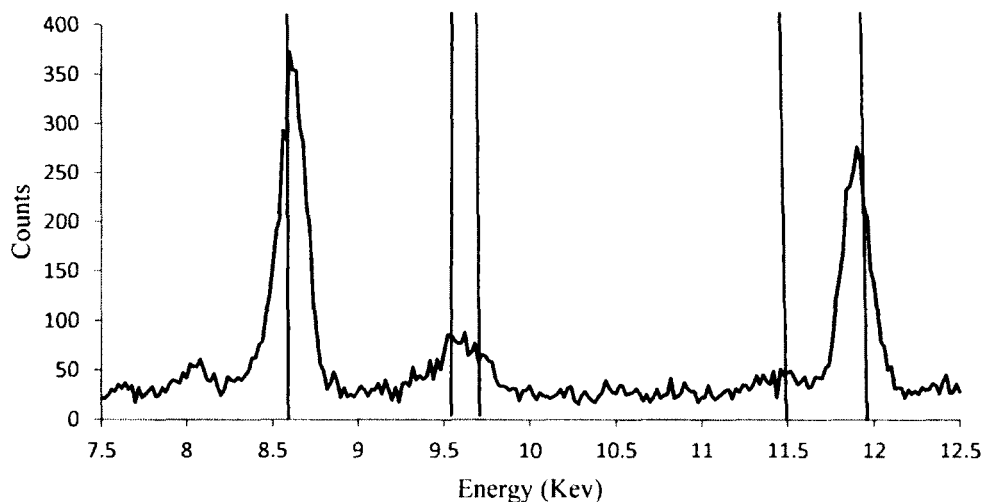


Figure 4-1: A raw spectrum of a sample from the calibration set (PPM value = 21.73). Vertical lines from left to right: Zn K_{α}^1 line (8.631 KeV), Zn K_{β}^1 line (9.572 KeV), Au L_{α}^1 line (9.711 KeV), Au L_{β}^1 line (11.439 KeV), Br K_{α}^1 line (11.907 KeV). These lines contribute to counts at each given energy.

The zinc found in the sample is attributed to zinc/aluminum alloy used in the sample chamber lid [17-18]. The data (in counts) was normalized in terms of tube current (counts/mA), and the normalized background was subtracted from all the data points.

A standard value of counts for zinc (obtained from the repeated runs of 0 ppm) sample was then subtracted from all the samples. After the subtraction, the values were normalized to obtain the peak intensity values (counts per second/mA). The peak intensity values of the calibration set were plotted against the actual concentration (of standard gold solution in the tissue) to produce a calibration curve.

4.3 Results

The doped tumor samples were plotted and fit with a linear trend line (where *PPM* is the calculated sample concentration in parts per million and *PI* is the peak intensity in counts per second per milliamp) for use as a calibration curve for this analysis.

$$PI = 0.0729*PPM + 0.0174. \quad \text{Eq. 4-1}$$

The calibration curve showed a strong linear correlation ($R^2 = 0.98$) between the concentrations of gold in doped samples (the samples were doped at regular concentration in the 0-60 ppm range) with the calculated peak intensity values after the manual subtraction. Therefore, this method was deemed suitable for assessment of gold concentration in tumors in the specified concentration range, which was also the clinically relevant concentration range for accumulation of gold nanorods after intravenous delivery.

The calibration curve with the doped samples, along with the tumor samples analyzed for gold concentration are shown in Figure 4-2.

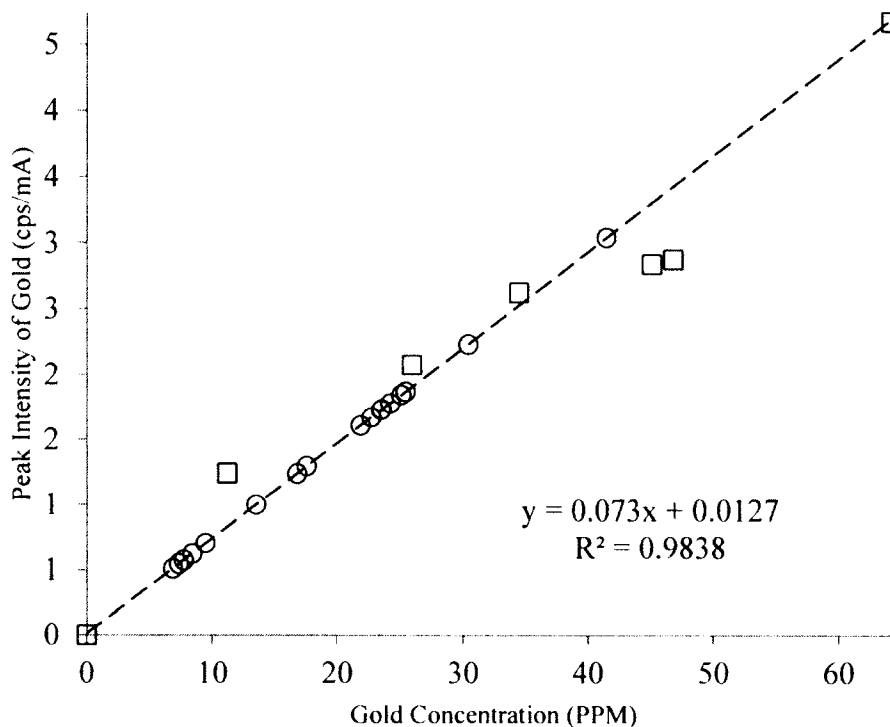


Figure 4-2: EDXRF calibration. This graph demonstrates the raw calibration points (□), calibration curve (dashed line), and individual tumors (○).

This method has a detection limit (3σ) of 1.4 ppm and a sensitivity of 0.07 cps/mA/PPM.

4.4 Discussion

The EDXRF protocol for gold in the tissue was designed with the following aims: quick and easy sample preparation, thin samples, and quantitative results. A 20% KOH solution was chosen, after experimentation, to minimize the time for liquefaction of the tissue. Thin sample geometry was implemented because the thick samples were impractical given the amount of tissue available, and to avoid intermediate sample thickness. An aliquot of 35 μL of tissue was selected to create a thin sample area entirely in the detection geometry of the detector. Quantitative results were obtained using the

same tissue dilutions and same sample scan time; Using doped tissue samples for calibration, we were able to provide a linear relationship between counts and tissue concentration. The calibration curve was used to obtain the values of the concentrations (in ppm) for tumor samples (dose group A: $n = 8$, mean = 10.7 PPM, STDEV = ± 5.8 PPM, and dose group B: $n = 9$, mean = 25.3, STDEV = ± 6.9 PPM). An analysis of the peak intensity (CPS/mA) versus the gold concentration (PPM) using different tissue types showed an R^2 correlation of greater than or equal to 0.93, despite having different slopes (0.0733-0.0856 cps/mA/PPM).

It was hypothesized that the small variations observed in the reported slopes were attributable to variations in tissue densities given that the regressions were similar when multiple preparations of the same tissue type were analyzed. The calculated concentration values for gold in the tumors were similar to the work published by *Huang et al.* which used industry standard methods [78]. Commercial laboratories that employ INAA or ICP-MS to analyze gold concentration report a detection limit in the low PPB range. This EDXRF analysis method demonstrates a detection limit of 1.4 ppm (3σ) and a sensitivity of 0.07126 cps/mA/PPM. This higher detection limit is acceptable due to the clinical requirements of rapid results in the PPM range.

The majority of the problems encountered were due to the presence of other elements that spectrally overlapped with one or more of the peaks of interest, as seen in previous work [79]. The zinc $K\beta_1$ peak (9.570 Kev) overlaps the $L\alpha_1$ peak for gold (9.712 Kev). Other peaks were explored for potential use; a second peak, the $L\beta$ peak (11.204-11.914 Kev), for gold overlapped the $K\alpha_1$ bromine peak (11.906 Kev). The bromine peak was attributed to the use of avertin (2-2-2-tribromoethanol) as the anesthesia for this

experiment. The bromine peak was only observed in the tissue samples where avertin was used as the anesthesia. For this reason, the use of anesthesia may influence the elemental analysis of tissues and should be considered among the criteria for selecting anesthesia in the experimental design.

4.5 Review of Specifications

A novel EDXRF protocol for rapid analysis of gold in the tissue, with a sensitivity of 0.07126 cps/mA/PPM and the lower detection limit of 1.3 ppm was developed. The project met the original specifications demonstrated in Table 4-1. The data from this project are included in a publication titled “Feasibility of energy dispersive x-ray fluorescence determination of gold in soft tissue for clinical applications” [80].

Table 4-1: Summary of Chapter 4 specifications.

Specification	
<i>Elemental Analysis</i> Develop a method to rapidly quantify the accumulation of gold nanoparticle in the tumor	Develop a protocol for elemental analysis of gold in tumor tissue using EDXRF, sensitive in the 0-50 ppm range, rapid enough to inform a clinical decision (24-48 hours)

After the development of the elemental analysis protocol, it was integrated into a set of pre-clinical experiments, with the goal of development of a population pharmacokinetic model for the gold nanorods. The data from the elemental analysis would inform the efficacy of the treatment (i.e. the final accumulation of the nanoparticles in the tumor) discussed in Chapter 5.

CHAPTER 5

USE OF REAL-TIME PHARMACOKINETICS TO PREDICT TUMOR UPTAKE OF GOLD NANORODS

5.1 Introduction and Specifications

Nanoparticle directed photothermal ablation of tumors relies heavily on the accumulation of nanoparticles in the target tissues. An appropriate accumulation of particles is required for proper thermal confinement and ablation of the target tumor. Preclinical studies of tumor accumulation are being conducted in an effort to predict the accumulation of nanoparticles more accurately. This preclinical study in a murine model works to relate the area under the blood plasma concentration curve to uptake and retention in the tumor.

The optimization of treatment variables, such as therapeutic dosage, circulation half-life, and clearance rates, is critical in maximizing the efficacy of a treatment modality. Since the nanoparticles are cleared from circulation mostly by the RES, a correlation between tumor uptake and retention and bioavailability should exist.

The purpose of the tumored studies is to correlate standard pharmacokinetic metrics to the uptake and retention of gold nanorods in the tumors. This set of experiments is based a hypothesis that pharmacokinetic metrics will be a more accurate predictor of tumor uptake alone and on the specifications outlined as:

- Blood plasma concentrations will be collected in near real-time. After the collection, the data can be processed quickly (less than five minutes) after collection for inclusion in an actively changing one-compartment pharmacokinetic model.
- Population pharmacokinetic models will be constructed from the resulting data to help study the dynamics of the gold nanoparticle *in vivo* after intravenous delivery of the nanoparticles.
- Elemental analysis of the tumor tissue is completed in under 12 hours post experiment, with the outside time limit of 24 hours. Additional data processing time is limited to one hour after completion of instrumentation time.

This purpose was achieved by using the pulse photometer for the sensing of the plasma concentration of the nanoparticles in real-time. The ability to measure the achieved dose of nanoparticles in real-time allows us to confirm the delivery to the circulatory system in an experimental setting. This study relates the dosage of nanoparticles to the bioavailability curve, which enables a comparison of the AUC relative to a dosage value.

Linear one-compartment (ADVAN1, TRANS2), two-compartment (ADVAN3, TRANS4), and three-compartment (ADVAN11, TRANS4) pharmacokinetic models were evaluated using Bayesian analysis in NONMEM using the FOCE method. Inter-mouse variability random effects were included in the base model and assumed to be log-normally distributed. The clearance, in this model was modeled using an exponential model.

For example, the clearance for the i^{th} mouse can be written in the form of the equation:

$$CL_i = CL_{TV} \times e^{\eta_i^{CL}}, \quad \text{Eq. 5-1}$$

where CL_{TV} is the typical value of the clearance, and η_i^{CL} is an independent random variable normally distributed about zero that represents the proportional difference between the clearance in the i^{th} mouse and in the population. Additive, proportional, and combined residual error structures were tested.

In this study the continuous covariates of the mouse weight and the categorical covariate of the dose received were tested for potential effects on the pharmacokinetic model parameter estimates. The effect of both the continuous and categorical covariates on the typical value of a parameter was tested using additive, proportional, and exponential function forms.

For example, the additive effect of the dose group variable on the central compartment volume of distribution is:

$$V1_{TV} = \theta_1 + (\text{DOSE}_i - 1)\theta_2, \quad \text{Eq. 5-2}$$

where θ_1 and θ_2 are the estimated fixed effect parameters, DOSE_i is either one or two, which depends on whether the i^{th} mouse received a x1 dose or a x2 dose. For the final model, each covariate was tested individually using a forward addition followed by the backward elimination method. Model selection was based on the likelihood ratio test using the NONMEM objective function values (OFV). The OFV equals -2 times the log-likelihood (plus a constant) so the difference in OFV between models is approximately chi-squared distributed. A difference of 3.84 is significant at the $P = 0.05$ level for nested models with one degree of freedom.

The spectra from a calibration set (of known concentration values, created using tissue and gold standard solution) were extracted and the area under the curve of the gold L- α 1 peak (9.30 to 9.94 KeV) was calculated. From these values, the peak intensities were calculated and a calibration curve was established. The calibration curve shown in the figure shown has the peak intensity values (cps/mA) against known concentration (ppm) values.

5.2 Materials and Methods

All of the studies involve animal work conducted under protocol approved by the Louisiana Tech University and Nanospectra Biosciences, Inc. Institutional Animal Care and Use Committee (IACUC). All tumored studies involve naïve BALB/c females inoculated with 1.5×10^5 (50 ml injection volume) CT26.WT murine colon carcinoma tumor cells (ATCC) were obtained from NBI. When animals arrived at Louisiana Tech University Center for Biomedical Engineering and Rehabilitation sciences, the mice were kept in general animal housing until the tumors were at the proper experimental size, approximately 100 cubic centimeters.

5.2.1 Experimental Design

This experiment involved seventeen tumor inoculated BALB/c female mice. The mice were divided into two dose groups (Group A and Group B) to investigate the differences in pharmacokinetic metrics, blood plasma concentration and tumor uptake based on the injected dose.

5.2.1.1 Temperature control: The mouse was placed in an environment with an ambient temperature of 35⁰ C for 2.5 hours using a shaking incubator, with the shaker off (Labnet International, Inc. Edison, NJ. Model # 211DS). For at least one hour prior to

the injection, the ambient temperature was increased to 39^o Celsius. During injection and while the mice were under anesthesia the temperature was controlled using a heating pad (Physitemp Instruments, Inc. Clifton, NJ. Model # TCAT-2LV) and/or a space heater for ambient air temperature (Sunbeam Products, Boca Raton, FL. Model # SFH111). After the injection, the mouse was returned to the incubator kept in a 39^o C environment for the first three and a half hours of the accumulation phase. After the first 3.5 hours, the mouse was returned to a room temperature environment for the remainder of the experiment.

5.2.1.2 Anesthesia and injection: Intravenous cannulation was established after the mouse was under anesthesia. Avertin anesthesia was administered by intraperitoneal injection at the dosage of 25 $\mu\text{L}/\text{gm}$ body weight, while the air flow was maintained at a steady rate of one L/min with the help of an Oxygen concentrator (Invacare Model: IRC5LX02, Elyria, OH) during the experiment.

The nanorod injection was done by cannulating one of the lateral tail veins. Once an intravenous cannula has been established and flushed with saline, the pulse photometer was attached to the tail. The nanorods were injected at a rate of up to 18 micro-liters per minute using a syringe pump (New Era Pump Systems, Inc., Model # NE-1010). The ~ 100 OD nanorods were intravenously injected at the dosage of 4.5 $\mu\text{L}/\text{gm}$ (Group A) or nine $\mu\text{L}/\text{gm}$ (Group B) body weight at the rate of up to 18 $\mu\text{L}/\text{min}$.

5.2.1.3 Pulse photometer data collection: The pulse photometer was used to read the blood plasma concentration of the nanorods. The pulse photometer was attached to

the tail of the mouse in a warm environment, with the help of a Physitemp TCAT-2LV controller pad set to 38°C and carefully monitored space heaters.

Once temperature stabilization was achieved, the probe was placed on the awake animal's tail and the pulse photometer was allowed to collect data. Five-second averages of the values of R were computed to assess signal stability. Data collection was designed around an assumed six-hour circulation half-life of the nanorods, and with approximately five data points in the first half-life, two in the second and one in the third half-life. Data collected were as close to the following time points as possible: 5, 45, 120, 240, 360, 450, 720, and 1080 mins.

5.2.1.4 End of experiment: The mouse was sacrificed when the blood plasma concentration reached an optical density of one plus or minus ten percent. The mouse was sedated using a ketamine and xylazine mixture, and then sacrificed by exsanguination via cardiac puncture. Liver, kidneys, spleen, tumor, heart, and lungs were collected for EDXRF analysis.

5.2.1.5 Data analysis: The collected data was sorted by using a MATLAB code. A code was specifically written to extract the data points that meet all the criteria for data standards. Anticipating potential transient problems such as motion artifact or low perfusion, the signal was deemed acceptable only if the following criteria were met:

- AC magnitude was in the range of 10-100 mV peak-to-peak
- the standard deviation of R was less than 0.03
- the heart rate measured on all three channels (660, 805 and 940 nm) were within ten percent of each other.

The data extracted from the raw experimental data and the average optical density value was used to produce a blood plasma concentration curve, which was used to calculate the area under the curve (AUC), which was used as a pharmacokinetic parameter in the experiment. In addition, the peak value and the half-life of the clearance curve were calculated.

5.2.1.6 EDXRF tumor sample preparation: Using the wet weight of the tumor, obtained the day of extraction, 20% (m/m) KOH was added at the rate of three μL KOH/mg of the tumor. The tissue was left at room temperature in a low speed shaker until all tissue dissolved in the solution. From each tumor sample, 30 μL (of tissue + KOH solution) was pipetted in up to three unique EDXRF cups.

The solution was then dried down in a vacuum oven at 30°C under 15 in Hg vacuum until the tissue sample is completely dry. This process takes about four hours. The dried samples were run in the EDXRF machine (Quant'X, Thermo Electron Corporation) and run each sample with ten replicates. The machine calculated a ppm (parts per million) value for the concentration of gold in the tumor.

5.2.1.7 EDXRF tumor sample data analysis: The concentration calculations were manually verified by using the calibration set in the machine with the ppm values obtained by using the methods. The spectra from the calibration set of known concentration values) were extracted and the area under the curve of the gold L- α 1 peak (9.94 to 9.30 KeV) was extracted. From these values, the peak intensities were calculated and a calibration curve was established using a linear regression model.

The calibration curve compared the peak intensity values (cps/mA) against known concentration (ppm) values and was found to be linear within the range of zero to 60 ppm

gold in tissue, which was deemed to be an appropriate calibration range, based on values from literature.

5.3 Results

The results of the rapid elemental analysis are shown in Figure 5-1.

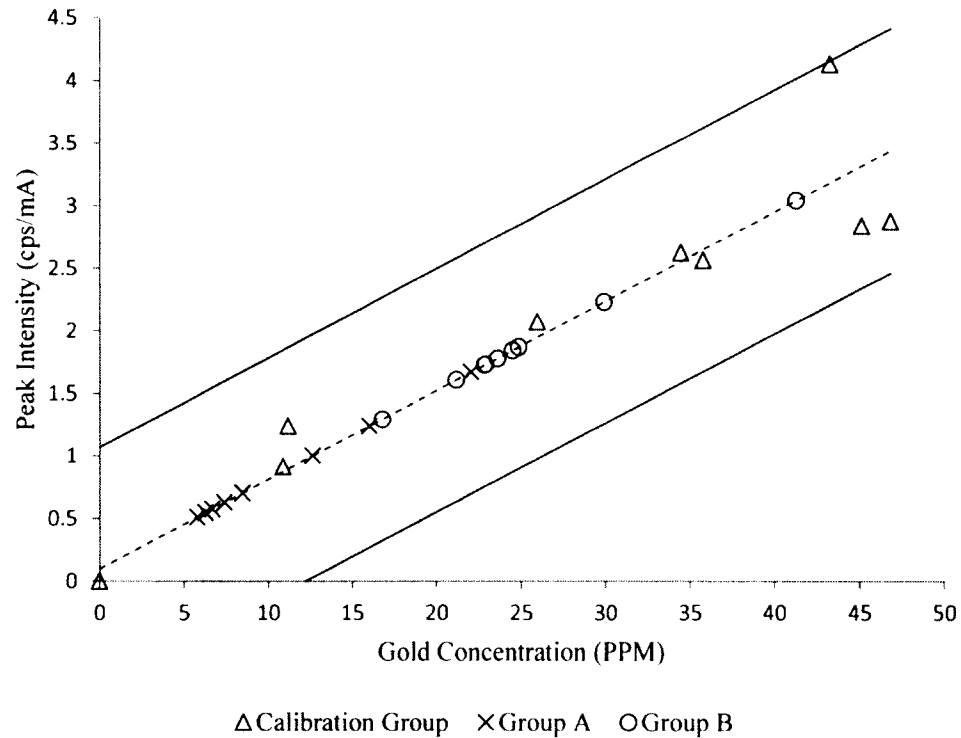


Figure 5-1: The graph of the peak intensity vs. concentration of gold in tissue for a sample of the Calibration data (Δ) from Figure 4-1, Experimental group A samples (\times , $n = 8$), and Experimental Group B Samples (\circ , $n = 9$). The linear correlation (dashed line) ($y = 0.07126x + 0.09984$, $R^2 = 0.93$) and 95% prediction interval are shown (solid lines).

The half-lives for all mice in the study were computed, and shows the large increase in average half-life from 271 minutes in group A to 408 minutes in group B. This increase in half-lives is demonstrated in detail for both experimental groups as shown in Table 5-1.

Table 5-1: Half lives for all mice in the study (n = 17). Dose group A got 9 μ L/gm, n = 8) and dose group B (4.5 μ L/gm, n = 9) with averages and standard deviations.

	Group A	Group B
Mouse 1	320	444
Mouse 2	357	313
Mouse 3	205	523
Mouse 4	267	373
Mouse 5	235	300
Mouse 6	281	356
Mouse 7	268	435
Mouse 8	236	478
Mouse 9		449
Average	271	408

A two-compartment model with proportional error best described the nanorod population pharmacokinetics. The typical values of the clearance, inter-compartment clearance, and peripheral compartment volume were 5.46 μ L/min, 5.82 μ L/min, and 246 μ L, respectively (See Table 5-2).

A covariate effect of nanorod dose on the central volume was found; the typical value of central volume was 1,870 μ L in the x1 dose group, and 3,100 μ L in the B dose group. The mouse's weight did not have a significant effect on any of the pharmacokinetic model parameters. The inter-mouse variability on the clearance,

central volume, and inter-compartment clearance were 22.5%, 18.8%, and 134.9%, respectively. The proportional residual error was 12.6% and the additive error was 0.00284 $\mu\text{g}/\mu\text{L}$. The details of the parameter estimation obtained using the two-compartmental model is shown in Table 5-2.

Table 5-2. Population pharmacokinetic parameter estimates from the final two-compartment model.

Parameter	Population estimate (%SE)	Inter-mouse variability (%SE)
Clearance ($\mu\text{L}/\text{min}$)	5.46 (5.5)	22.5 (47.6)
V1 (μL)		18.8 (38.2)
A dose group	1870 (7.7)	
B dose group	3100 (20.59)	
Q	5.82 (43.6)	134.9 (46.7)
V2 (μL)	246 (33)	---
Proportional error	12.6% (20.3)	
Additive Error ($\mu\text{g}/\mu\text{L}$)	0.00284(132.6)	

To investigate the effect of variables on the accumulation, a single variable correlation analysis was performed using the following variables:

AUMC (area under moment curve) ($R^2 = 0.54$), Volume of distribution ($R^2 = 0.08$), initial plasma concentration ($R^2 = 0.36$), Dose ($R^2 = 0.46$). Additional comparisons evaluated the effects of injected dose on the AUC ($R^2 = 0.69$), the effect

of dose on half-life ($R^2 = 0.65$), and the relationship between half-life and AUC ($R^2 = 0.64$)

The goodness of fit plots of the model to the nanorod concentration data showed no bias (see Figure 5-2 for typical example).

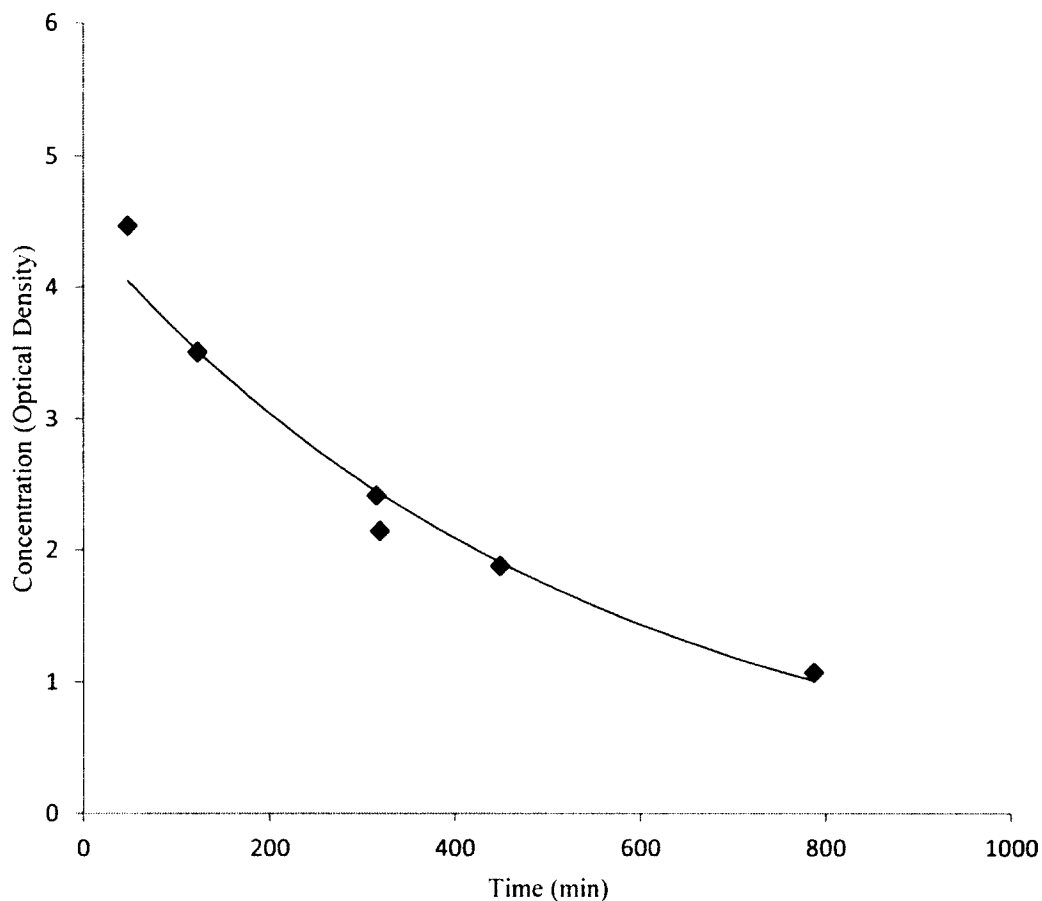


Figure 5-2: An example bio distribution curve built from the data taken by the pulse photometer.

In addition to the final accumulation in the tumors, various other clinical parameters, such as injected dose, peak plasma concentration were compared among the two experimental groups. The analysis demonstrated that the tumor weight is the only parameter where we are unable to reject the null hypothesis (the means of the

dose groups are equal) ($\alpha = 0.05$). The pertinent p-values and the clinical variables from the t-tests conducted between the two groups are shown in Table 5-3.

Table 5-3: P-values for comparison of pharmacokinetic and accumulation parameters between dose groups A and B.

	p-value
Concentration (PPM)	0.000129721
AUC (OD*min)	0.000120694
AUMC (OD*MIN2)	4.20157E-05
OD Adjusted Dose	6.24664E-07
injected dose (μL)	5.33305E-08
mean residence time	1.87732E-05
Elimination rate constant	0.00044814
half-life (min)	0.000579249
initial concentration from fit (OD)	0.026590645
Tumor Weight (g)	0.703795196

The data analysis shows an individual correlation between AUC and accumulation ($\mu\text{g}/\text{gm}$, or PPM) in the tumor and fitted to a linear regression model, which yielded a correlation of $R^2 = 0.56$.

5.4 Discussion and Review of Specifications

Animals which were included did not show a statistically significant increased prediction quality for AUC compared to the dose, suggesting that other yet unmeasured or uncontrolled factors play an important role in promoting uptake. In

the course of previous related studies, various groups have suggested the need for a set of best practices in terms of species selection for in vivo experimentation, particle size and coating, excipient [81]. In addition, several modeling studies have established that physiological variables related to the animal, such as animal blood pressure, core and peripheral temperature, and the effect of anesthesia need to be carefully controlled during experimentation, because these parameters seem to have an effect on peripheral circulation [15].

Models show that accumulation starts from bioavailability, and few things such as perfusion, blood pressure, tumor radius, porosity affect the accumulation. Good candidates would be any one or more of the following physiological variables: vascularity of the tumors, pore size of the vessels in the tumors, local blood pressure and necrotic radius of the tumor. The effect of tumor interstitial pressure on the accumulation of macromolecules has been investigated theoretically and experimentally in the literature [82, 83].

These modeling efforts have identified these factors and suggest that clinical protocols, short of direct control, would be wise to consider the effects of environment and drug interactions on these variables. While the ability to measure the real-time concentration of nanoparticles in the circulating blood brings us one step closer to pharmacokinetic modeling of nanoparticle interactions in the body, the inability to quantify variables such as vascularity of the tumors, and pore size of the vessels around the tumors prevents us from clearly establishing the relationship between the variables. AUC has been used as a pharmacokinetic metric to predict therapeutic outcome in the past in other drugs [6, 84].

However, those drugs function by the process of metabolism in vivo. The nanoparticles used in this study are passively accumulated in the tumor by taking the advantage of the leaky vasculature around the tumor tissue. Therefore, we posit that the physiological variables such as tumor perfusion, ambient temperature and porosity of the vessels around the tumor play a critical role in the accumulation of nanoparticles in the tumor. The majority of nanorods are believed to be removed from the blood by two pathways; opsonization and elimination by the phagocytes of the reticuloendothelial system (RES), and transient accumulation in other tissues, such as solid tumors [85].

The EDXRF protocol used in these experiments enabled us to analyze the accumulation data in the tumors in a clinically relevant time frame (24 hours). This decrease in sample analysis time made it possible to make adjustments to the temperature regulation protocol to improve the accumulation. A direct comparison of the accumulation achieved relative to previous reports was difficult without more factors for evaluation (e.g. prescribed dose vs. achieved dose, metrics of circulation, peripheral perfusion, etc.); however, it appears that this report, in terms of percent of dose injected, appeared higher in comparison to other studies we examined in the literature [78, 85].

For comparison, Nie et al. reported accumulations between 15 ppm and 75 ppm but the injected dose was not reported. Puvanakrishnan et al. reported between $0.118 \pm 0.027\%$ ID for nanoshells and $1.35 \pm 0.29\%$ ID for nanorods, with a dose of 7 $\mu\text{L/g}$ of 100 OD gold nanoshells and nanorods. AUC is a pharmacometric variable that has been previously used in studies to indicate the bioavailability of a substance

in the bloodstream [6]. This type of analysis could be a useful part of nanoparticle manufacturing, in both the prototype and pre-clinical stages, as well as in clinical trials. Nanomaterial production schemes are prone to batch-to-batch differences and irregularities, and clinical products can suffer from storage stability and contamination problems.

These issues along with inherent subject-to-subject variability and the need for clinical quality control suggest the utility of real-time monitoring of pharmacokinetic metrics. The design constraints of a nanoparticle-based delivery system designed to treat a solid tumor, which includes both the specifications of the nanoparticle in an excipient solution and the delivery and treatment protocol, should provide for optimization of accumulation in the tumor.

This optimization is both a function of bioavailability in the circulation as well as providing for circumstances for uptake at the target site. The continuing need for best practices in nanomedicine is confounded by the difficulty in relating these patient-specific factors to treatment efficacy.

A subset of this data in an in-progress publication titled “A Study of Gold Nanorod Bioavailability and Tumor Uptake in a Murine Model.” This data was also published in a conference proceedings paper titled “LQR Tracking of a Delay Differential Equation Model for the Study of Nanoparticle Dosing Strategies for Cancer Therapy”, in which control strategies to provide an optimal dose, maintain a target concentration in the plasma, and the most efficient dose profile, in terms of the amount of nanoparticles were discussed using a delay differential model, using the

data obtained from the experiments discussed in this chapter. [86]. A review of specifications is presented in Table 5-4.

Table 5-4: Review of specifications.

Specification	Status
Address the patient-to-patient variability (in terms of dosage, bioavailability, and uptake) in therapeutic nanoparticles.	Develop a population model for gold nanoparticles to establish a relationship between dose, bioavailability and accumulation in the tumor.
<u>Dose verification</u> Provide real-time assessment of the delivery of dose in gold nanoparticle therapy.	Use of novel multi-wavelength photoplethysmograph for direct dose verification and real-time <i>in vivo</i> sensing of circulating nanoparticles.

CHAPTER 6

RETICULOENDOTHELIAL SYSTEM BLOCKADE OF GOLD NANORODS IN A MURINE MODEL

6.1 Introduction

Current medical-grade particles are constructed from a variety of materials including lipids, polymers [20], and metals, [22] and are routinely delivered intravenously for passive or active accumulation in tumor tissue [21]. Accumulation via the vascular route increases as the nanoparticle circulation time increases and the nanoparticle circulation time increases by discouraging their removal by the reticuloendothelial system (RES). The high removal rate observed by the RES of charged and hydrophobic particles, [27] which is a requirement of a stable colloidal system, creates a need to mask the charge by adding a surface coating for nanoparticle therapies to be most effective. The Kupffer cells in the liver provide a major removal route of nanoparticles by the RES. Multiple agents have been evaluated to suppress the actions of the Kupffer cells.

Following the investigation outlined in Chapter 5, it was concluded that the AUC of the plasma concentration was one of the influential factors that affected the final accumulation of the gold nanoparticles in the tumor, ultimately affecting the efficacy

of the treatment. Building on this observation, it was hypothesized that the ability to modulate the AUC during the clearance phase of the injection could potentially influence the outcome (i.e. the final accumulation) in the tumor. In an effort to modulate the AUC during the clearance phase, λ -carrageenan was chosen as an adjuvant therapy to be administered in conjunction with the nanoparticle. λ -carrageenan was chosen because of its ability to cause temporary RES blockade. In addition to its RES suppression ability by the suppression of hepatic phagocytosis, it is also designated as Generally Recognized As Safe (GRAS) by the FDA [88] This chapter describes the preliminary experiments that established the feasibility of λ -carrageenan as an adjuvant therapy in a pre-clinical setting.

6.2 Materials and Methods

6.2.1 Overview

All animals were handled and cared for in accordance with the Louisiana Tech University Institutional Animal Care and Use Committee. Intravenous injections and blood plasma concentrations were monitored using the pulse photometer, and a bioavailability curve was created from that data. The purpose of this pilot study was to determine whether λ -carrageenan would be an effective RES blockade agent, and also determine a dosage plan of the adjuvant λ -carrageenan with the therapeutic particles.

Three BALB/c female mice were assigned one of three cases (A, B, or C). The dosage of the individual mouse in each case is described as follows:

- Case A was designated to be the initial control group. The mouse was injected with a regular dose of gold nanorods (4.5 μ L/gm body wt), and the bioavailability curve was recorded with the help of the pulse

photometer until complete clearance of the nanorods. After the clearance of the nanoparticles, the mouse was intravenously injected with 25 mg/kg of 10% λ -carrageenan solution, followed by another regular dose of gold nanorods.

- Case B was designed to investigate the efficacy of λ -carrageenan as a RES blocking agent after the introduction of nanorods in circulation. The mouse was intravenously injected with a regular dose of gold nanorods (4.5 μ L/gm body wt), and the bioavailability curve was recorded with the help of the pulse photometer for the first 30 minutes. After that, the mouse was intravenously injected with 25 mg/kg of 10% λ -carrageenan solution, and the clearance was measured, using the pulse photometer. The objective was to measure any changes in the clearance after the introduction of λ -carrageenan in the bloodstream.
- Case C was designed to investigate the efficacy of λ -carrageenan as a RES blocking agent before the introduction of nanorods in circulation. The mouse was intravenously injected with 25 mg/kg of 10% λ -carrageenan solution, followed by a regular dose of gold nanorods (4.5 μ L/gm body wt), and the bioavailability curve was recorded with the help of the pulse photometer.

The real-time concentration of the nanorods was recorded with the help of the novel pulse photometer, and used to create a bioavailability curve, from which the clearance and the half-life of the nanorods were determined.

6.2.1.1 Temperature control: The mouse was placed in an environment with an ambient temperature of thirty-five degrees Celsius for two and a half hours using a shaking incubator with the shaker off (Labnet International, Inc. Edison, NJ. Model # 211DS). For at least one hour prior to the injection, the ambient temperature was increased to thirty-nine degrees Celsius.

During injection and while the mice were under anesthesia, the temperature was controlled using a heating pad (Physitemp Instruments, Inc. Clifton, NJ. Model # TCAT-2LV) and/or a space heater for ambient air temperature (Sunbeam Products, Boca Raton, FL. Model # SFH111).

After the injection, the mouse was returned to the incubator kept in a 39^o C environment for the first three and a half hours of the accumulation phase. After the first three and a half hours, the mouse was returned to a room temperature environment for the remainder of the experiment.

6.2.1.2 Anesthesia and injection: Intravenous cannulation was established after the mouse was under anesthesia. Isoflurane anesthesia was used at the concentration of 3% for induction and 2% for maintenance steady at a rate of 1.5 L/min with the help of an Oxygen concentrator (Invacare Model: IRC5LX02, Elyria, OH) during the experiment.

The nanorod injection was done by cannulating one of the lateral tail veins. Once an intravenous cannula has been established and flushed with saline, the pulse photometer was attached to the tail. The nanorods were injected at a rate of up to 18 micro-liters per minute using a syringe pump (New Era Pump Systems Inc., Model#NE-1010). The ~100 OD nanorods were intravenously injected at the dosage of 4.5 μ L/gm.

The pulse photometer was used to monitor the condition of the mouse while under anesthesia.

6.2.1.3 Pulse photometer data collection: The pulse photometer was used to read the blood plasma concentration of the nanorods. The Pulse photometer was attached to the tail of the mouse in a warm environment, with the help of a Physitemp TCAT-2LV controller pad set to 38°C and carefully monitored space heaters.

Once temperature stabilization was achieved, the probe was placed on the awake animal's tail and the Pulse photometer was allowed to collect data. Five-second averages of the values of R were computed to assess signal stability.

6.2.1.4 Data analysis: The collected data was sorted by MATLAB code. A code was specifically written to extract the data points that meet all the criteria for data standards. Anticipating potential transient problems such as motion artifact or low perfusion, the signal was deemed acceptable only if the following criteria were met:

- AC magnitude was in the range of 10-100 mV peak-to-peak
- the standard deviation of R was less than 0.03
- The heart rate measured on all three channels (660, 805 and 940 nm) were within ten percent of each other.

The data extracted from the raw experimental data and the average optical density value was used to produce a blood plasma concentration curve (using a single decay exponential model). This curve was used to calculate the clearance, half-lives and area under the curve (AUC), which was used as pharmacokinetic parameters for this set of experiments.

6.3 Results

It was observed that λ -carrageenan was seen to extend the circulation half-life of the nanorods in all three cases. In the first case (Case A) as shown in Figure 6-1, the animal was injected with a normal dose of nanorods. The half-life was observed to be approximately 58 minutes. After the clearance of the nanorods, the animal was injected with λ -carrageenan before the nanorods, and blood concentration measurements were made. The new half-life measurement was found to be about 110 minutes, as shown in Figure 6-1.

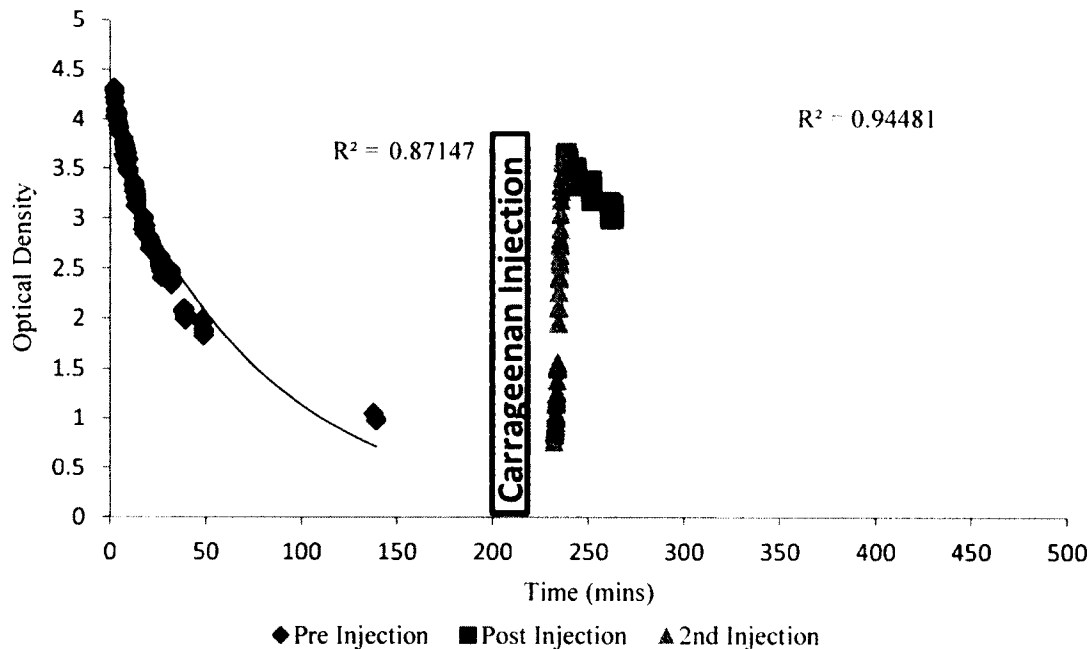


Figure 6-1: The effect of λ -carrageenan on circulation half-life of nanorods. The half-life for the first injection (without the λ -carrageenan injection) was 58.10 mins. The half-life for the second injection immediately following a λ -carrageenan injection was 110.55 mins.

Similar effects were observed in Case C where an animal was intravenously injected with λ -carrageenan directly followed by a normal dose of nanorods. The peak concentration was not affected, as shown in Figure 6-2, while the clearance rate

(according to a single decay exponential model) of the nanorods from circulation went down from $.00968 \text{ min}^{-1}$ to 0.00216 min^{-1} . This caused the half-life to be 321 minutes, as shown in Figure 6-2.

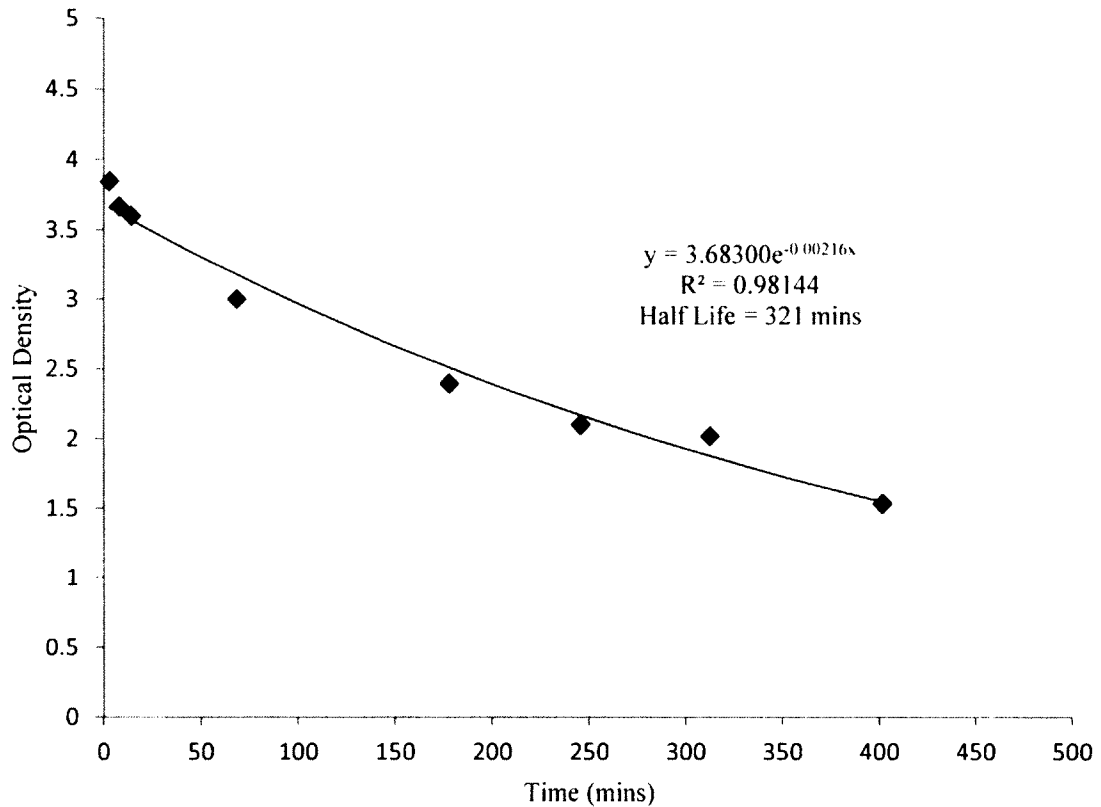


Figure 6-2: The circulation half-life of nanorods after a λ -carrageenan injection. It was observed that the peak concentration of the nanorods was not affected after the injection of λ -carrageenan, while the clearance slowed down, and thus circulation half-life went up.

The second case of the experiments (CASE B) was designed to investigate the effect of the λ -carrageenan injection after the introduction of nanorods in the circulating blood. For this experiment, a dose of λ -carrageenan was intravenously injected into an animal during the clearance phase, and the projected half-life of the nanorods before and after the injection were compared. It was observed that the clearance went down from

000868 min^{-1} to 0.00225 min^{-1} and the half-life increased from approximately 80 minutes to around 308 minutes (Figure 6-3).

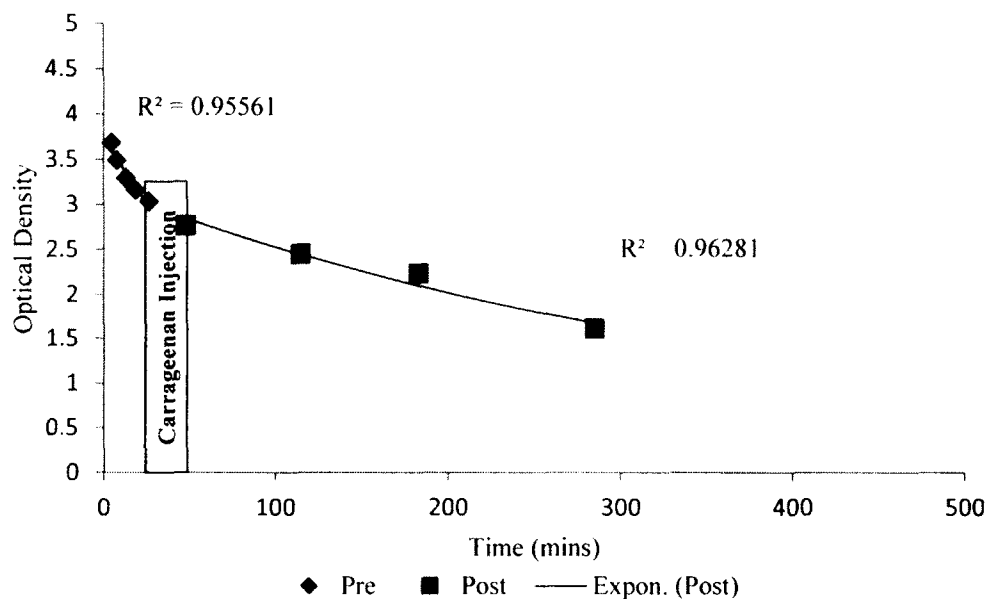


Figure 6-3: The elongation of circulation time of nanorods after the introduction of λ -carrageenan into the circulation.

6.4 Discussion

The purpose of this set of pilot experiments was to establish the feasibility to λ -carrageenan as an adjuvant therapy that could be used for RES blockade, ultimately increasing the AUC of the plasma concentration to help improve accumulation in the tumors. These preliminary experiments showed that λ -carrageenan could be used as a RES blockade agent to increase the circulation time of the nanorods in a murine model. The findings of this study demonstrate the utility of λ -carrageenan in increasing the circulation half-life and AUC of PEGylated gold nanorods. In addition, the use of λ -carrageenan after nanorods injections was able to increase AUC values. These findings are noteworthy for investigators who wish to achieve the longer circulation times without

particle modification. The data from these preliminary experiments was used to design a larger study on the effect of λ -carrageenan on circulation of nanoparticles. During the design of those experiments, it was theorized that the change in volume of distribution caused by the bolus injection of λ -carrageenan before nanorods could be affecting the clearance. Those concerns were addressed by adding a control group where equal volume of saline (as λ -carrageenan) was injected to the animal in the control group. This enabled the investigators to account for the change in AUC caused by the change in volume of distribution of the particles.

6.5 Review of Specifications

These preliminary experiments showed that λ -carrageenan could be used as an RES blockade agent to increase the circulation time of nanorods in a murine model. The findings of this study demonstrated the utility of λ -carrageenan in increasing the circulation half-life and AUC of PEGylated gold nanorods. The data from the subsequent experiments was presented (presentation title: “The Use of Real-Time Optical Feedback to Improve Outcomes”) at Photonics West BiOS on February 2, 2014, with an associated conference proceedings publication, [86] and is the data set for an in-progress publication titled “Suppression of the Reticuloendothelial System Using λ -Carrageenan to Prolong the Circulation of Gold Nanoparticles”. The specifications are described in Table 6-1.

Table 6-1: Review of specifications.

<p><u><i>RES modulation</i></u> Provide a means to modulate the AUC and clearance to increase exposure time of nanoparticles.</p>	<p>Develop a safe protocol for temporary RES blockade for the modulation of AUC, and eventually to increase treatment efficacy</p>
---	--

CHAPTER 7

USE OF PULSE PHOTOMETER FOR *IN VIVO* DETECTION OF QUININE

7.1 Introduction and Specifications

The novel multi-wavelength photoplethysmograph (PPG), discussed in previous chapters, was used to demonstrate the potential to enhance therapeutic treatment predictability as pharmacokinetic metrics are provided throughout the intravenous delivery phase of quinine in real-time. The drug currently under investigation is anti-malarial quinine which has an absorption peak at around ~350 nm. The algorithm was adapted to quantify the concentration of quinine in the pulsatile, circulating blood based on its extinction at three wavelengths (355, 660 and 940 nm). We show an example of the system collecting data representing the baseline, injection, and the clearance phases. An examination of the raw signal suggests that the system is well suited to sense the concentration of quinine in the therapeutic range (10 mg/kg).

The initial rationale for developing this type of instrument relates to the need for increased quality and reproducibility of nanoparticle-based therapies. The PPG quantifies the concentration using the Beer-Lambert law and the principles of pulse oximetry theory, focusing on the optical density of the pulsating medium measured in a

vascularized mass of tissue. This was implemented to find the concentration of gold nanoshells *in vivo* in the murine models across the therapeutically relevant concentration range [24]. The device uses off-the-shelf optoelectronic components in conjunction with a LabVIEW virtual instrument (VI) with an algorithm based on Beer-Lambert's Law in a multi-spectral method designed to elucidate the concentration (in optical density) of oxy- and deoxy-hemoglobin and the nanoparticles simultaneously in the blood. This device was implemented to measure the *in vivo* concentration of the particles that are absorbent between 600 – 940 nm, longer than the major absorptive bands of hemoglobin.

We speculated early in the development process that the opto-electronic system, as well as the intrinsic algorithms, should be versatile enough to sense traditional therapeutic agents not based on particle formulations. Potential compounds must contain optically absorptive bands in the water window between 200 and 900 nm, such as doxorubicin (absorption peak ~460 nm, fluorescent emission peak ~600 nm), quinine (absorption peak ~350 nm, fluorescent emission peak ~460 nm), and many of the agents used in photodynamic therapy.

A major concern dealt with the ubiquitous presence of hemoglobin, and how its absorptivity below 600 nm might confound the sensing of agents with absorption in that spectral region. We decided to examine quinine, focusing on the current clinical needs related to maintaining the dose within the therapeutic window and concerns of potential toxicity. Plasma quinine concentrations above 15 mg/l were associated with increased risks of permanent visual damage and of cardiac arrhythmias [88]. The selection was also a test of the versatility of the system, as the compound absorbs strongly around 350 nm,

corresponding with hemoglobin absorbance two-orders of magnitude greater than previously examined.

The award that funded this research presented aims that would demonstrate the potential benefits of integrating the PPG with established therapies. The aims are to improve treatment reproducibility as we precisely control and verify the delivered dose, as well as quantify the clearance properties of the drug in real-time allowing for better control of the dose within the therapeutic window. This report presents the feasibility test of the system to quantify the concentration of quinine, delivered intravenously at a therapeutically relevant dose.

7.2 Materials and Methods

7.2.1 Instrumentation

A combination of a multivibrator chip (CD4047BCN) configured in an astable free running mode producing pulses at a rate of 1.19 MHz and a 3-bit counter (MM74HC393N) are used to feed the signal into a 3-to-8 decoder (MM74HC138N). The decoder separates pulses among eight different channels, each generating pulses at the rate of approximately 150 pulses/sec with a duty cycle of approximately 15%. The pulses from the decoder are sent to buffers (LM324N) to supply power to our light sources.

The circuitry of the pulse photometer is designed to use up to eight channels of data collection. We used three data collection channels and one ambient light subtraction channel for our experiments. After the collection of the PPG of the mouse, the pulses are inverted, using an inverter (MM74HC04N), which controls sample and hold chips (LF398), one for each data channel and subtraction channel.

The signals from the sample-and-hold chips are then fed through a first order analog filter ($F_c \approx 28$ Hz) for smoothing and attenuation of the power line interference and then digitized with an NI DAQ card set to a sampling rate of 10 kHz.

The probe, a transmission-mode “clip”, looks similar to many commercially available veterinary pulse oximeters clips made for the tail, paw, or leg of a murine subject. Major components consist of a photodiode (Hamamatsu S1337-33BR) and LEDs (Roithner LaserTechnik UVTOP335-HL-TO39 and LED660N/940-04A). These LEDs are off the shelf opto-electronic components that contain wavelengths of 340 nm, 660 nm, and 940 nm. The 340 nm wavelength was chosen to match the maximum extinction peak of the quinine used.

7.2.2 Algorithm

The pulse photometer algorithm is implemented in a LabVIEW VI. The signal from the subtraction channel is first subtracted from each of the other channels to account for ambient light interference. A band-pass filter with user specified order and cutoff frequencies is utilized to extract the pulsatile portion of the PPG referred to as the AC signal.

The AC magnitude of the PPG is determined by the envelope of this signal. An averaging algorithm is used to extract the baseline or DC portion of the PPG. These values can be used to determine the extinction change due to pulsation at each wavelength using the Beer-Lambert Law as follows,

$$\Delta A_{\lambda} = \log \left(\frac{V_{DC}}{V_{DC} - V_{AC}} \right)_{\lambda} \sim \frac{V_{AC_{\lambda}}}{V_{DC_{\lambda}}}, \quad \text{Eq. 7-1}$$

where the ratio of ΔA at two wavelengths can be calculated, which eliminates the wavelength dependence of the measurements.

Further manipulation of the Beer-Lambert Law yields equations that are dependent only on the effective attenuation coefficients of reduced and oxygenated whole blood and the ratiometric pulsatile changes referred to as R_{λ_1/λ_2} where λ_1 and λ_2 are the interrogation wavelengths:

$$R_{355/940} = \frac{\frac{V_{AC355}}{V_{DC355}}}{\frac{V_{AC940}}{V_{DC940}}}, \quad \text{Eq. 7-2}$$

and the ratio for the second set of wavelengths is shown as

$$R_{660/940} = \frac{\frac{V_{AC660}}{V_{DC660}}}{\frac{V_{AC940}}{V_{DC940}}}. \quad \text{Eq. 7-3}$$

Summing the absorbances at the wavelengths, we get two equations as follows.

$$R_{355/940} = \frac{S(\mu_{HbO_2}^{355}) + (1-S)(\mu_{Hb}^{355}) + \mu_{quinine}^{355}}{S(\mu_{HbO_2}^{940}) + (1-S)(\mu_{Hb}^{940}) + \mu_{quinine}^{940}}, \quad \text{Eq. 7-4}$$

$$R_{660/940} = \frac{S(\mu_{HbO_2}^{660}) + (1-S)(\mu_{Hb}^{660}) + \mu_{quinine}^{660}}{S(\mu_{HbO_2}^{940}) + (1-S)(\mu_{Hb}^{940}) + \mu_{quinine}^{940}}. \quad \text{Eq. 7-5}$$

Simultaneous solving of these two equations yields estimates of both $\mu_{quinine}^{355}$ and S , where S is the oxygen saturation. Five second averages of the AC and DC magnitudes at each wavelength are computed and used to solve the system of equations to determine $\mu_{quinine}^{355}$ and S .

7.2.3 Animal Experiments

All animals were handled and cared for in accordance with the Louisiana Tech Institutional Animal Care and Use Committee. Three male albino mice (20-25 g), of undetermined genetic characteristics were used in this study.

Each mouse was placed under anesthesia using isoflurane vaporized at three percent concentration as set by the vaporizer (Dentry Biomedical) with 95% oxygen (Invacare 5) delivered at a flow rate of 1.5 L/min to a small plastic enclosure.

Once immobilization was achieved, the mouse was moved to a temperature controlled heating pad (Physitemp TCAT-2LV, controller) set to 38°C and the feedback thermometer was placed under the abdomen. Anesthesia was maintained by delivering isoflurane at a concentration of 20% of that used to induce immobilization via a snout cone.

The tail vein was then catheterized in order to deliver the quinine injection. Once the thermometer measured a temperature of around 39°C, the probe was placed on the mouse's tail and allowed to collect the photoplethysmograph data for a period of 30 seconds at a time.

Once signals at each wavelength met the typically used metrics of signal quality (AC amplitudes of 5 mVp-p with standard deviations of less than 0.08 over the five second average), an injection of 80 μ L quinine sulphate solution was given at the concentration of 3.23 μ g/mL in 0.9 % saline solution.

A dose of quinine, corresponding to approximately 12 μ g/gm was delivered intravenously. The pulse photometer was allowed to collect estimates of $\mu_{quinine}$ and S for five minutes after the injection phase, then removed briefly, and a final set of data meeting the previously described signal criteria was collected.

7.3 Results

The PPG recorded a pulsatile signal across the mouse tail, which demonstrates the transillumination of the tissue, with light hitting the photodiode. (around 3mm path length, as shown in Figure 7-1).

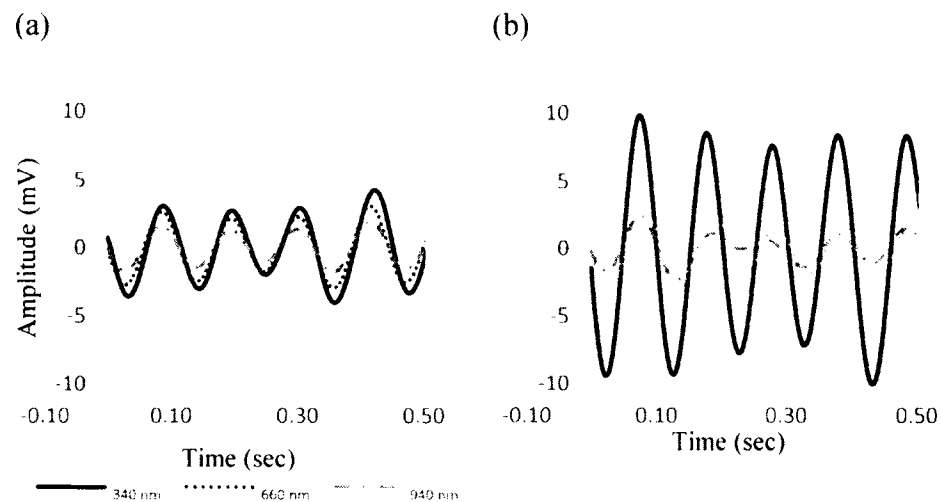


Figure 7-1: The pulsatile part of the photoplethysmogram signal (a) before injection (b) during and after injection. The ratiometric measurements of the three channels (with $V_{p-p} > 5mV$) were collected and used to calculate the *in vivo* concentration of quinine.

After the introduction of quinine in the blood stream, an increase was observed in the peak-to-peak amplitude of the AC signal at 340 nm, as demonstrated in Figure 7-1 as anticipated, compared to the red (660 nm) and infra-red light (940 nm). The magnitude of the AC portion of the signal corresponds to the respective extinction in the corresponding wavelengths, and should increase as the optical extinction at a specific wavelength increases. A common maintenance dosage of intravenous quinine solution is 10 mg/kg [9].

The PPG was run in continuous mode before, during, and after the intravenous delivery, and showed a peak concentration of ≈ 7 optical density (OD), as shown in Figure 7-2.

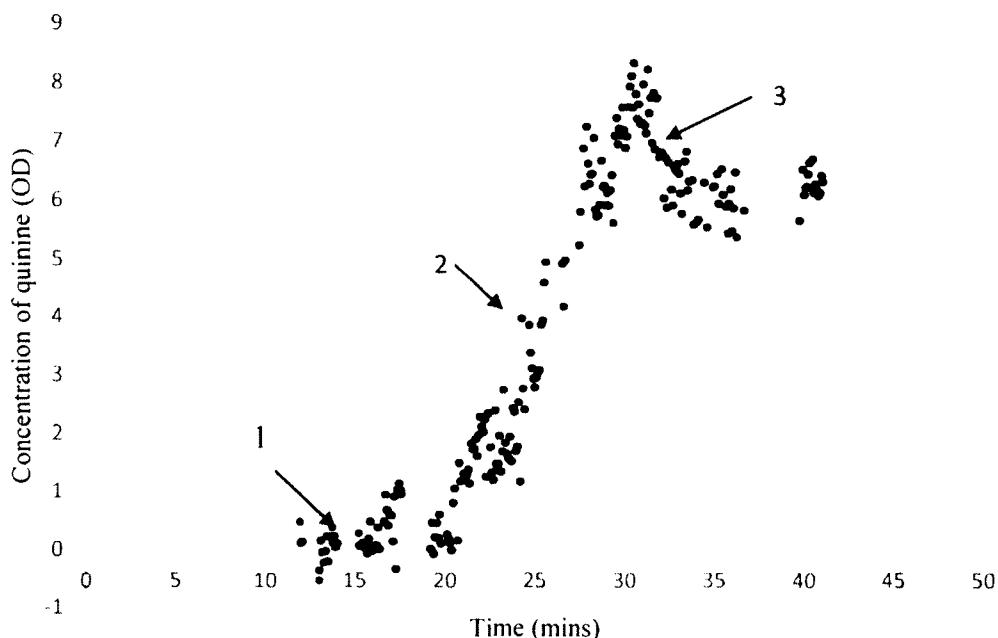


Figure 7-2: The real-time *in vivo* concentration of quinine in blood. The graph is divided into three parts: (1) Background data from pre-injection phase (2) The rising concentration during the injection, and (3) The decay phase after the end of the injection.

From the graph, it was observed that the concentration of quinine in the blood rises from the background (Part 1) during the injection phase (Part 2). The decay observed in the *in vivo* concentration starting at the end of the injection (Part 3) suggests that the quinine was starting to be metabolized or cleared as would be expected.

Previously, it was shown that the relationship between the concentration of an absorber in pulsatile blood and the optical density (concentration) readings measured by the device is linear [24].

An empirical calibration using blood draws and UV/Vis absorbance spectroscopy was performed, which was found to have a strong linear correlation ($R^2=0.96$) as shown in Figure 7-3.

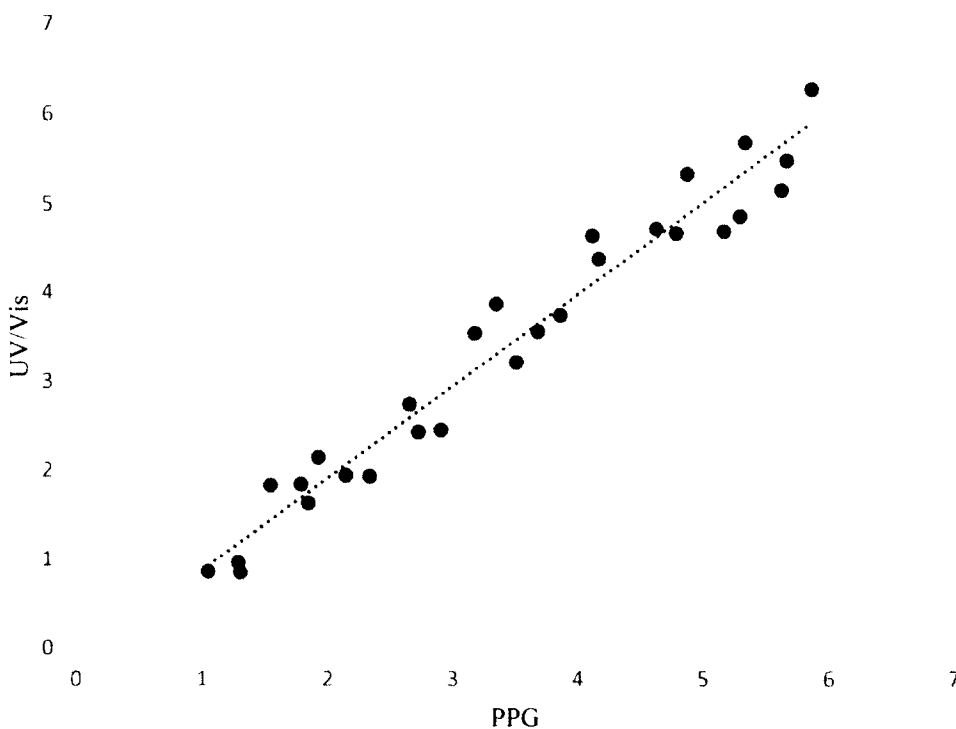


Figure 7-3: The comparison between the results of blood analysis (UV/Vis) and the PPG readings of intravenously injected quinine. The graph represent the PPG readings that were taken at different time points after the injection, plotted against the UV/Vis analysis of the blood draws at the same time points ($n = 3$ mice, 8-9 points from each mouse). Linear fit resulted in a straight line with the equation: $y = 1.032x - 0.1604$, $R^2=0.96$

The peak OD shown for the relatively “normal” dose suggests that this compound is well suited for the dynamic range of the device with nanoparticles, previously calculated to be 0.5 - 8 OD.

7.4 Discussion

This report suggests that the pulse photometer can be adapted for use towards the *in vivo* detection of circulating drugs with distinct absorption bands in the range of 200-

800 nm, corresponding to the low absorptivity of water in this specified region. This instrumentation could have clinical utility in support of drugs about which the knowledge of the initial or maintenance dose, circulation characteristics, and therapeutic window would be helpful or critical.

CHAPTER 8

USE OF PULSE PHOTOMETER FOR *IN VIVO* DETECTION OF AMPHOTERICIN B

8.1 Introduction and Specifications

Previous experiences related to the development of optically-absorptive nanoparticles for *in vivo* therapeutic applications led the team to appreciate the value of real-time pharmacokinetics [24, 89]. A real-time system allows for a precise dose to be achieved, and allows for an analysis of the clearance rate providing information related to the functioning of the physiological systems of the subject and the characteristics of the drugs or nanoparticles in use. Employed in a closely related inbred mouse group, real time pharmacokinetics can lend credibility to other metrics demonstrating the therapeutic agent has been manufactured according to specifications and functions *in vivo* as expected.

This chapter describes our initial investigation of the feasibility of our prototype towards amphotericin b (ampB), an anti-fungal agent. Given the significant mortality and morbidity of invasive fungal infections, and considering the significant challenges ampB poses in regards to its own toxicity, we present here a demonstration of real-time pharmacokinetics to medical practitioners who are faced with the challenges of high doses and/or long-term use.

The Center for Disease Control (CDC) reports candidiasis as the fourth leading cause of hospital-acquired infections in the United States [90]; however, for children and neonates, it is the third most frequent etiology of hospital-acquired infections in the United States and in Europe [91]. This significantly influences the high mortality rate among premature infants (~ 30% for those born weighing less than 1000 grams) [92]. AmpB is also widely indicated in oncology, immunology, and hematology, where hematopoietic stem-cell transplants are routinely utilized. Associated toxicity and therapeutic levels have been investigated for Amphotericin B used in prophylaxis for the highly immunosuppressed patients population undergoing hematopoietic stem cell transplants [93]. Amphotericin B is also applied to visceral *leishmaniasis*, which is fatal if untreated, affecting nearly half a million individuals annually [5].

While population-based half-life or peak levels provide for dosing recommendations and frequencies for a given pharmacological agent, no one individual with a given disease can be expected to process pharmacologic agents in an identical manner, lending many of the pharmacologic treatment decisions to a best estimate. The method presented here using an animal model suggests a tool or methodology to study pharmacological agents with significant toxicity while optimizing dose related efficacy, metabolism and clearance, and other relevant pharmacokinetic concerns. The PPG system utilized quantifies the concentration of the agent under observation using the Beer-Lambert Law and the principles of pulse oximetry theory, focusing on the optical density of the pulsating medium measured in a vascularized mass of tissue. The device uses off-the-shelf optoelectronic components in conjunction with a LabVIEW virtual instrument (VI) with an algorithm based on Beer-Lambert's Law in a multi-spectral method

designed to elucidate the concentration (in optical density) of oxy- and deoxy-hemoglobin and the nanoparticles simultaneously in the blood. This device was initially demonstrated to measure the optical density of the nanoparticles that are absorbent between 600 – 940 nm, in the range of wavelengths longer than the major absorptive bands of the hemoglobin.

We speculated early in the development process that the opto-electronic system, as well as the built-in algorithms, should be versatile enough to sense traditional therapeutic agents not based on particle formulations. Potential compounds must contain optically absorptive bands in the water window between 200 and 900 nm, such as doxorubicin (absorption peak ~460 nm, fluorescent emission peak ~600 nm), amphotericin b (absorption peak ~355 nm, fluorescent emission peak ~460 nm), and many of the agents used in photodynamic therapy.

A major concern dealt with the ubiquitous influence of hemoglobin upon the pulse-derived signal, and how its absorptivity below 600 nm might confound the sensing of agents with absorption in that spectral region.

The award that funded this research proposed to demonstrate the potential benefits of integrating the PPG with established therapies. The major aim, as presented here, demonstrates an optical sensing system that can provide improvements in treatment reproducibility via delivery control and allow for control of the circulating dose within the pharmacological therapeutic window. This report presents the feasibility test of the system to quantify the circulating concentration of amphotericin B, in the liposome-based Abelcet® formulation, delivered intravenously in a murine model at a therapeutically relevant dose.

8.2 Materials and Methods

8.2.1 Instrumentation

A combination of a multivibrator chip (CD4047BCN) configured in astable free running mode producing pulses at a rate of 1.19 MHz and a 3-bit counter (MM74HC393N) are used to feed the signal into a 3-to-8 decoder (MM74HC138N). The decoder separates pulses amongst eight different channels, each generating pulses at the rate of approximately 150 pulses/sec with a duty cycle of approximately 15%. The pulses from the decoder are sent to buffers (LM324N) to supply power to our light sources.

The circuitry of the pulse photometer is designed to use up to eight channels of data collection. We used three data collection channels and one ambient light subtraction channel for our experiments. After the collection of the PPG of the mouse, the pulses are inverted, using an inverter (MM74HC04N), which controls the sample and hold chips (LF 398), one for each data channel and subtraction channel.

The signals from the sample-and-hold chips are then fed through a first order analog filter ($F_c \approx 28$ Hz) for smoothing and attenuation of power line interference and then digitized with an NI DAQ card set to a sampling rate of 10 kHz. The probe looks similar to many commercially available veterinary pulse oximeters clips made for the tail, paw, or leg of a murine subject.

Major components consist of a photodiode (Hamamatsu S1337-33BR) and LEDs (Roithner LaserTechnik UVTOP335-HL-TO39 and LED660N/940-04A). These LED's are off the shelf opto-electronic components that contain wavelengths of 355 nm, 660 nm, and 940 nm. The 355 nm wavelength was chosen to match the maximum extinction peak of the amphotericin b used.

8.2.2 Algorithm

The pulse photometer algorithm is implemented in a LabVIEW VI, where signal from the subtraction channel is first subtracted from each of the other channels to account for ambient light interference. A band-pass filter (fourth order Butterworth filter) with cutoff frequencies at 4 Hz and 10 Hz is used to extract the pulsatile portion of the PPG referred to as the AC signal from the three channels. The AC magnitude of the PPG is determined by the envelope of this signal. An averaging algorithm is used to extract the baseline or DC portion of the PPG. These values can be used to determine the extinction change due to pulsation at each wavelength using the Beer-Lambert Law.

$$\Delta A_{\lambda} = \log \left(\frac{V_{DC}}{V_{DC} - V_{AC}} \right)_{\lambda} \sim \frac{V_{AC_{\lambda}}}{V_{DC_{\lambda}}}, \quad \text{Eq. 8-1}$$

The ratio of ΔA at two wavelengths can be calculated which eliminates the wavelength dependence of the measurements. Further manipulation of the Beer-Lambert law yields equations that are dependent only on the effective attenuation coefficients of reduced and oxygenated whole blood and the ratiometric pulsatile changes referred to as R_{λ_1/λ_2} where λ_1 and λ_2 are the interrogation wavelengths:

$$R_{355/940} = \frac{\frac{V_{355}}{V_{DC_{355}}}}{\frac{V_{AC_{940}}}{V_{DC_{940}}}}, \quad \text{Eq. 8-2}$$

and the ratio for the second set of wavelengths is

$$R_{660/940} = \frac{\frac{V_{AC_{660}}}{V_{DC_{660}}}}{\frac{V_{AC_{940}}}{V_{DC_{940}}}}. \quad \text{Eq. 8-3}$$

Combining the absorbance from the two channels in ratio metric form yields two simultaneous equations (Equation 8-1 and Equation 8-2), which can be solved by a linear

algebra to calculate the values of the two unknowns, and the ratios are calculated from the data collected from the photodiode (sensor).

$$R_{355/940} = \frac{S(\mu_{HbO_2}^{355}) + (1-S)(\mu_{Hb_r}^{355}) + \mu_{amb}^{355}}{S(\mu_{HbO_2}^{940}) + (1-S)(\mu_{Hb_r}^{940}) + \mu_{amb}^{940}} \quad \text{Eq. 8-4}$$

$$R_{660/940} = \frac{S(\mu_{HbO_2}^{660}) + (1-S)(\mu_{Hb_r}^{660}) + \mu_{amb}^{660}}{S(\mu_{HbO_2}^{940}) + (1-S)(\mu_{Hb_r}^{940}) + \mu_{amb}^{940}} \quad \text{Eq. 8-5}$$

Simultaneous solving of these two equations yields estimates of both μ_{amb}^{355} and S , where S is the oxygen saturation. Five second averages of the AC and DC magnitudes at each wavelength are computed and used to solve the system of equations to determine μ_{amb}^{355} and S .

8.2.3 Animal Experiments

All animals were handled and cared for in accordance with the Louisiana Tech Institutional Animal Care and Use Committee (IACUC). Three female research albino mice (24-27g), of undetermined genetic characteristics was used in this study. The mouse was placed under anesthesia using isoflurane vaporized at 3% concentration as set by the vaporizer (LEI Medical, Model M 3000) with 95% oxygen (Invacare 5) delivered at a flow rate of 1.5 L/min to a small plastic enclosure.

Once immobilization was achieved, the mouse was moved to a temperature controlled heating pad (Physitemp TCAT-2LV, controller) set to 38° C and the feedback-thermometer was placed under the abdomen.

Anesthesia was maintained by delivering isoflurane at a concentration of 20% of that used to induce immobilization via a snout cone. The tail vein was then catheterized in order to deliver the injection.

Once the thermometer measured a temperature of $\geq 39^{\circ}\text{C}$, the probe was placed on the mouse's tail and allowed to collect the PPGs. Once signals at each wavelength met typically used metrics of signal quality (AC amplitudes of 5 mVp-p with standard deviations of less than 0.08 over the five second average), an injection of 25 μL Abelcet® solution was given at the concentration of 5 mg/mL in 5% dextrose solution. 125 μg of Abelcet® was delivered intravenously, corresponding to $\approx 5.2 \mu\text{g}/\text{gm}$.

The pulse photometer was allowed to collect estimates of μ_{amb} and S for different time points after the injection phase, was then removed briefly, and a final set of data meeting the previously described signal criteria was collected.

8.2.4 Blood Analysis

After each PPG reading, a blood sample was collected from the animals to compare the PPG readings with the analysis of the blood sample using blood spectrometry. This simple UV-VIS assay was conducted by diluting 5 μL of blood extracted from the tail vein into 995 μL of a 10% Triton-X solution to lyse scattering confounders such as red blood cells.

The extinction of the amphotericin b at 355 nm, after subtraction of the hemoglobin baseline, was quantified. The subtraction of the hemoglobin baseline was done by using the value of the peak at 560 nm (between the hemoglobin bands).

The blood samples were processed in UV-transparent micro- cuvettes [Brandtech (Essex, Connecticut) Ultra-Micro] in a low-volume spectrophotometer [DU 800, Beckman Coulter]. The corresponding values obtained from the UV/Vis analysis were plotted against the PPG values to generate a calibration curve.

8.3 Results

The PPG device was used to quantify the *in vivo* concentration of Abelcet® in near-real time. Blood draws corresponding to the PPG readings were also taken and analyzed using a UV/Vis spectrometer. The data points were taken at fixed time intervals after the injection to produce a bio-availability curve fitted with a single decay exponential model, as shown in Figure 8-1.

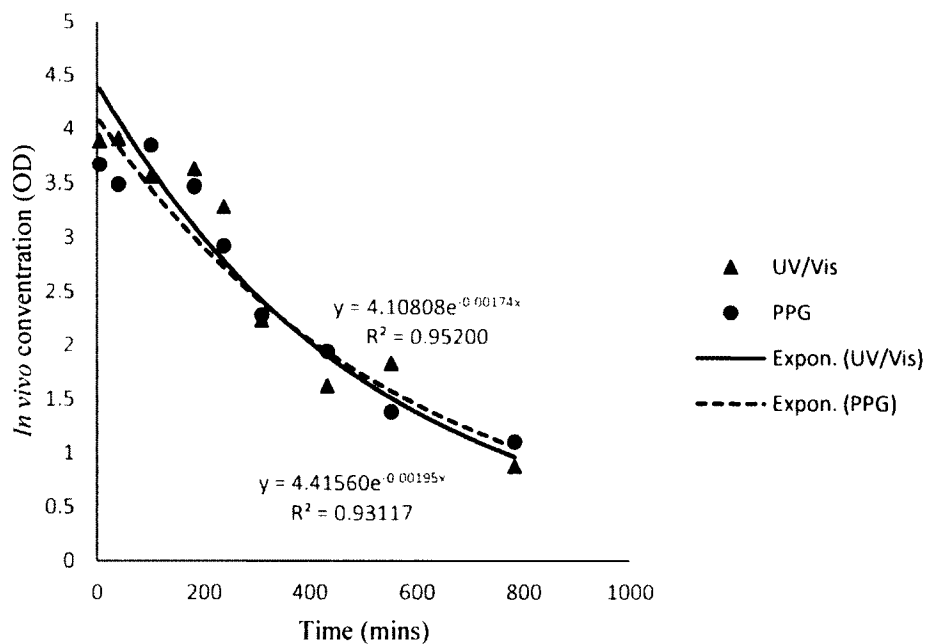


Figure 8-1: Bioavailability curve of Abelcet® *in vivo* as measured by the PPG ($R^2 = 0.95$) and the blood draws by UV/Vis analysis ($R^2 = 0.93$). The values were then fitted to a single decay exponential model to obtain half-lives. (UV/Vis = 355 min, PPG = 398 min.)

A single exponential decay model was used to describe the clearance of the drug from the blood, which produced a circulation half-life for Abelcet® in the blood. The average circulation half-life as measured by the PPG and blood draws were measured to be 483 min and 377 min respectively.

The calibration curve generated by using the data against UV/Vis spectrometry is shown in Figure 8-2.

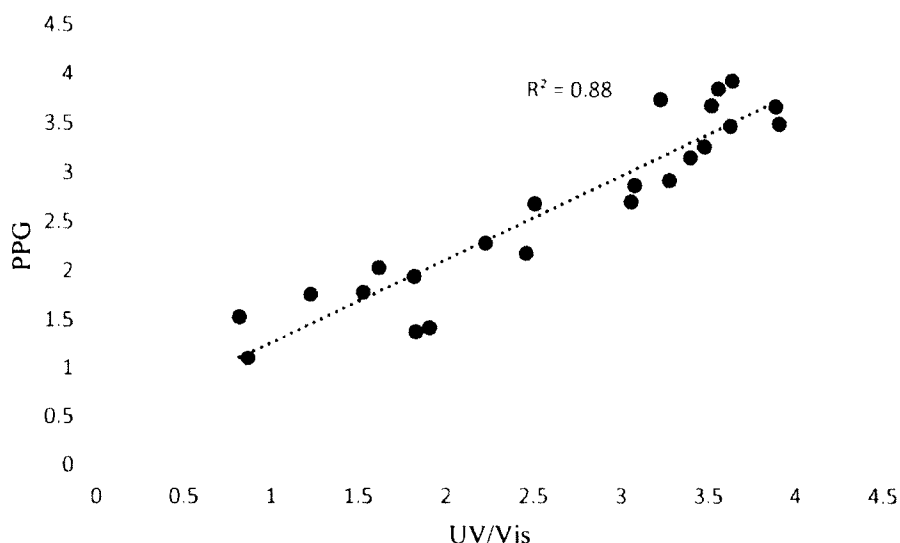


Figure 8-2: The comparison between the results of blood analysis (UV/Vis) and the PPG readings for intravenously injected Abelcet®. The graph represent the PPG readings that were taken at different time points after the injection, plotted against the UV/Vis analysis of the blood draws at the same time points (n = 3 mice, 7-8 points from each mouse). Linear fit resulted in a straight line with the equation: $y = 0.85x + 0.41$.

8.4 Discussion

The calibration curve demonstrates an underestimation of higher concentrations and overestimation at lower concentrations of circulating Abelcet®, which is similar to the work previously reported. This experimental bias in the instrument can explain the variation of the PPG half-life from the UV/Vis half-life. The range of concentrations that was detected by the PPG was experimentally determined to be 0.0987 mg/mL in the blood (≈ 4 OD) to 0.025 mg/ml in the blood. This range of values demonstrates that the device is feasible for *in vivo* detection of a clinical amphotericin dose.

8.5 Conclusion

Given the challenges in identifying the therapeutic levels required to achieve the effectiveness in various conditions that necessitates ampB, the known adverse effects associated with it, and continued investigations for ampB use in complex patients, the ability to sense the real time *in vivo* concentration of Abelcet® could have significant clinical implications. In addition, the theory of pulse dye densitometry and pulse plethysmography can be applied towards non-invasive detection and pharmacokinetics of other molecular drugs with similar spectral properties.

CHAPTER 9

CONCLUSIONS AND FUTURE WORK

This body of work demonstrates the development of various instrumentation and protocol improvements to pre-clinical and clinical outcomes. Closing the gap between the developed pre-clinical practices (in an academic setting) and pre-clinical and clinical setting (in industry) is part of future work that is necessary for a set of best practices to fully develop. The primary goal of these recommendations is improved clinical outcomes. The primary work toward improved clinical outcomes is developed through:

- Development of instrumentation for proper dose verification during the treatment, and continued observation throughout the clearance to minimize the chances of untoward reactions.
- Protocols for treatment decisions through observation of clinical signs (real-time blood plasma concentration and rapid elemental analysis of biopsied tissue
- Quantifying influential factors that affect final outcome (i.e. accumulation in the tumor) through use of data driven models, and continuing to search for new factors

The development and the use of the pulse photometer have been evaluated, and modified as needed for use with PEGylated gold nanoshells and nanorods. The instrumentation and data analysis protocols discussed in this work emphasize the ability to process data in near real time. The importance of standardized data analysis and monitoring is found primarily when future protocols use these devices to inform clinical decisions in real time. Early academic or pre-clinical studies have the luxury of time for making decisions, but clinical decisions will be made using this information in an urgent and life threatening climate. The climate these decisions will be made in highlights the need for standardized and easily interpreted results. The path toward data driven medicine will involve the personalized one compartment modeling from real-time blood plasma monitoring, and the ability to observe tumor uptake metrics. The ability to collect tumor uptake data is available through rapid elemental analysis.

The proposed rapid elemental analysis technique (EDXRF used in this work) allows for the quantitative analysis of gold in animal tissues. With a focus on future clinical implementation, elemental analysis will be required to be completed in under 12 hours. The current 12-hour window is based on timing of currently implemented clinical treatment protocols. This elemental analysis technique meets these requirements, and continues to be used in our animal research due to its ease of use and short turnaround time. Additional quantitative studies would be required to fully validate the technique and characterize the sources of errors in the protocol prior to human clinical use.

In advance of the implementation of industry standard population pharmacokinetic modeling techniques, the pulse photometer and current MATLAB coding were able to create individualized pharmacokinetic models. These individual one-

compartment pharmacokinetic models are designed for near-real-time clinical implementation. The personalized one-compartment models provide the ability for comparison of physiological responses to the treatment and allow us to head toward personalized cancer treatments. The population pharmacokinetic models can assist any clinical treatment with ongoing pre-clinical and clinical trials, and provide useful starting point information tailored to the patient (provided from the population pharmacokinetic models).

Future work should build on the set of one-compartment models to create a desired blood plasma concentration curve. From the desired curve there is potential for the implementation of traditional electrical engineering controls methods [79] to attempt to ensure a uniform blood plasma concentration curve. In future clinical settings, it will be possible for the delivery of nanoparticles to be different and contain new dosing strategies to ensure optimization of tumor uptake. Similar instrumentation can be used for dose verification and *in vivo* monitoring of other clinically relevant drugs. In addition to the ability to create a more uniform blood plasma concentration curve from patient to patient, the one-compartment models will be able to assist with the detection of undesired reactions (e.g. anaphylaxis) for different clinically relevant drugs, including the nanoparticles. As future studies search for improving clinical outcomes, the instrumentation, analysis protocols, and specifications discussed here can be useful as a starting point.

APPENDIX A

MOUSE BLOOD DRAW PROTOCOL

A.1 Theory

Blood draws taken from a mouse post injection of nanoshells can be used to measure the concentration of circulating nanoshells. UV-Vis spectra of the diluted blood draws can be analyzed using Beer's Law to separate extinction caused by the oxyhemoglobin and nanoshells in the sample. This is done by observing the value at the peak extinction wavelength for nanoshells and by using Eq. A-1:

$$A_{\text{peak}} = (\epsilon_{\text{NS}} C_{\text{NS}} + \epsilon_{\text{HbO}_2} C_{\text{HbO}_2}) D. \quad \text{Eq. A-1}$$

Where A is the extinction at the peak wavelength, the ϵ 's are the extinction coefficients for the two compounds of interest (oxyhemoglobin (compound b) and nanoshells (compound (a) in this case) at the peak wavelength, and C_{NS} and C_{HbO_2} are the concentrations nanoshells and HbO₂. Note that we are using the extinction coefficient for oxyhemoglobin because the blood samples have been exposed to air in the sampling process. Therefore, we assume that the hemoglobin is fully oxygenated. Also, note that the extinction is pathlength dependent, but we assume that D is one centimeter.

The concentration of nanoshells in the sample can be expressed using Eq. A-2:

$$C_{\text{NS}} = \frac{A_{\text{peak}} - \epsilon_{\text{HbO}_2} C_{\text{HbO}_2}}{\epsilon_{\text{NS}}}. \quad \text{Eq. A-2}$$

A.1.1 Finding the Extinction Coefficients for Nanorods

Since Beer's Law expresses concentrations as moles/liter, we will examine the nanorods as if each one was one atom. Therefore, you will notice that the molarities of nanorods that are found in each sample are extremely low, but since they are such good extinguishers of light, their molar extinction coefficients will be extremely high. As reported, batches of nanorods are manufactured to have a peak optical density of 100 at a

wavelength between 760 and 820 nm. The molar extinction coefficient is found using

Eq. A-3:

$$\epsilon_{NS} = \frac{A_{NS}}{c_{NS}} \quad \text{Eq. A-3}$$

The concentration of the nanoshells is reported as a number of particles/ml. We can find a molarity from Eq. A-4:

$$\frac{\text{NP's}}{\text{ml}} * \frac{1000\text{ml}}{1\text{L}} * \frac{\text{mol}}{6.02 * 10^{23} \text{ NP's}} = \frac{\text{moles NP's}}{\text{L}} \quad \text{Eq. A-4}$$

A.1.2 Blood Draws and Measurements

Once the extinction coefficient used in Eq. A-1 and Eq. A-2 is found, we can inject nanoparticles into a mouse, take blood samples, and examine them. The procedure for taking a blood sample and analyzing it is as follows:

1. Fill a micro-cuvette with 95 μl of 10% Triton-X 100. Blank the spectrometer using that micro-cuvette.
2. Heparinize a ten microliter pipette tip by sucking in five microliter of heparin and then releasing it leaving a layer of heparin inside the tip.
3. Obtain a five microliter blood sample using the heparinized tip and mix this with the Triton-X in the cuvette.
4. Scan this cuvette using the previously specified wavelengths (500-1100nm) and record the extinction at 805 nm (Let's say that is μ_{805}).
5. Dilute the sample using 100 μl Triton-X and scan again and record the extinction at 560 nm (μ_{560}).
6. Note that the hemoglobin "crest" is visible at around 560 nm.

7. The formula for optical density is as follows, in Eq. A-5:

$$\left(\mu_{805} - \left(\frac{\mu_{560}}{32613} \right) * 2 * 840 \right) * 20 = OD. \quad \text{Eq. A-5}$$

A.2 Adjustments

There will be an error in volume. To adjust for that, multiply the final OD value by $\frac{1.95}{\mu_{560}}$.

A.3 Calibration Curve/Typical Results

The spectra from blood draws taken from a mouse injected with nanoparticles can be seen in Figure A-1, and the calibration curve is shown in Figure A-2.

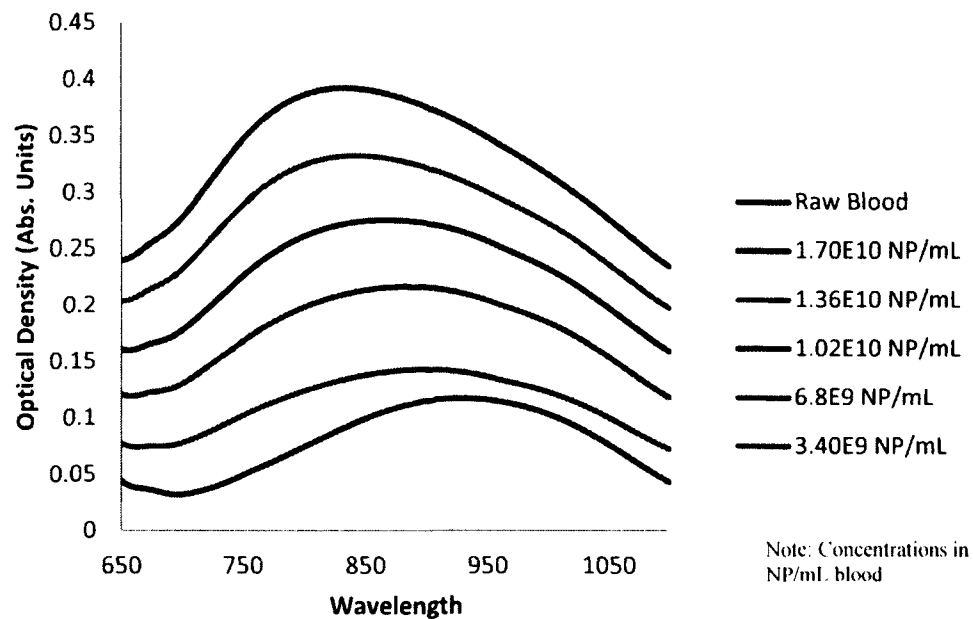


Figure A-1: Extinction spectra of blood prior to (raw blood) and post (all other spectra) injection. Note how the extinction at 760 nm increases greatly in comparison to 940 nm and then begins to return to a spectrum more like that for raw blood.

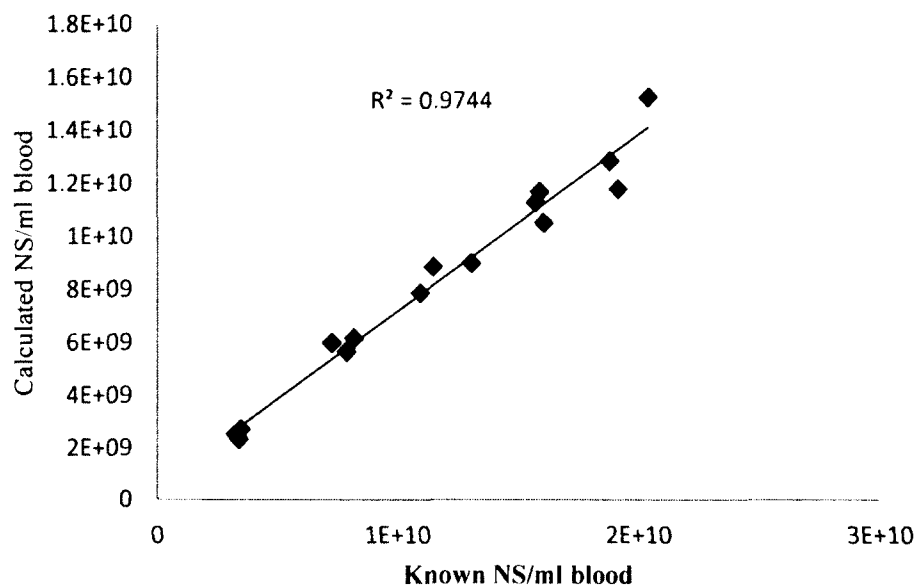


Figure A-2: Calibration curve comparing the calculated nanoshell concentration in samples containing blood and nanoshells to samples containing only known concentrations of nanoshells. The equation of the linear fit is $y = 0.6671x + 5E+08$

APPENDIX B

ESTIMATION OF THE LIMITS OF DETECTION OF AN LED DETECTOR COMBINATION

This addendum describes the process of roughly estimating the upper limit of detection for a known set of LED and detectors. In this example, the theoretical upper limit of detection for the 805 nm led of the four wavelength package L660/735/805/940-40B42-C-I, and S1227-33BR. The output power of the LED at 805 nm is rated at 3.5 mW. The datasheet can be obtained from the link that follows:

[<http://www.tech-led.com/data/L660.735.805.940-40B42-C-I.pdf>].

The spectral response chart shows that and the noise equivalent power (NEP) is of the photodiode is $2.1 \times 10^{-15} \text{ W/Hz}^{1/2}$, and the peak spectral response 0.43 A/W and spectral response at 805 nm is 0.4 A/W.

We know, the minimum detectable power:

$$P_{\min} = \frac{\text{NEP} * R_{\max} * \sqrt{B}}{R(\lambda)} \quad \text{Eq. B-1}$$

where, P_{\min} is the minimum detectable power with the photodiode with a SNR of 1

NEP is the noise equivalent power

R_{\max} is the maximum responsivity of the detector

$R(\lambda)$ is the responsivity of the photodiode at the LED wavelength

B is the measurement bandwidth

Using 12 kHz as the bandwidth (approximate value for the pulse photometer), we get the minimum detectable power to be 2.47×10^{-13} W. Now, let's suppose the incident power from LED at optimum conditions is 3.5mW. Therefore under the best conditions, the maximum theoretical limit of detection for this set is:

$$A = \log_{10} \frac{P_{\text{incident}}}{P_{\text{detected}}} = 11.14 \text{ OD} \quad \text{Eq. B-2}$$

APPENDIX C

AVERTIN ANESTHESIA (2,2,2-TRIBROMOETHANOL)

Avertin is useful for use in procedures where immobilization is less than 20 minutes and with no significant pain or distress. Avertin should provide good skeletal muscle relaxation and a moderate degree of respiratory depression.

C.1 Contraindication

Repeated administrations of avertin are contraindicated.

Do **NOT** inject intravenous, animal death would be expected within minutes.

C.2 Materials

2,2,2-tribromoethanol (Sigma-Aldrich T48402)

2-Methyl-2-Butanol (Alfa Aesar A18304)

C.3 Avertin Stock Solution

Mix:

1. 15 g 2,2,2-tribromoethanol
2. 15.5 mL 2-Methyl-2-Butanol
3. Mix overnight in a dark (amber) bottle at room temperature. (be sure to use clean stir bar)

The stock solution has a shelf life of six months when stored and wrapped in foil in a dark cabinet at room temperature. The following information **MUST** be on the outside of the bottle and the box the bottle is stored in: Solution, Expiration date, grams of 2,2,2-tribromoethanol and lot number, mL 2-Methyl-2-Butanol and lot number.

C.4 Avertin Working Solution

Mix:

1. 0.1 mL Avertin Stock Solution
2. 7.9 mL 0.9% Sterile Saline
3. Mix in a dark bottle and store overnight
4. Filter sterilize with 0.22 μm filter, label and store at four to six degrees Celsius.

Working solution has a shelf life of six months if unopened. Once the working solution has been opened, it has a shelf life of **one week**.

All containers of working solution must be labeled with the following information: Solution, Expiration date (once opened), Date of sterilization, Your Initials, mL Avertin stock solution, mL saline.

C.5 Animal Injection

Intraperitoneal (IP) injection of Avertin solution is given at the following dose:

Normal injection for slow particle infusion: 25 $\mu\text{L/g}$ body weight.

APPENDIX D

**INSTITUTIONAL ANIMAL CARE
AND USE COMMITTEE
APPROVAL LETTERS**

INSTITUTIONAL ANIMAL CARE AND USE COMMITTEE
Louisiana Tech University

25 October 2011
Dr. Patrick O'Neal, Ph.D.
Biomedical Engineering
Louisiana Tech University
Campus Box # 58

Dear Dr. O'Neal:

The Louisiana Tech University's Institutional Animal Care and Use Committee (IACUC) met on 17 October and approved your amended protocol entitled:

Nanoparticle Tracking For Cancer Therapy

The committee members feel that the transport of mice from Houston that have been inoculated with cancer cells is appropriate, and in keeping with your previous protocols. Please make sure that the animals are in a transport box with adequate water and that the vehicle be air-conditioned at all times so that the animals will not become dehydrated or overheated.

You and the students have been approved for a limit of 50 animals in this initial study beginning 1 November 2011. Please remember that you are required to keep adequate and accurate records of all procedures, results, and the number of animals used in this protocol. You are required to provide a progress report each year by 1 October. If the project should need to be extended beyond 31 October 2014, the third year, you will be required to submit a new protocol. Any changes you need to make in the protocol before the termination date must be submitted to the IACUC on the amendment form for approval before implementation.

Keep for your research records and results for three years after termination of the project. These records must be available for review by the IACUC or state and federal animal use agencies. Each year by 31 October you will be required to complete a summary of number of animals used in this protocol used for the United States Agricultural Agency (USDA). Note that failure to follow this protocol as approved may result in the termination of research. If you have any questions please call me at 318-243-0796 or via e-mail at jgspauld@latech.edu.

Sincerely,



James G. Spaulding, Chair
Louisiana Tech University IACUC

INSTITUTIONAL ANIMAL CARE AND USE COMMITTEE
Louisiana Tech University

9 September 2013

Patrick O'Neal, Ph.D.
Biomedical Engineering
Louisiana Tech University
Campus Box # 58

Dear Dr. O'Neal:

The members of the Institutional Animal Care and Use Committee (IACUC) have all read your protocol (Number2013-9) entitled: *Nanoparticle Tracking Instrumentation Test*. They have appointed me as the Designated Reviewer. I have read and approved your protocol.

Your protocol consists of two parts: (1) the use of animals from the Tech Farm that may require anesthesia. For this I recommend use of Ketamine or Xylazine either IV or IM to keep the animals sedated during the non-invasive testing.

(2) The testing at the instrumentation on dogs and cats at the Eastern Animal Clinic will be under the supervision of Dr. Sexton DVM and any anesthesia used will be provided by Dr. Sexton to assist in his procedures. One important procedure that will be required is the "Informed consent form" signed by the owners of the animals. The Eastern Animal Clinic should take care not to use any particular animal for too long a time or too many times on the animal or interrupt the business of the facility.

You have three years in which to complete the work. Your final report must be received by the IACUC by 1 October 2016. Yearly progress reports will be due 1 October of 2014 and 2015. Please remember that you are required to keep accurate records of all procedures, results, and the number of animals used in this project for each year after termination of the project. These records must be available for review by the IACUC or state and federal animal use agencies. Each year in October you will be required to complete a summary of animals used for the United States Department of Agriculture. Please that failure to follow this protocol as approved may result in the suspension of your protocol. If you have any questions please call me at 318-243-0796 or via email.

Sincerely,


James G. Spaulding, Chair
Louisiana Tech University

APPENDIX E

**INDIVIDUAL BIOAVAILABILITY
CURVES OF MICE USED
IN CHAPTER 7**

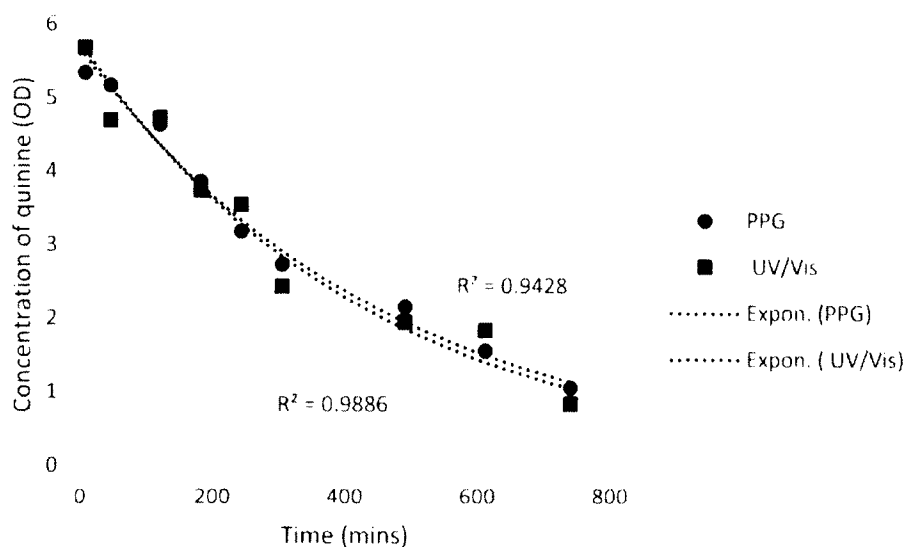


Figure E-1: Bioavailability curve of quinine *in vivo* as measured by the PPG ($R^2 = 0.989$) and the blood draws by UV/Vis analysis ($R^2 = 0.943$). The values were then fitted to a single decay exponential model to obtain half-lives in Mouse 1.

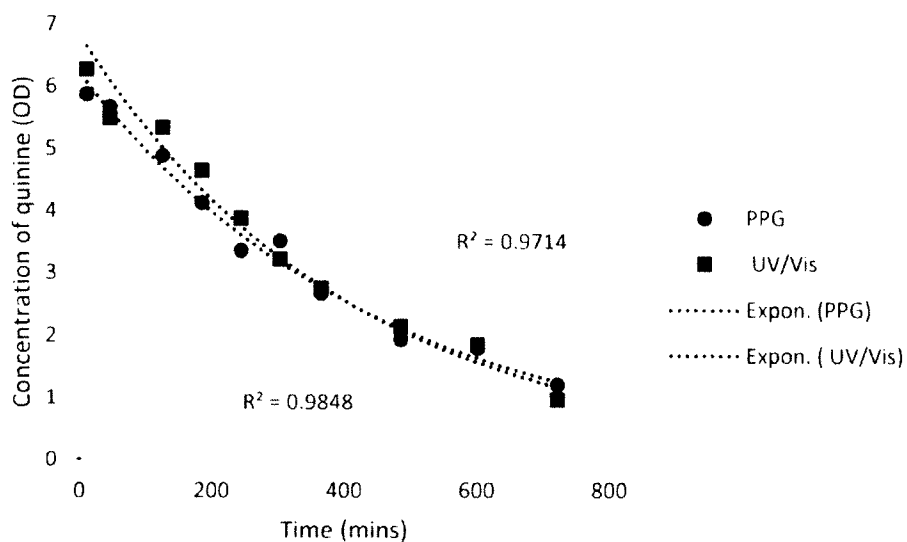


Figure E-2: Bioavailability curve of quinine *in vivo* as measured by the PPG ($R^2 = 0.985$) and the blood draws by UV/Vis analysis ($R^2 = 0.971$). The values were then fitted to a single decay exponential model to obtain half-lives in Mouse 2.

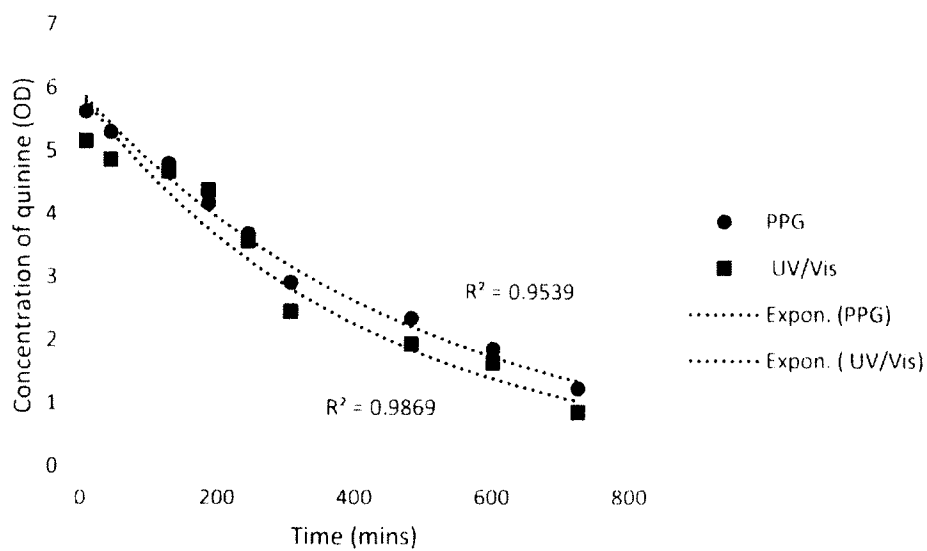


Figure E-3: Bioavailability curve of quinine *in vivo* as measured by the PPG ($R^2 = 0.987$) and the blood draws by UV/Vis analysis ($R^2 = 0.954$). The values were then fitted to a single decay exponential model to obtain half-lives in Mouse 3.

APPENDIX F

SAMPLE BIOAVAILABILITY CURVE OF MOUSE USED IN CHAPTER 8

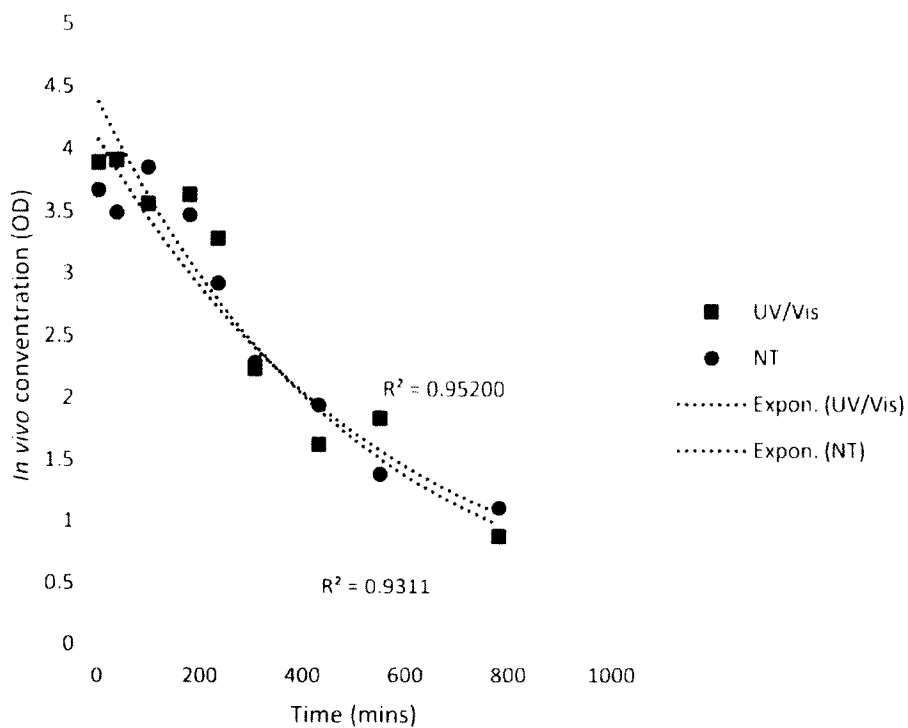


Figure F-1: Bioavailability curve of quinine *in vivo* as measured by the PPG ($R^2 = 0.952$) and the blood draws by UV/Vis analysis ($R^2 = 0.931$). The values were then fitted to a single decay exponential model to obtain half-lives in Mouse 1.

APPENDIX G

DESCRIPTION OF LOESS SMOOTHING FUNCTION

LOESS, originally proposed by Cleveland (1979) and further developed by Cleveland and Devlin (1988), specifically denotes a method that is more descriptively known as locally weighted polynomial regression. At each point in the data set, a low-degree polynomial is fit to a subset of the data with explanatory variable values near the point whose response is being estimated. The polynomial is fit using weighted least squares, giving more weight to points near the point whose response is being estimated and less weight to points further away. The value of the regression function for the point is then obtained by evaluating the local polynomial using the explanatory variable values for that data point. The LOESS fit is complete after regression function values have been computed for each of the n data points. Many of the details of this method, such as the degree of the polynomial model and the weights, are flexible. The range of choices for each part of the method and typical defaults are briefly discussed next.

LOESS combines much of the simplicity of linear least squares regression with the flexibility of nonlinear regression. It does this by fitting simple models to localized subsets of the data to build up a function that describes the deterministic part of the variation in the data, point by point. In fact, one of the chief attractions of this method is that the data analyst is not required to specify a global function of any form to fit a model to the data, only to fit segments of the data [10].

The local polynomials fit to each subset of the data are almost always of first or second degree, that is, either locally linear (in the straight line sense) or locally quadratic. Using a zero degree polynomial turns LOESS into a weighted moving average. Such a simple local model might work well for some situations, but may not always approximate the underlying function well enough. Higher-degree polynomials would work in theory,

but yield models that are not really in the spirit of LOESS. LOESS is based on the ideas that any function can be well approximated in a small neighborhood by a low-order polynomial and that simple models can be fit to the data easily. High-degree polynomials would tend to over fit the data in each subset and are numerically unstable, making accurate computations difficult.

As mentioned above, the weight function gives the most weight to the data points nearest the point of estimation and the least weight to the data points that are furthest away. The use of the weights is based on the idea that points near each other in the explanatory variable space are more likely to be related to each other in a simple way than points that are further apart. Following this logic, points that are likely to follow the local model best influence the local model parameter estimates the most. Points that are less likely to actually conform to the local model have less influence on the local model parameter estimates. The traditional weight function used for LOESS is the tri-cube weight function:

$$w(x) = \begin{cases} (1 - |x|^3)^3 & \text{for } |x| < 1 \\ 0 & \text{for } |x| \geq 1 \end{cases} \quad \text{Eq. G-1}$$

BIBLIOGRAHPY

- [1] Issa, A. M. Personalized Medicine and the Practice of Medicine in the 21st Century. *McGill J of Med.* 10(1):53-57, 2007.
- [2] G. J. Michalak, G. P. Goodrich, J. A. Schwartz, W. D. James, and D. P. O’Neal, “Murine photoplethysmography for *in vivo* estimation of vascular gold nanoshell concentration,” *J. Biomed. Opt.*, vol. 15, no. 4, 2010.
- [3] G. J. Michalak, H. A. Anderson, and D. P. O’Neal, “Feasibility of using a two-wavelength photometer to estimate the concentration of circulating near-infrared extinguishing nanoparticles,” *J. Biomed. Nanotechnol.*, vol. 6, no. 1, pp. 73–81, 2010.
- [4] J. Webster, *Medical Instrumentation: Application and Design*, Hoboken, NJ, John Wiley & Sons, 1998.
- [5] *Guidelines for the treatment of malaria -- 2nd edition*. WHO Press, World Health Organization. 2010, ISBN 978 92 4 154792 5.
- [6] S. H. Jang, M. G. Wientjes, D. Lu, and J. L.-S. Au, “Drug delivery and transport to solid tumors,” *Pharm. Res.*, vol. 20, no. 9, pp. 1337–1350, 2003.
- [7] F. Bray, J.-S. Ren, E. Masuyer, and J. Ferlay, “Global estimates of cancer prevalence for 27 sites in the adult population in 2008,” *Int. J. Cancer*, vol. 132, no. 5, pp. 1133–1145, Mar. 2013.

- [8] J. Ferlay, I. Soerjomataram, M. Ervik, S. Eser, C. Mathers, M. Rebelo, D. Parkin, D. Forman, and F. Bray, "Cancer Incidence and Mortality Worldwide: IARC CancerBase No. 11," International Agency for Research on Cancer, Lyon, France.
- [9] American Cancer Society, "Cancer Facts and Figures 2013," American Cancer Society, Atlanta, GA, 2013.
- [10] American Cancer Society, "Cancer Treatment & Survivorship Facts & Figures," American Cancer Society, Atlanta, GA, 2012.
- [11] M. Horner, L. Ries, M. Krapcho, N. Neyman, R. Aminou, N. Howlander, S. Altekruse, E. Feuer, L. Huang, and A. Mariotto, "SEER Cancer Statistics Review, 1975-2006, National Cancer Institute. Bethesda, MD," 2009.
- [12] Y.-I. Chang, W.-Y. Cheng, and C.-Y. Gu, "Application of the network model for studying the delivery of colloidal drugs," *Colloid Polym. Sci.*, vol. 289, no. 13, pp. 1479–1492, 2011.
- [13] H. Xue, M. B. Sawyer, P. E. Wischmeyer, and V. E. Baracos, "Nutrition modulation of gastrointestinal toxicity related to cancer chemotherapy: From preclinical findings to clinical strategy," *J. Parenter. Enter. Nutr.*, vol. 35, no. 1, pp. 74–90, 2011.
- [14] R. B. Livingston and F. J. Esteva, "Chemotherapy and Herceptin for HER-2+ metastatic breast cancer: The best drug?," *Oncologist*, vol. 6, no. 4, pp. 315–316, 2001.
- [15] M. Soltani and P. Chen, "Numerical modeling of fluid flow in solid tumors," *PLoS ONE*, vol. 6, no. 6, 2011.

- [16] R. K. Jain, "Transport of molecules across tumor vasculature," *Cancer Metastasis Rev.*, vol. 6, no. 4, pp. 559–593, 1987.
- [17] R. K. Jain, "Transport of molecules in the tumor interstitium: A review," *Cancer Res.*, vol. 47, no. 12, pp. 3039–3051, 1987.
- [18] S. K. Hobbs, W. L. Monsky, F. Yuan, W. G. Roberts, L. Griffith, V. P. Torchilin, and R. K. Jain, "Regulation of transport pathways in tumor vessels: Role of tumor type and microenvironment," *Proc. Natl. Acad. Sci. U. S. A.*, vol. 95, no. 8, pp. 4607–4612, 1998.
- [19] R. B. Campbell, "Tumor physiology and delivery of nanopharmaceuticals," *Anticancer Agents Med. Chem.*, vol. 6, no. 6, pp. 503–512, 2006.
- [20] W. L. Monsky, D. Fukumura, T. Gohongi, M. Ancukiewicz, H. A. Weich, V. P. Torchilin, F. Yuan, and R. K. Jain, "Augmentation of transvascular transport of macromolecules and nanoparticles in tumors using vascular endothelial growth factor," *Cancer Res.*, vol. 59, no. 16, pp. 4129–4135, 1999.
- [21] O. Ishida, K. Maruyama, K. Sasaki, and M. Iwatsuru, "Size-dependent extravasation and interstitial localization of polyethyleneglycol liposomes in solid tumor-bearing mice," *Int. J. Pharm.*, vol. 190, no. 1, pp. 49–56, 1999.
- [22] C. Loo, A. Lowery, N. Halas, J. West, R. Drezek, "Immunotargeted nanoshells for integrated cancer imaging and therapy," *Nano Letters*, vol. 5, pp. 709–711, 2005.
- [23] Hadas Skaat, Shlomo Margel, "Synthesis of fluorescent-maghemite nanoparticles as multimodal imaging agents for amyloid-[beta] fibrils detection and removal by a magnetic field," *Biochemical and Biophysical Research Communications*, vol. 386, pp. 645–649, 2009.

- [24] H. Liu, D. Chen, F. Tang, G. Du, L. Li, X. Meng, W. Liang, Y. Zhang, X. Teng, and Y. Li, "Photo thermal therapy of Lewis lung carcinoma in mice using gold nanoshells on carboxylated polystyrene spheres," *Nanotechnology*, vol. 19, pp. 17, 2008.
- [25] J. R. Tauro and R. A. Gemeinhart, "Matrix metalloprotease triggered delivery of cancer chemotherapeutics from hydrogel matrixes," *Bioconjug. Chem.*, vol. 16, no. 5, pp. 1133–1139, 2005.
- [26] E. Brewer, J. Coleman, and A. Lowman, "Emerging technologies of polymeric nanoparticles in cancer drug delivery," *J. Nanomater.*, vol. 2011, 2011.
- [27] T. M. Allen, W. W. K. Cheng, J. I. Hare, and K. M. Laginha, "Pharmacokinetics and pharmacodynamics of lipidic nano-particles in cancer," *Anticancer Agents Med. Chem.*, vol. 6, no. 6, pp. 513–523, 2006.
- [28] D. Peer, J. M. Karp, S. Hong, O. C. Farokhzad, R. Margalit, and R. Langer, "Nanocarriers as an emerging platform for cancer therapy," *Nat. Nanotechnol.*, vol. 2, no. 12, pp. 751–760, 2007.
- [29] B. Y. S. Kim, J. T. Rutka, and W. C. W. Chan, "Current concepts: Nanomedicine," *N. Engl. J. Med.*, vol. 363, no. 25, pp. 2434–2443, 2010.
- [30] J.-L. Li and M. Gu, "Gold-nanoparticle-enhanced cancer photothermal therapy," *IEEE J. Sel. Top. Quantum Electron.*, vol. 16, no. 4, pp. 989–996, 2010.
- [31] Z. Amoozgar and Y. Yeo, "Recent advances in stealth coating of nanoparticle drug delivery systems," *Wiley Interdiscip. Rev. Nanomed. Nanobiotechnol.*, vol. 4, no. 2, pp. 219–233, 2012.

- [32] V. P. Podduturi, I. B. Magaña, D. P. O'Neal, and P. A. Derosa, "Simulation of transport and extravasation of nanoparticles in tumors which exhibit enhanced permeability and retention effect." *Comput. Methods Programs Biomed.*, vol. 112, no. 1, pp. 58–68, 2013.
- [33] G. Kong, R. D. Braun, and M. W. Dewhirst, "Characterization of the effect of hyperthermia on nanoparticle extravasation from tumor vasculature." *Cancer Res.*, vol. 61, no. 7, pp. 3027–3032, 2001.
- [34] E. S. Day, J. G. Morton, and J. L. West, "Nanoparticles for thermal cancer therapy." *J. Biomech. Eng.*, vol. 131, no. 7, 2009.
- [35] G. J. Michalak, J. A. Schwartz, G. P. Goodrich, and D. P. O'Neal, "Three-wavelength murine photoplethysmography for estimation of vascular gold nanorod concentration," *Opt. Express*, vol. 18, no. 25, pp. 26535–26549, 2010.
- [36] G. P. Goodrich, L. Bao, K. Gill-Sharp, K. L. Sang, J. Wang, and J. Donald Payne, "Photothermal therapy in a murine colon cancer model using near-infrared absorbing gold nanorods," *J. Biomed. Opt.*, vol. 15, no. 1, 2010.
- [37] Dickerson, E.B., Dreaden, E.C., Huang, X., El-Sayed, I.H., Chu, H., Pushpanketh, S., McDonald, J.F., El-Sayed, M.A. "Gold nanorod assisted near-infrared plasmonic photothermal therapy (PPTT) of squamous cell carcinoma in mice." *Cancer Letters*. Vol 269(1), pp. 57-66, 2008.
- [38] Fowler, E.F., Thomson, A.W. "Effect of carrageenan on activity of the mononuclear phagocytic system in the mouse." *British Journal of Experimental Pathology*. 59, pp. 213. 1977.

- [39] Li YP, Pei YY, Zhang XY, Gu ZH, Zhou ZH, Yuan WF, Zhou JJ, Zhu JH, Gao Xj. PEGylated PLGA nanoparticles as protein carriers: Synthesis, preparation and biodistribution in rats. *J Control Release*. vol. 71, pp. 203-211, 2001.
- [40] G. Prencipe, S. M. Tabakman, K. Welsher, Z. Liu, A. P. Goodwin, L. Zhang, J. Henry, and H. Dai, "PEG branched polymer for functionalization of nanomaterials with ultra long blood circulation." *Journal of the American Chemical Society*, vol. 131, pp. 4783-4787, 2009.
- [41] W. D. James, L. R. Hirsch, J. L. West, P. D. O'Neal, and J. D. Payne, "Application of INNA to the build-up and clearance of gold nanoshells in clinical studies in mice," *Journal of Radioanalytical and Nuclear Chemistry*, vol. 271, no. 2, pp. 455-459, 2007.
- [42] H. Xie, K. L. Gill-Sharp, and D. P. O'Neal, "Quantitative estimation of gold nanoshell concentrations in whole blood using dynamic light scattering," *Nanomedicine: Nanotechnology, Biology, and Medicine*, vol. 3, pp. 89-94, 2007.
- [43] G. J. Michalak, G. P. Goodrich, J. A. Schwartz, W. D. James, and D. P. O'Neal, "Murine Photoplethysmography for *in vivo* Estimation of Vascular Gold Nanoshell Concentration," *JBO Letters*. Vol 15, no. 4, 2010.
- [44] Michalak, G. In-vivo, non-invasive monitoring of optically resonant metal nanoparticles using multi-wavelength photoplethysmography. A Dissertation Presented in Partial Fulfillment of the Requirements for the Degree of Doctor of Philosophy at Louisiana Tech University, 2010.

- [45] L. Sun, R. M. Crooks. "Fabrication and Characterization of Single Pores for Modeling Mass Transport Across Porous Membranes," *Langmuir*. Vol 15, pp. 738-741, Jan 8, 1999.
- [46] S. Oldenburg, R. Averitt, S. Westcott, and N. Halas, "Nanoengineering of optical resonances," *Chem. Phys. Lett.*, vol. 288, no. 2, pp. 243–247, 1998.
- [47] W. D. James, L. R. Hirsch, J. L. West, P. D. O'Neal, and J. D. Payne, "Application of INAA to the build-up and clearance of gold nanoshells in clinical studies in mice," *J. Radioanal. Nucl. Chem.*, vol. 271, no. 2, pp. 455–459, 2007.
- [48] N. R. Jana, L. Gearheart, and C. J. Murphy, "Wet chemical synthesis of high aspect ratio cylindrical gold nanorods," *J. Phys. Chem. B*, vol. 105, no. 19, pp. 4065–4067, 2001.
- [49] J. M. Tucker-Schwartz, K. R. Beavers, W. W. Sit, A. T. Shah, C. L. Duvall, and M. C. Skala, "*In vivo* imaging of nanoparticle delivery and tumor microvasculature with multimodal optical coherence tomography," *Biomed. Opt. Express*, vol. 5, no. 6, pp. 1731–1743, 2014.
- [50] D. E. Owens III and N. A. Peppas, "Opsonization, biodistribution, and pharmacokinetics of polymeric nanoparticles," *Int. J. Pharm.*, vol. 307, no. 1, pp. 93–102, 2006.
- [51] X. Yan, G. L. Scherphof, and J. A. A. M. Kamps, "Liposome opsonization," *J. Liposome Res.*, vol. 15, no. 1–2, pp. 109–139, 2005.

- [52] R. T. Zaman, P. Diagaradjane, J. C. Wang, J. Schwartz, N. Rajaram, K. L. Gill-Sharp, S. H. Cho, H. G. Rylander, J. D. Payne, S. Krishnan, and J. W. Tunnell, “*In vivo* detection of gold nanoshells in tumors using diffuse optical spectroscopy,” *IEEE J. Sel. Top. Quant. Electron.* 13, pp. 1715–1720, 2007.
- [53] T. Niidome, Y. Akiyama, K. Shimoda, T. Kawano, T. Mori, Y. Katayama, and Y. Niidome, “*In vivo* monitoring of intravenously injected gold nanorods using near-infrared light,” *Small* 4(7), pp. 1001–1007, 2008.
- [54] G. J. Michalak, G. P. Goodrich, J. A. Schwartz, W. D. James, and D. P. O’Neal, “Murine photoplethysmography for *in vivo* estimation of vascular gold nanoshell concentration,” *J. Biomed. Opt.* 15(4), 2010.
- [55] Y. Wang, X. Xie, X. Wang, G. Ku, K. L. Gill, D. P. O’Neal, G. Stoica, and L. V. Wang, “Photoacoustic tomography of a nanoshell contrast agent in the *in vivo* rat brain,” *Nano Lett.* 4(9), pp. 1689–1692, 2004.
- [56] J. W. Severinghaus, and Y. Honda, “History of blood gas analysis. VII. Pulse oximetry,” *J. Clin. Monit.* 3(2), pp. 135–138, 1987.
- [57] K. Yamakoshi, and Y. Yamakoshi, “Pulse glucosimetry: a new approach for noninvasive blood glucose measurement using instantaneous differential near-infrared spectrophotometry,” *J. Biomed. Opt.* 11(5), pp. 1–9, 2006.
- [58] T. Iijima, T. Aoyagi, Y. Iwao, J. Masuda, M. Fuse, N. Kobayashi, and H. Sankawa, “Cardiac output and circulating blood volume analysis by pulse dye-densitometry,” *J. Clin. Monit.* 13(2), pp. 81–89, 1997.

- [59] T. Imai, C. Mitaka, T. Nosaka, A. Koike, S. Ohki, Y. Isa, and F. Kunimoto, "Accuracy and repeatability of blood volume measurement by pulse dye densitometry compared to the conventional method using ^{51}Cr -labeled red blood cells," *Intensive Care Med.* 26(9), pp. 1343–1349, 2000.
- [60] N. Taguchi, S. Nakagawa, K. Miyasaka, M. Fuse, and T. Aoyagi, "Cardiac output measurement by pulse dye densitometry using three wavelengths," *Pediatr. Crit. Care Med.* 5(4), pp. 343–350, 2004.
- [61] Y. Mendelson, R. M. Lewinsky, and Y. Wasserman, "Multi-wavelength reflectance pulse oximetry," *Anesth. Analg.* 94(1 Suppl), pp. S26–S30, 2002
- [62] J. G. Webster, *Design of Pulse Oximeters*, Chapter 4, pp. 40–55, New York, NY, Taylor and Francis Group, 1997.
- [63] T. Aoyagi, M. Fuse, N. Kobayashi, K. Machida, and K. Miyasaka, "Multiwavelength pulse oximetry: theory for the future," *Anesth. Analg.* 105(6 Suppl), pp. S53–S58, 2007.
- [64] J. Kraitl, H. Ewald, and H. Gehring, "An optical device to measure blood components by a photoplethysmographic method," *J. Opt. A, Pure Appl. Opt.* 7(6), pp. S318–S324, 2005.
- [65] S. J. Barker, J. Curry, D. Redford, and S. Morgan, "Measurement of carboxyhemoglobin and methemoglobin by pulse oximetry: a human volunteer study," *Anesthesiology* 105(5), pp. 892–897, 2006.

- [66] W. G. Zijlstra, A. Buursma, and W. P. Meeuwse-van der Roest, "Absorption spectra of human fetal and adult oxyhemoglobin, de-oxyhemoglobin, carboxyhemoglobin, and methemoglobin," *Clin. Chem.* 37(9), pp. 1633–1638, 1991.
- [67] R. Notari, *Biopharmaceutics and Pharmacokinetics: an Introduction*. New York, NY: Marcel Dekker Inc., 1971.
- [68] W. H. De Jong, W. I. Hagens, P. Krystek, M. C. Burger, A. J. A. M. Sips, and R. E. Geertsma, "Particle size-dependent organ distribution of gold nanoparticles after intravenous administration," *Biomaterials*, vol. 29, no. 12, pp. 1912–1919, 2008.
- [69] S. Sturtz, U. Ligges, and A. Gelman, "R2WinBUGS: A package for running WinBUGS from R," *J. Stat. Softw.*, vol. 12, pp. 1–16, 2005.
- [70] G. Hoffman, "Methods of Analysis by the U.S. Geological Survey National Water Quality Laboratory- Preparation Procedure for Aquatic Biological Material Determined for Trace Metals," U.S. Department of the Interior, Denver, CO, Open-File Report 96-362, 1996.
- [71] J. Anzelmo, A. Seyfarth, and L. Arias, "Approaching a Universal Sample Preparation Method for XRF Analysis of Powder Materials," *Diffr. Data*, vol. 44, pp. 368–373, 2001.
- [72] J. Börjesson and S. Mattsson, "Medical applications of X-ray fluorescence for trace element research," *Powder Diffr.*, vol. 22, no. 2, pp. 130–137, 2007.
- [73] J. Scott and S. Lillicrap, "¹³³Xe for the x-ray fluorescence assessment of gold *in vivo*," *Phys. Med. Biol.*, vol. 33, no. 7, pp. 859–864, 1988.

- [74] M. Szczerbowska-Boruchowska, "Sample thickness considerations for quantitative X-ray fluorescence analysis of the soft and skeletal tissues of the human body - theoretical evaluation and experimental validation." *X-Ray Spectrom.*, vol. 41, no. 5, pp. 328–337, 2012.
- [75] J. Bacso, I. Uzonyi, and B. Dezsó, "Determination of gold accumulation in human tissues caused by gold therapy using x-ray fluorescence analysis." *Appl. Radiat. Isot.*, vol. 39, no. 4, pp. 323–326, 1988.
- [76] Cope M and Delpy D T System for long term measurement of cerebral blood and tissue oxygenation on newborn infants by near infrared transillumination *Med. Biol. Eng. Comput.* 26(3) 289-94, 1988.
- [77] Cope M, Delpy D T, Reynolds E+ R, Wray S, Wyatt J S and van der Zee P Methods of quantitating cerebral near infrared spectroscopy data *Adv. Exp. Med. Biol.* 222 183-90, 1988.
- [78] X. Huang, X. Peng, Y. Wang, Y. Wang, D. M. Shin, M. A. El-Sayed, and S. Nie, "A reexamination of active and passive tumor targeting by using rod-shaped gold nanocrystals and covalently conjugated peptide ligands," *ACS Nano*, vol. 4, no. 10, pp. 5887–5896, 2010.
- [79] K. Ricketts, A. Castoldi, C. Guazzoni, C. Ozkan, C. Christodoulou, A. P. Gibson, and G. J. Royle, "A quantitative x-ray detection system for gold nanoparticle tumour biomarkers," *Phys. Med. Biol.*, vol. 57, no. 17, pp. 5443–5555, 2012.

- [80] I. B. Magaña, P. Adhikari, M. C. Smalley, S. E. Eklund, and D. P. O'Neal, "Feasibility of energy dispersive X-ray fluorescence determination of gold in soft tissue for clinical applications," *Anal. Methods*, vol. 5, no. 12, pp. 3148–3151, 2013.
- [81] Nie, S., Understanding and overcoming major barriers in cancer nanomedicine. *Nanomedicine (Lond)*, 5(4), pp. 523–528, 2010.
- [82] Frieboes H. B., Min Wu, John Lowengrub, Paolo Decuzzi, Vittorio Cristini, A computational model for predicting nanoparticle accumulation in tumor vasculature. *Plos One* 8(2) e56876, 2013.
- [83] Gutiérrez, L., Raquel Mejías , Francisco J. Lázaro , Carlos J. Serna , Domingo F. Barber, M. Puerto Morales. Effect of Anesthesia on Magnetic Nanoparticle Biodistribution After Intravenous Injection. *IEEE Trans. on Mag.* 49(1): 398-401, 2013.
- [84] Hashizume, H., P. Baluk, S. Morikawa, J. W. McLean, G. Thurston, S. Roberge, R. K. Jain, D. M. McDonald. Openings between Defective Endothelial Cells Explain Tumor Vessel Leakiness. *Am. J. of Path.*, 156(4): 1363-1380, 2000.
- [85] Puvanakrishnan, P., Park, J., Chatterjee, D., Krishnan, S., Tunnell, J.W. "In vivo tumor targeting of gold nanoparticles: effect of particle type and dosing strategy." *Int. J of Nanomed.*, 7. 1251-1258, 2012.
- [86] P. Adhikari, S. S. Bracey, K. A. Evans, I. B. Magana, and D. P. O'Neal, "LQR tracking of a delay differential equation model for the study of nanoparticle dosing strategies for cancer therapy." *Am. Con. Conf.* pp. 2068–2073, 2013.

- [87] Rumjanek VM, Watson SR, Sljivic VS. A re-evaluation of the role of macrophages in carrageenan induced immunosuppression. *Immunology*; 33 (3):423–32, 1977.
- [88] Bateman D.N., Blain P. G., Woodhouse K. W., Rawlins M. D., Dyson H., Heyworth R., Prescott L. F., Proudfoot A. T., “Pharmacokinetics and Clinical Toxicity of Quinine Overdosage: Lack of Efficacy of Techniques Intended to Enhance Elimination.” *QJM* , 54 (2) 125-131; Feb 1985.
- [89] Adhikari, P., Magana, I., O’Neal, D.P. “Multi-wavelength pulse plethysmography for real-time drug delivery monitoring.” *Proc. SPIE (BiOS) West*, 2014.
- [90] Invasive Candidiasis Statistics. 2013. (Accessed 01-252015, at <http://www.cdc.gov/fungal/diseases/candidiasis/invasive/statistics.html>.)
- [91] Steinbach, W.J., Roilides,E., Berman, D. “Results from a prospective, international epidemiologic study of invasive candidiasis in children and neonates.” *The Ped. Inf Dis. J* 31:1252-7, 2012.
- [92] Hundalani, .S, Pammi, M. “Invasive fungal infections in newborns and current management strategies.” *Exp. Rev. of Anti-Inf. Therap.* 11:709-21, 2013.
- [93] Luu Tran, H., Mahmoudjafari, Z., Rockey M. “Tolerability and outcome of once weekly liposomal amphotericin B for the prevention of invasive fungal infections in hematopoietic stem cell transplant patients with graft-versus-host disease.” *J. of Onc. Pharm. Prac.* 2014.